STRUCTURE AND ANISOTROPY OF THE UPPER MANTLE

by

JAMES B. GAHERTY

Sc.B., Brown University, 1986
M.S., University of Michigan, 1990

Submitted to the Department of
Earth, Atmospheric, and Planetary Sciences
in partial fulfillment of the requirements for the degree of

DOCTOR OF PHILOSOPHY

at the

MASSACHUSETTS INSTITUTE OF TECHNOLOGY

June, 1995

Signature of Author _____
Department of Earth, Atmospheric, and Planetary Sciences
May 1995

Certified by _____
Thomas H. Jordan
Thesis Supervisor

Accepted by _____
Thomas H. Jordan
Department Head

STRUCTURE AND ANISOTROPY OF THE UPPER MANTLE

by

JAMES B. GAHERTY

Submitted to the Department of Earth, Atmospheric, and Planetary Sciences in partial fulfillment of the requirements for the degree of Doctor of Philosophy

We investigate the nature of seismic anisotropy in the upper mantle by inverting two classes of data that provide increased vertical resolution of upper-mantle structure. Frequency-dependent travel-time residuals of three-component turning and surface waves such as *S*, *SS*, *SSS*, R_1, and G_1 are used to constrain the anisotropic velocity structure within a layered framework. Details on the layering (travel times to and impedance contrasts across all significant upper mantle and transition zone discontinuities) are provided by previous analyses of *ScS* reverberations. These data are jointly inverted using a Bayesian scheme that employs mineral physics, geological, and seismological data as prior information. A path average approximation is used to determine one-dimensional transversely isotropic structure within tectonically isolated corridors.

We analyze seismic data from 55 earthquakes that sample the old oceanic upper mantle between Tonga-Fiji and Hawaii, as well as data from 22 earthquakes that sample the upper mantle beneath cratonic western Australia. Our preferred model for the western Pacific is characterized by a high velocity, anisotropic seismic lithosphere, bounded at 68-km depth by a large (negative) Gutenburg discontinuity; a distinct anisotropic low velocity zone extending to 166-km depth; no significant Lehmann discontinuity; and an isotropic, steep-gradient region between 166 km and 415 km depth. The upper mantle beneath western Australia is characterized by a fast, thick, anisotropic layer bounded at 252-km depth by the Lehmann discontinuity, underlain by an isotropic high-velocity region extending to the 410-km discontinuity. These models support the proposal that the Lehmann discontinuity beneath stable continents represents a transition from an anisotropic lithosphere to a more isotropic material in the lower part of the continental tectosphere. Beneath the Pacific, anisotropy extends into the low-velocity zone, implying that it is both locked into the seismic lithosphere during plate formation, and is being maintained by current dynamic flow in the oceanic asthenosphere. Similarity of anisotropic signature between the Tonga-Hawaii path and alternative paths in the western Pacific indicates that any dynamic flow alignment does not coincide with current plate motion, but rather has smaller characteristic length scales.

Thesis Committee:

Dr. Thomas H. Jordan, Professor of Geophysics (Thesis Supervisor)
Dr. Timothy L. Grove, Professor of Geology
Dr. Bradford H. Hager, Professor of Geophysics
Dr. Chris J. Marone, Professor of Geophysics
Dr. Paul G. Silver, Carnegie Institute of Washington

TABLE OF CONTENTS

CHAPTER 1

Introduction

Over the last decade, remarkable advances have been made in mapping lateral variations in Earth's seismic velocity structure. Three-dimensional (3D) tomographic models provide maps of shear and compressional velocity variations in the crust, mantle, and core on global and regional scales, generating new insight into the structure, composition, and dynamics of the Earth's interior [*Dziewonski*, 1984; *Woodhouse and Dziewonski*, 1984; *Grand*, 1987, 1994; *Inoue et al.*, 1990; *Tanimoto*, 1990; *Montagner and Tanimoto*, 1991; *Pullium et al.*, 1993; *Zhang and Tanimoto*, 1993; *Su et al.*, 1994; *Zielhuis and Nolet*, 1994]. Such models do have short-comings, however, primarily due to the limited spatial extent and/or resolution of seismic data sets and constraints on the number of parameters that realistically can be included in such models. This lack of resolution is particularly acute in the upper mantle, where typical global 3D models display far less variability than that observed among regional one-dimensional models [*Nolet et al.*, 1994]. Much of the variability may come in parameters that are not incorporated in typical 3D models; rapid changes in radial gradients and discontinuities, for example, or differences in anisotropic structure. Such parameters are diagnostic of composition, phase, thermal, and mechanical structure in the upper mantle, and spherically-symmetric, one-dimensional (1D) anisotropic models remain an excellent mechanism for examining regional variation of such structure. In this thesis we have two major goals: 1) provide new, high-resolution regional upper mantle models that incorporate variable radial gradients, discontinuities, and anisotropy; and 2) increase the understanding of anisotropy, discontinuities, and the underlying thermal and mechanical structure of the upper mantle via generation and analysis of these models.

NEW REGIONAL MODELS

Toward the first goal, we present new regional seismic models of the upper mantle from two narrow, well-isolated corridors -- one traversing the western Pacific, one crossing western Australia -- using a one-dimensional, path-average, transversely isotropic (radially anisotropic) parameterization. Because we can accurately calculate three-component synthetic seismograms in the frequency band of 0-50 mHz (down to 20 s period) from such models, this methodology provides several benefits: 1) we can analyze seismograms more completely in both time (multiple phases -- *S, SS, SSS*, surface waves, all on three components) and frequency (travel time behavior across the 10-45 mHz band, much broader than most structural studies); 2) we can fully iterate our inversion process (i.e. completely reanalyze our data using an improved model), which is very important owing to the non-linearity inherent in the seismic problem; and 3) the parameterization allows us to focus on the variability of radial gradients, discontinuities, and anisotropy as a function of depth. The disadvantage of this approach is that it averages along-path heterogeneity and potential azimuthal anisotropy that is nominally resolved in alternative analyses. We have minimized the expense of the former by choosing short corridors that cross simple, tectonically stable regions of oceanic and continental upper mantle. The latter can be addressed by considering theoretical and laboratory constraints, as well as observations from different azimuths, in the interpretation of the resulting models. Our approach is ultimately validated by demonstrating our models' ability to fit observed seismograms: synthetics from 1D models that account for regional variations in discontinuities and anisotropy match the observed data better than synthetics from 3D models that ignore variability in these features.

Our models are constructed by applying two complementary seismic analysis techniques that provide increased vertical resolution of upper-mantle structure. We start with the results of *Revenaugh and Jordan* [1991a-c], who employ *ScS* reverberations to identify, locate and measure the impedance contrasts of upper-mantle discontinuities for

several corridors crossing a variety of tectonic environments in the southwest Pacific and Australasia. The resulting vertical travel times and impedance contrasts establish precise layered frameworks for corridor-specific upper-mantle velocity models. Velocities (and anisotropy) within these frameworks are constrained by frequency-dependent travel times of body (S, SS, sSS, SSS) and surface (R_1, G_1) seismic phases measured from three-component, long-period seismograms using the isolation filter techniques of *Gee and Jordan* [1992]. This combination of surface and body waves provides excellent sensitivity to velocity structure throughout the upper mantle and transition zone. These data are jointly inverted for layered, radially anisotropic models by solving the linearized inverse problem from first-order perturbation theory:

$$\mathbf{G}\delta\mathbf{m} = \delta\mathbf{d},$$

where $\delta\mathbf{d}$ is a vector containing ScS-reverberation and frequency-dependent travel time residuals, $\delta\mathbf{m}$ is the model perturbation, and $\mathbf{G}$ is a matrix of partial derivatives that describe the sensitivity of the data to changes in the model parameters. In our case, $\delta\mathbf{m}$ includes depths to discontinuities, velocities, and linear gradients in each layer, all of which are allowed to vary.

Despite the good sensitivity of our data set and a layered parameterization, we cannot uniquely determine all features of a radially anisotropic model. We therefore employ a Bayesian inference scheme [e.g. *Tarantola and Valette*, 1982] that allows us to directly incorporate additional information in the inversion process. This information comes in the form of prior knowledge of the model space, based on mineralogical data [e.g. *Montagner and Anderson*, 1989; *Ita and Stixrude*, 1993] and expectations on anisotropic structure inferred from other seismological [e.g. *Hess*, 1964; *Shearer and Orcutt*, 1986] and geological [e.g. *Nicolas and Christensen*, 1987] observations. These prior distributions also serve as a means to test hypotheses on the state of the upper mantle: for example, can data sampling the continental upper mantle be explained by a model with low velocities characteristic of oceanic upper mantle below 300 km depth? These

hypothesis tests hold a number of implications for anisotropy and structure of the upper mantle.

RADIAL GRADIENTS, DISCONTINUITIES, AND ANISOTROPY IN THE UPPER MANTLE

There is a long history of inference of upper mantle properties from spherically symmetric, layered velocity models, starting with the debates of Lehmann, Gutenburg, Jeffreys, and Bullen on the existence of a low-velocity zone and 410-km discontinuity [e.g. *Gutenburg*, 1959], and continuing with *Jordan's* [1975] and *Anderson's* [1979] debate on the thicknesses of the thermal boundary layer beneath continents and oceans. The first debate has been resolved via improved data and modeling, but many aspects of the latter debate remain unresolved, primarily because comparisons are often made using models that have been constructed using a variety of data types and modeling procedures. For example, Figure 1.1 displays four models, two oceanic and two continental. The continental models maintain higher velocities to the 410-km discontinuity, evidence of a thick, high-velocity thermal boundary layer beneath continents [*Jordan et al.*, 1989]. Details of this contrast remain hazy because the models represent not simply tectonic differences, but also different data types (i.e. *SH* vs. *PSV*, surface vs. body waves) used in the modeling. In addition, *Anderson* [1979] argued that these ocean-continent differences are due to the exclusion of anisotropy in the modeling process. By utilizing an analysis technique that handles three-component surface and body waves in a self-consistent fashion, and by directly including variable anisotropy, we show that the ocean-continent differences in Figure 1.1 are robust characteristics of the upper mantle. We also refine our understanding of these differences by considering the anisotropic structure in the context of mean oceanic and continental velocities.

Radial models also provide information via discontinuities. While the transition zone discontinuities are reasonably well understood in terms of phase-changes in an olivine-dominated upper mantle [*Ringwood*, 1975; *Bina*, 1991], interpretation of the

variety of observations of upper mantle discontinuities has remained elusive [e.g. *Adams*, 1968; *Whitcomb and Anderson*, 1969; *Jordan and Frazier, 1975*; *Bock*, 1988; *Vidale and Benz*, 1991; *Shearer*, 1993; *Zhang and Lay*, 1994]. A recent model proposed by *Revenaugh and Jordan* [1991a-c] incorporates upper-mantle and transition-zone discontinuities whose properties correlate with tectonic structure (Figure 1.2). Historically-defined boundaries of Gutenburg ("G"), Hales ("H"), and Lehmann ("L") were interpreted within this regional context, a new subduction-related discontinuity ("X") was proposed, and the thermal variability of the transition-zone discontinuities was demonstrated. This model implies distinct relationships between upper mantle discontinuities and the surrounding velocity structure: for example, G is related to the low-velocity zone beneath oceans, and L is related to an anisotropic boundary beneath continents. We test these hypotheses by establishing the velocities between discontinuities, and we place constraints on the mechanical structure of the upper mantle by considering the discontinuities jointly with anisotropy. Our models also improve the interpretation of the thermal variability of transition zone discontinuities by placing them into the context of their background velocity.

Theoretically, the composition and state of the upper mantle and transition zone can be inferred by comparing the gradients in radial seismic models with those calculated and/or measured from hypothesized mineralogical assemblages [e.g. *Ringwood*, 1975; *Bass and Anderson*, 1984; *Weidner*, 1985; *Duffy and Anderson*, 1989; *Rigden et al.*, 1991; *Ita and Stixrude*, 1993]. In practice such inference is difficult, primarily because of the two-step scheme typically used to test mineralogical models: 1) velocity models are constructed from seismological data sets more or less independently of other considerations, and (2) these models are then treated as a type of data in testing various mineralogical and compositional hypotheses. The first step is done by seismologists and the second by mineral physicists and geochemists, usually in disjunct groups. The result is highly dependent on the particular seismic model employed as data in step 2 (e.g. global vs. regional, *S* vs. *P*

velocities), and consideration of the non-uniqueness inherent in the seismic model is difficult. The methodology presented here allows the testing of mineralogical models by directly including mineralogical constraints in the inversion process. This procedure incorporates realistic error estimates of both seismological and mineralogical parameters, and consistency (or lack thereof) of the seismic data with the mineralogical hypothesis can be directly evaluated. In the current implementation, we utilize the seismic data to constrain shear velocities (which are poorly constrained by mineral physics observations), and we use the mineralogical data to constrain the density and bulk sound velocity (which are poorly constrained by our shear wave observations). The resulting model fits the seismic data, and could represent either pyrolite or high-aluminum piclogite compositions [*Ita and Stixrude*, 1993]. Future work will incorporate additional seismic data to allow for the testing of specific mineralogical hypotheses.

It is generally accepted that seismic anisotropy in the upper mantle arises via crystallographic alignment of olivine and (to a lesser extent) pyroxene in mantle rocks [e.g. *Nicolas and Christensen*, 1987]. While seismic velocities are a function of composition, phase, pressure, and temperature of mantle minerals, anisotropy is a function of these plus the integrated strain history of the material [*Ribe*, 1992], and thus provides a unique tool for studying the dynamics and mechanics of the upper mantle. Anisotropy illuminates the tectonic history of both oceanic [*Hess*, 1964; *Forsyth*, 1975a; *Regan and Anderson*, 1984; *Shearer and Orcutt,* 1986; *Nishimura and Forsyth*, 1989] and continental [*Gee and Jordan*, 1988; *Silver and Chan*, 1991] lithosphere, as well as the convective flow field related to active deformation in the sublithospheric upper mantle [*Montagner and Tanimoto*, 1991; *Vinnik et al.,* 1992; *Gao et al.*, 1994; *Russo and Silver*, 1994]. In detail, however, our knowledge of anisotropic structure is quite sketchy. Little is known regarding the length scales (both vertical and horizontal) of anisotropic structure, for example. *Montagner and Tanimoto* [1991] and *Vinnik et al.* [1992, 1995] argue that azimuthal anisotropy with a coherent horizontal fast axis can be observed over the scale length of the plates , i.e.

thousands of kilometers. Significant variations of shear wave splitting observed over short lateral distances [*Silver and Kaneshima,* 1993; *McNamara et al.*, 1994] imply just the opposite case -- azimuthal anisotropy with significant fast-axis variations over tens to a few hundred kilometers, even in oceanic regions [*Farra and Vinnik*, 1994]. These two scenarios imply very different modes of deformation in the mantle, and we need to delineate them and understand their tradeoffs. Our models allow us to establish rough upper limits on the length scales of anisotropic structure. In particular, we find little evidence of large-scale anisotropy oriented with global plate motion beneath the Pacific.

The regional variability of anisotropic structure is also not well established, other than the strong correlation of azimuthal anisotropy with fossil-spreading direction in oceanic plates [*Hess*, 1964; *Forsyth*, 1975a; *Nishimura and Forsyth*, 1989; *Montagner and Tanimoto*, 1991], and an apparent correlation between fast vertical shear-wave polarization and the trend of tectonic cordillera [*Silver and Chan*, 1991; *Vinnik et al.*, 1992; *Russo and Silver*, 1994; *Yang et al.*, 1995]. In the only global 3D models that incorporate anisotropy, *Nataf et al.* [1986] find a general correlation of the magnitude of polarization anisotropy with tectonic province, *Montagner and Tanimoto* [1991] extend this analysis to include azimuthal anisotropy. The resolution of these analyses is severely limited by the reliance on long-period surface waves and tradeoffs with three-dimensional isotropic heterogeneity, however, and thus even ocean-continent differences are not clearly established. Using single corridor analyses such as those presented here, *Cara and Leveque* [1988] find that anisotropy extends deeper beneath North America than the Pacific, and *Gee and Jordan* [1988] infer that radial anisotropy beneath tectonically-active southwest Eurasia is smaller than that beneath the stable shields and platforms of Siberia and northern Eurasia. Both observations imply intriguing regional variability that needs to be confirmed and interpreted using a more complete analysis. A critical element lacking from most analyses of anisotropy is an explicit demonstration of the depth extent of the anisotropy. The depth distribution of anisotropic structure is inferred from the correlation of a fast direction with

expected lithospheric (tectonic) or sublithospheric (convective) patterns [*Silver and Chan*, 1991; *Vinnik et al.*, 1992, 1995; *Su and Park*, 1994], it is assumed a priori [*Regan and Anderson*, 1984], or it is simply allowed to extend throughout the depth range sampled by the data [*Nataf et al.*, 1986; *Cara and Leveque*, 1988; *Nishimura and Forsyth*, 1989; *Montagner and Tanimoto*, 1991].

Testing hypothesized prior distributions on the model space allows us to evaluate the depth extent of anisotropic structure in the upper mantle. For example, can the surface- and body-wave data sampling the western Pacific be satisfied by an anisotropic model in which the anisotropy is confined to the seismic lithosphere, or does the data require an additional component of anisotropy in the low-velocity zone below the lid? We evaluate a number of models with variable depth extent of the anisotropy, and we allow the anisotropy to terminate discontinuously if the data prefer, rather than enforcing a smooth distribution. The fact that discontinuities in velocity structure represent rapid changes in mechanical, phase, or compositional structure implies that they may be present in anisotropic structure as well. This hypothesis proves quite fruitful in developing a model of an anisotropic mechanical boundary layer with a sharp lower boundary beneath Australia. In contrast, the apparent continuity of anisotropy across the lid/LVZ boundary beneath the Pacific has very different implications for the mechanical structure in this region.

It should be clear from this discussion that when considered together, observations of anisotropy, velocities, and discontinuities provide deep insight into the mechanical and dynamical structure of the upper mantle. This thesis is organized in two major sections; one discusses the upper mantle beneath an old ocean basin (the western Pacific), and one focuses on the upper mantle beneath an ancient, stable continent (western Australia). Chapter 2 presents model PA5, which is our preferred one-dimensional radially anisotropic model for the western Pacific. This chapter describes in detail our analysis and inversion procedure, including data selection, cross-correlation analysis, model parameterization,

inversion incorporating a variety of prior constraints, and the preferred and alternative models. In Chapter 3 we explicitly test the hypothesis that anisotropy beneath the seismic lithosphere in the western Pacific is caused by large-scale alignment of olivine correlated with the motion of the Pacific plate. We turn our attention to continental upper mantle in Chapter 4, where we present model AU3, our preferred radially anisotropic model for western Australia. In Chapter 5 we discuss a model for the Lehmann discontinuity beneath continents, which has long been an enigmatic feature of the upper mantle. This model results from the joint consideration of upper mantle anisotropy beneath Australia, the observed L discontinuity, and the mean velocity profiles of both oceanic and continental upper mantle (PA5 and AU3, respectively). We conclude in Chapter 6 with a comparison between the models and a preview of new directions.

FIGURE CAPTIONS

Fig. 1.1. Regional, isotropic, one-dimensional models of upper mantle structure in oceanic and continental regions. Models PA2 and EU2 are Pacific and Eurasian-shield models, respectively, designed to fit Rayleigh waves [*Lerner Lam and Jordan*, 1987]; they thus primarily represent v_{SV} in a radially anisotropic model. Models ATL and SNA are Atlantic and North American-shield models, respectively, designed to fit refracted *SH* body waves [*Grand and Helmberger*, 1984a,b]; they thus primarily represent v_{SH} in a radially anisotropic model. While the continental models are clearly faster than the oceanic models throughout the depth range from 220 km to 400 km, the meaning of this observation has been questioned because of the different data-types and modeling assumptions (isotropy) used in generating the models. Our analysis will generate similar models using a self-consistent, three-component, radially anisotropy modelling analysis.

Fig. 1.2. Schematic representation of the discontinuous structure of the upper mantle inferred from *ScS* reverberations, along a hypothetical cross-section extending from a continental craton (left), across an active subduction zone (center), into an ocean basin (right). Tectonic regions are noted along the top, and depth divisions of Bullen are noted on the left. Upper-mantle discontinuities are designated by letter, while transition-zone discontinuities are denoted by their average depth. Interpretation of discontinuity structure in terms of major facies boundaries in a peridotitic composition is given on the right: Ol, olivine; Sp, spinel; Gt, garnet; β, beta phase of olivine; γ, gamma phase of olivine; Pv, perovskite; Mw, magnesiowustite; Il, garnet in ilmenite structure. In this thesis we further our understanding of this structure by constraining the anisotropic velocities within the regional discontinuity structure appropriate for an old ocean (regions B and C in the figure; Chapter 2) and a stable continent (regions P and S; Chapter 4). Figure is from *Revenaugh and Jordan* [1991c].

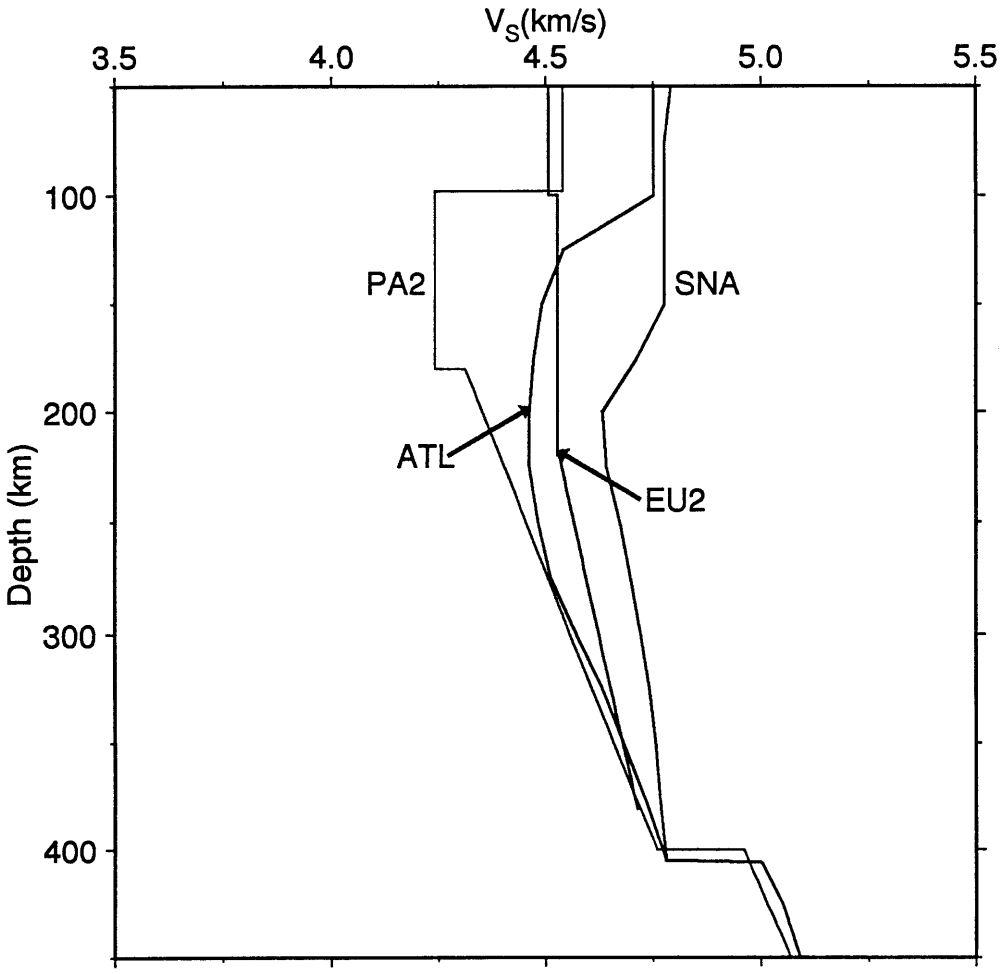

Figure 1.1

Revenaugh and Jordan (1991)

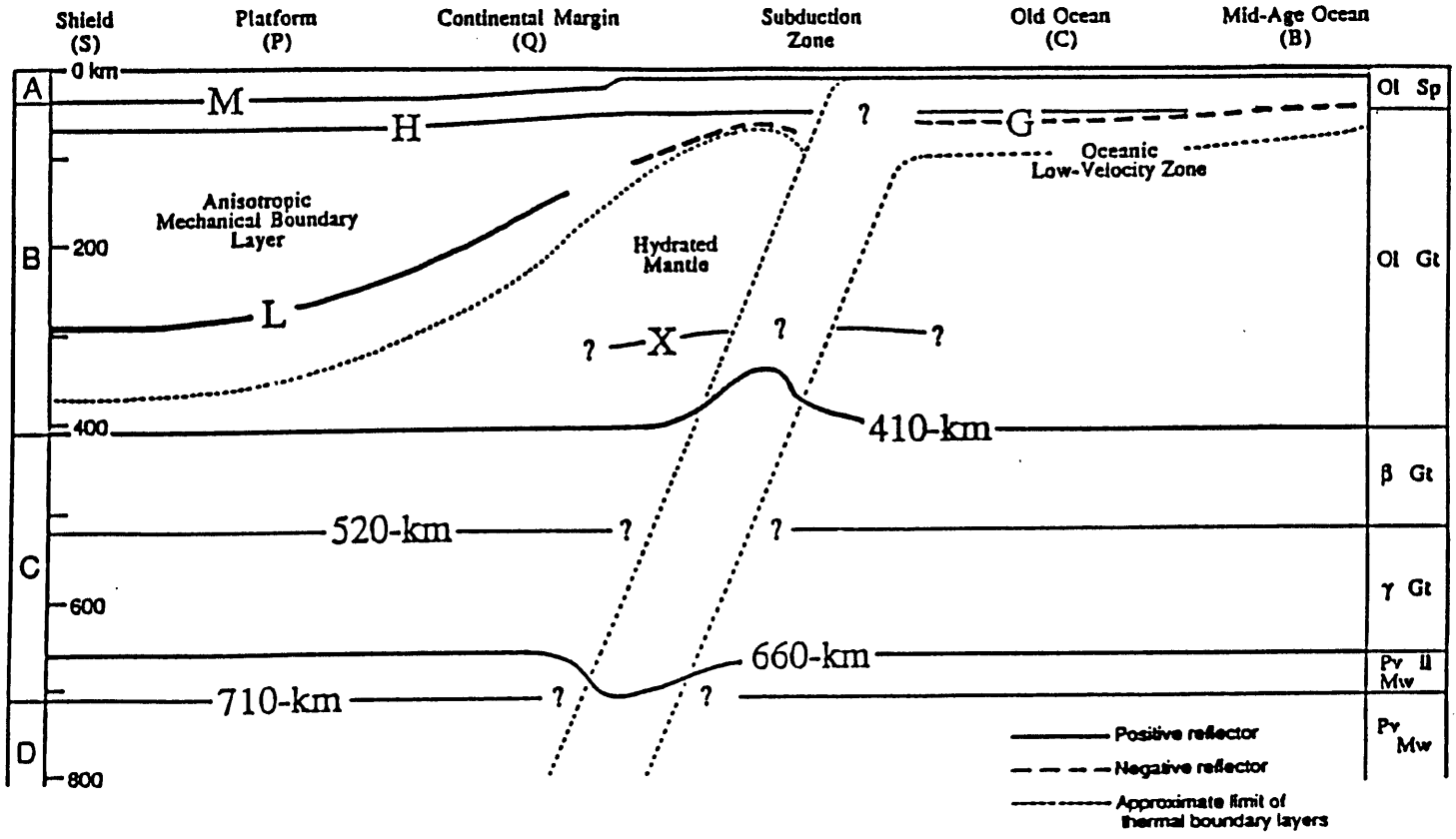

Figure 1.2

CHAPTER 2

A Radially Anisotropic Model of the Upper Mantle in a Western Pacific corridor

The Pacific basin provides an excellent environment for analyzing oceanic upper mantle structure. The large plate size surrounded by numerous source regions allows for isolation of a narrow range of tectonic ages, minimizing the effects of plate-related lateral heterogeneity. We focus on one particularly simple corridor in the older portion of the western Pacific, the path between the Tonga-Fiji seismic zone and the island of Oahu, Hawaii (Figure 2.1). The age (and thus bathymetry) of this profile is relatively homogenous; it traverses oceanic lithosphere with ages between 100-125 Ma (from magnetic lineations), and it has a bathymetric depth of ~5 km and sediment thickness of ~200 meters [*Ludwig and Houtz*, 1979]. The corridor avoids the Pacific Superswell [*McNutt and Fischer*, 1987], and it crosses only the eastern margin of the Darwin Rise (in particular the Line Islands), a region of prolific Cretaceous volcanism [*Menard*, 1984; *Larson*, 1991]. The current plate motion relative to a hot-spot reference frame is roughly perpendicular to the path [*Gripp and Gordan*, 1991].

Lateral variations in velocity structure have been observed in this region; tomographic models [e.g. *Zhang and Tanimoto*, 1993; *Su et al.*, 1994] typically show low-velocity regions (~ 1% slow) throughout the upper mantle beneath both Tonga/Fiji and Hawaii, with a relatively fast lithosphere between them. In addition, travel times of multiple-*ScS* phases show large along-path variations [*Sipkin and Jordan*, 1980a; *Gee*, 1994] that possibly arise from velocity anomalies in the upper mantle. Our approach averages such heterogeneity in order to focus on radial anisotropic structure. This chapter presents the first application of the procedure, including details on our choice of parameterization, data processing, and inversion.

RADIAL ANISOTROPY

Seismic anisotropy describes the phenomena by which seismic waves traveling in different directions or with different polarizations travel with distinct velocities [e.g. *Anderson*, 1989]. We require a spherically symmetric model that can address observed differences in tangential- and vertical seismograms (the Love-Rayleigh (*LR*) discrepancy and other forms of polarization (*SH-SV*) anisotropy); we therefore choose a radially anisotropic (transversely isotropic) parameterization. This type of anisotropy is characterized by five elastic parameters: v_{PH} and v_{PV} are the speeds of *P* waves propagating horizontally and vertically, respectively; v_{SH} is the speed of a horizontally propagating, transversely polarized shear wave; v_{SV} is the speed of a shear wave propagating either horizontally with a vertical polarization, or vertically with horizontal polarization; and η governs the variation of the shear and compressional wave speeds at oblique propagation angles. Radial anisotropy thus accounts for polarization anisotropy, as well as differences in vertical and horizontal propagation directions. It cannot directly account many other characteristics of seismic data that are usually attributed to anisotropy: azimuthal variation in *Pn* velocities and long-period surface waves [*Hess*, 1964; *Forsyth*, 1975; *Shearer and Orcutt*, 1986; *Montagner and Tanimoto*, 1991]; splitting of vertically propagating shear waves [*Ando et al.*, 1983; *Silver and Chan*, 1991; *Vinnik et al.*, 1992]; and coupling of long-period surface waves [*Kirkwood and Crampin*, 1981a; *Yu and Park*, 1994]. However, it is probable that polarization anisotropy arises from the same source as these observations, namely olivine alignment in the upper mantle [e.g. *Estey and Douglas*, 1986; *Nicolas and Christensen*, 1987]. As long as our data exhibit polarization anisotropy, a radially anisotropic model can address important first order issues such as the depth distribution of anisotropy, and its average magnitude along a path, even if the true anisotropy has a more general (azimuthal) form [*Lévêque and Cara*, 1983, 1985; *Maupin*, 1985; *Cara and Lévêque*, 1987, 1988]. By comparing radially anisotropic models for

different azimuths (Chapter 3) we can begin to make inferences on hypothesized azimuthal components of the anisotropy.

ScS REVERBERATION DATA

Our analysis starts with the reflectivity results of *Revenaugh and Jordan* [1991a,c], specifically the vertical travel times (t_v) to and shear impedance (R_o) contrasts across discontinuities within the western Pacific corridor. Shear impedance is defined as

$$R_o = \frac{\rho^- v_{sv}^- - \rho^+ v_{sv}^+}{\rho^- v_{sv}^- + \rho^+ v_{sv}^+}$$

where ρ_{sv}^- and v_{sv}^- are the density and *SV* velocity just below a given discontinuity, respectively, and ρ_{sv}^+ and v_{sv}^+ are the velocity and density above the discontinuity. The reflectivity profile for this corridor (Figure 2.2) is characterized by a Gutenburg (G=lid/LVZ, near 70 km depth), 410-km, 520-km, and 660-km discontinuities. Notably absent is evidence for the Hales discontinuity (~50 km depth), perhaps because it is obscured by the large G [*Revenaugh and Jordan*, 1991c]. Also missing is the Lehmann discontinuity (~220 km depth), which is ubiquitously observed on paths with a significant continental component [*Revenaugh and Jordan*, 1991c]. This profile nicely characterizes the upper mantle of regions B and C in Figure 1.2.

Table 2.1 presents t_v and R_o for the Moho, G, 410-km, 520-km, and 660-km discontinuities. The observed discontinuity structure is roughly compatible with model PA2 of *Lerner Lam and Jordan* [1987], which is constructed to fit Rayleigh waves from the western Pacific. We choose PA2 as the starting model for our inversion, and calculate residuals of the *ScS*-reverberation observations relative to it. There are two discrepancies between the observations and PA2. The latter has an L discontinuity with a positive impedance contrast, whereas no discontinuity is observed near this depth on this path. We retain a second-order discontinuity near this depth to allow for two distinct gradients

between G and 410 km, and assign the discontinuity an impedance of $R_Q = 0.0 \pm 0.005$ and an unconstrained vertical travel time. In addition, a discontinuity near 520-km depth is observed on this path. PA2 does not does not have such a feature, and a positive impedance residual is calculated for a depth appropriate for the observed travel time. The partial derivatives of these data with respect to our model parameters are straight-forward to calculate from ray theory and plane-wave reflection coefficients [*Revenaugh and Jordan*, 1989]. We summarize them in the Appendix.

Multiple *ScS* and *ScS* reverberations also provide knowledge of Q_{ScS} along this corridor, including Q estimates for upper- and lower-mantle layers (Figure 2.2) [*Sipkin and Jordan*, 1980a; *Revenaugh and Jordan*, 1987, 1991a]. These values are necessary for the body- and surface-wave analysis described in the next section. The whole mantle Q_{ScS} estimate is 169 ± 30, with $Q_{UM} = 82 \pm 18$ and $Q_{LM} = 231 \pm 60$ [*Revenaugh and Jordan*, 1991a]. These estimates are slightly lower than the global values in PREM [*Dziewonski and Anderson*, 1981]. As we expect there to be a significant Q contrast between the lid, LVZ, and transition zone, we partition Q_{UM} into $Q_{LID} = 150$, $Q_{LVZ} = 30$, and $Q_{TZ}=150$; this assumption is validated by forward modeling. These Q values are maintained throughout our study.

THREE-COMPONENT BODY- AND SURFACE WAVE DATA

ScS reverberation data constrain the discontinuities in our model; the anisotropic velocities between discontinuities are determined using frequency-dependent phase delays of surface, multiply-reflected (*SS*, *sSS*, *SSS*), and direct (*S*) body waveforms extracted from 3-component, long-period seismograms of 55 earthquakes in the Tonga-Fiji region recorded at the GSN stations HON and KIP (Figure 2.1 and Table 2.2). The recorded seismograms are rotated into the tangential-radial-vertical coordinate system and low-passed with a zero-phase filter with a corner at 45 mHz. The earthquakes are all of moderate size ($M_w < 6.6$), minimizing unmodeled source effects, and range in source depth

from 10 km to 663 km and epicentral distance from 39°-58°. Evidence of anisotropy can be seen directly on the seismograms. For example, Figure 2.3a displays observed seismograms from a shallow-focus event, along with synthetic seismograms calculated for isotropic model PA2 (via mode summation, complete to 50 mHz, convolved with the Harvard CMT source mechanism). The initial phase of the observed Rayleigh wave is reasonably well matched by PA2, while the observed Love wave is clearly much faster than the synthetic. The magnitude of the misfit cannot be rectified by an isotropic model. Likewise, *SSS* observations from a deep focus event (Figure 2.3b) shows clear evidence of shear wave splitting, with SSS_H advanced by approximately 6 s relative to SSS_V. As we will see, these observations of polarization anisotropy can be satisfied by a radially anisotropic model with horizontal velocities that are greater than vertical velocities.

GSDF Analysis

We analyze these data using the Generalized Seismological Data Functional (GSDF) methodology of *Gee and Jordan* [1992], which uses accurate synthetic seismograms to isolate a general waveform on the seismogram and provides travel-time residuals for that waveform at several discrete frequency intervals. This methodology provides a self-consistent analysis of complex phases on three-component seismograms, and the frequency-dependent analysis of each isolated phase greatly increases the amount of information gleaned from the seismogram. Upper mantle phases recorded at teleseismic distances often incorporate considerable complexity, with many distinct phases arriving in a short time interval. Such phases are difficult to model in three-components with any single ray or normal-mode theory, requiring large-aperture arrays that limit analysis to continental regions [e.g. *Cara and Lévêque*, 1988]. GSDF accounts for interfering phases, and as a result these types of arrivals can be robustly analyzed [*Gee and Jordan*, 1992].

GSDF processing consists of (1) creating an "isolation filter", i.e. a synthetic seismogram of a chosen wave group calculated by performing a weighted sum of

eigenfunctions for a subset of modes selected by phase velocity, group velocity, and/or other characteristics; (2) cross-correlating the isolation filter with both the observed and complete synthetic seismograms, creating two broad-band correlation functions; (3) windowing the correlation functions in the time domain to reduce interference with other wave groups; (4) filtering the windowed correlation functions in several discrete narrow-band windows in the interval $10 \leq f_0 \leq 45$ mHz; and (5) extracting four time-like quantities (phase delay $\delta\tau_p$, group delay $\delta\tau_g$, amplitude delay $\delta\tau_q$, and attenuation delay $\delta\tau_a$) relative to the synthetic at each f_0 using a Gaussian wavelet approximation. These quantities completely describe the behavior of the observed waveform relative to the model-predicted behavior, including correction for interference from unmodeled wavegroups. In this analysis we focus on the phase delay ($\delta\tau_p$). A particularly powerful attribute of GSDF analysis is that it provides complete partial derivative kernels associated with each $\delta\tau_p$, leading to a straightforward solution to the linearized inverse problem. *Gee and Jordan* [1992] provide a detailed description of the GSDF procedure. As described in the Appendix, we have extended their formulation of the Fréchet kernels to include general radially anisotropic media.

GSDF Analysis: Examples

The advantages of the GSDF approach can best be summarized using a few examples. We first illustrate the process for a well-isolated body wave, a vertical-component *sSS* phase (Figure 2.4). Figure 2.4a displays the data, a full synthetic seismogram, and an isolation filter formed by summing the eigenfunctions for all excited modes with group velocities of 4.10-4.30 km/s and phase velocities less than 8 km/s; this process isolates the phase in time and eliminates contributions from core-interaction modes. Phase delays (frequency-dependent travel times, Figure 2.4b) are then calculated relative to the synthetic model by cross correlating the isolation filter with both the data and the full synthetic; the filter/data cross correlation provides the initial phase delay estimates, and the

filter/synthetic cross correlation captures the interference expected from wavegroups not modeled by the filter, for which the final phase delays are corrected. Since this waveform is well isolated with minimal interference from unmodeled arrivals, these corrections are less than a second and are not shown in the figure. One of the advantages of using the GSDF analysis is immediately apparent in the frequency trend in the phase delays. The *sSS* waveform is moderately dispersed relative to the synthetic model, with low frequencies arriving approximately as predicted, and higher frequencies arriving up to 8 s early. A narrow-band analysis of this body wave would record only one observation near the center frequency of the waveform (in this case, approximately -6 s at ~35 mHz). Each phase delay has a corresponding partial derivative kernel (Figure 2.4c), which provides the sensitivity of the observation to perturbations in the model. The frequency-dependent trend in phase delays is accompanied by a trend in the partials. At low frequency, this *sSS* phase is sensitive primarily to the average SV velocity in the upper mantle, with two broad peaks near 100 and 300 km depth. At higher frequency, the kernel becomes more oscillatory, and while it still roughly averages over the upper 600 km, it is more sharply peaked in the transition zone between 500 to 670 km depth. Vertical-component *sSS* is sensitive to all 6 parameters of the anisotropic model, but we plot only v_{SH} and v_{SV} for clarity (cf. Figure 2.7). Note that this vertical component *sSS* wave displays no sensitivity to v_{SH}.

The full power of GSDF analysis is illustrated using a multi-mode oceanic Love wave (Figure 2.5). Such phases are critical to inferring anisotropic structure in oceanic regions, but the lid/LVZ structure in oceanic regions results in very strong interference between the fundamental and higher modes. As a result, traditional measurements and interpretations of oceanic Love wave dispersion in terms of a single mode can be biased [*Boore*, 1969; *James*, 1971; *Forsyth*, 1975b]. Figure 2.5a contains an observed tangential-component seismogram from a shallow focus earthquake; the direct *S* and Love waves are the only observed phases in this time window. Also shown are a complete synthetic seismogram and an isolation filter (labeled Filt1) that is calculated via summation

of the fundamental mode branch. A comparison between Filt1 and the full synthetic indicates that the branch summation captures only a portion of the full Love waveform; the remainder of the waveform is made up of higher modes. The phase delays and partial derivatives require a significant correction to account for this interference (Figures 2.5b and 2.5c, with notation consistent with *Gee and Jordan*, [1992]). In Figure 2.5b, the symbols labeled $\delta\tau_p+\tilde{t}_p$ are the phase delays resulting directly from the cross-correlation of Filt1 with the data, where $\tilde{t}_p$ represents the correction terms determined from the cross-correlation of Filt1 with the full synthetic. The final phase delays ($\delta\tau_p$) that result from applying this correction term are up to 5 s slower than the initial estimates. Likewise, the partial derivative kernels (Figure 2.5c) corresponding to uncorrected $\delta\tau_p+\tilde{t}_p$ (labeled "Fund only", i.e. kernels containing only the contributions of the fundamental mode branch) are very different than the corrected kernels, which have a broader double peak that is more representative of the multimode nature of the full waveform. Clearly, if simple fundamental mode isolation filters and kernels are used to interpret the phase behavior of this waveform (as would be the case in typical surface-wave analyses), incorrect model perturbations would result.

The corrected phase delays and partial derivatives are quite accurate, and they are robust to a variety of choices for the isolation filter. Figure 2.6a contains the same data and full synthetic as in Figure 2.5, but now the isolation filter (labeled Filt2) is constructed by selecting all modes with group velocities of 4.14-4.54 km/s and phase velocity < 8 km/s (much like the "body wave" filter shown in Figure 2.4). Unlike Filt1, Filt2 clearly represents a good match to the full synthetic Love wave, and the correction terms $\tilde{t}_p$ for this filter are negligible ($\tilde{t}_p < 0.7$ s). The final $\delta\tau_p$ and partial derivative kernels for both filters are compared in Figures 2.6b and 2.6c, respectively, and they are nearly identical. The corrections applied to the phase delays and partial derivative kernels corresponding to the Filt1 accurately account for interference with modes not incorporated in the filter itself.

Similar results are found for filters constructed by summing either the 1st or 2nd higher mode branches, which contribute significantly to the full Love waveform.

GSDF Partial Derivatives

We generate isolation filters for all observed R_1, G_1, *S*, *SS*, *sSS*, and *SSS* waveforms with sufficiently high signal-to-noise ratio; a total of 233 waveforms from the 55 events. Nearly 1500 frequency-dependent phase delays are extracted from the 233 waveforms. Representative partial derivative kernels for each of these phase types (Figures 2.4, 2.6, and 2.7) demonstrate the sampling by these data of upper-mantle structure. While the surface wave kernels (Figures 2.6c and 2.7a) are confined to the upper 400 km of the mantle, the *SSS* and *SS* kernels (Figures 2.4c and 2.7b) sample the upper 600 km in various ways, increasing our resolution of anisotropic structure in the sublithospheric mantle beyond that provided by surface waves alone. The *S* wave (Figure 2.7c) also averages over much of the upper mantle and transition zone, with a peak near its ray-theoretical turning point at ~1000 km.

The frequency-dependent variability of surface waves is well-known (Figure 2.7a, for example), but frequency dependence of "body" waves is relatively unexplored. The frequency dependence of an *sSS* wave was discussed above; similar behavior can be observed in Figures 2.7b,c for *SS* and *S* phases. Rayleigh waves have non-negligible sensitivity to density, *P* velocities, and η [*Anderson and Dziewonski*, 1982; *Regan and Anderson*, 1984] (Figure 2.7a), and it is clear from our kernels that this holds for other *SV*-type phases (Figure 2.7c), reinforcing the importance of inverting for the full radially-anisotropic model.

It is interesting to compare how the different components of an arrival differ in their radial sampling of the mantle. Figure 2.8 presents partial derivative kernels for vertical- (Figure 2.8a) and tangential- (Figure 2.8b) component *sSS* waves. At low-frequency, the sensitivity with depth is similar; sSS_V has a v_{SV} kernel double-peaked in the upper 400 km,

and sSS_H has a similar v_{SH} kernel. At higher frequency, however, the two components have substantially different kernels. The v_{SV} kernel for sSS_V is peaked near 400 km, with oscillatory behavior in the upper mantle and a broad tail extending to 700 km depth. The v_{SH} kernel for sSS_H is more sharply peaked in the transition near 500 and 670 km, and it's sensitivity to v_{SH} in the upper mantle, while still oscillatory, is of lower amplitude relative to the transition zone peaks. In addition, note that at both low and high frequencies, tangential component phases such as *sSS* have non-negligible sensitivity to v_{SV}, especially in the shallow mantle. This is in contrast to the vertical component phases, which are relatively insensitive to v_{SH}. These kernels imply that a bias might exist in the shallowest portions of the isotropic shear velocity models generated from analysis of tangential-component seismograms [e.g. *Grand and Helmberger*, 1984a,b; *Sheehan and Solomon*, 1991; *Woodward and Masters*, 1991; *Grand*, 1994].

GSDF Analysis: Summary

Figure 2.9 summarizes the 1497 phase-delay observations from all 55 events. All phase delays have been corrected for ellipticity, receiver, and source anomalies, which are calculated by averaging the tangential and vertical broad-band *S*-wave delays for each event. The large difference in the Love and Rayleigh wave residuals (5-25 s) relative to isotropic model PA2 is the *LR* discrepancy, and points to the presence of anisotropy in the upper mantle. In addition, the strong frequency-dependent trend in the Rayleigh-wave residuals indicates that PA2 does not correctly predict the Rayleigh-wave dispersion; the trend of this relative dispersion favors a thinner lid and/or a slower LVZ. The Love wave phase delays reflect the interference between the fundamental and higher modes (as shown above), and thus are not strongly dispersed relative to PA2, though they are much faster. Shear-wave splitting is observed in the *SS* and *SSS* phases, with the SSS_H and SS_H phases being advanced by up to 8 s and 4 s, respectively. This apparent splitting is frequency-dependent, with low-frequency observations more split than high-frequency

observations. The low-frequency *SSS* and *SS* observations are more sensitive to the shallow upper mantle than the high-frequency observations (see Figures 2.4, 2.7, and 2.8), and thus this frequency-dependence places strong constraints on the depth extent of anisotropic structure. The *S* waves show little evidence of splitting or relative dispersion, further indication that the anisotropy is predominantly shallow (above the transition zone). These inferences on anisotropy are approximate, of course; although tangential-component shear waves are labeled with the subscript H, and radial- and vertical-component observations carry the subscript V, we have seen from the partial derivative kernels that the connection of S_H phases to v_{SH} is not direct, and likewise for S_V and v_{SV}, and the different components can have differing depth sensitivity. The inversion for anisotropic structure incorporates these complexities.

INVERSION

To invert our *ScS*-reverberation and turning-wave data set for an improved upper-mantle model, we discretize the model space into an M-dimensional vector, where the M model parameters include the depth to each discontinuity, and the seismic velocities and density and associated linear gradients in each layer. The use of linear gradients is justified because mineral physics [*Bass and Anderson*, 1984; *Weidner*, 1985; *Ita and Stixrude*, 1993] and seismic data [*Grand and Helmberger*, 1984a, b; *Lerner-Lam and Jordan*, 1987; *Nolet et al.*, 1994] indicate that except for at discontinuities, upper mantle velocities vary slowly with depth, allowing them to be described by linear segments if the number of layers is sufficiently large. We could choose alternative parameterizations such as continuous or higher-order polynomial descriptions, but our ability to satisfy the data with a linear parameterization indicates that additional complexity is unwarranted. The seven-layer models presented have a total of 97 parameters.

Assuming this model parameterization, we follow a Bayesian approach [*Tarantola and Valette*, 1982; *Tarantola*, 1987] and construct a probability density function that

describes our prior state of knowledge of the model space. This function is specified by estimates of the model parameters (and functions of the model parameters) $\mathbf{m}_{prior}$, along with Gaussian uncertainties described by the covariance operator $\mathbf{C}_m$. Our prior knowledge takes on several forms drawn from seismological, geological, and mineralogical information. First, for shear velocities though the bulk of the upper mantle and transition zone, we assume $m_{prior} = m_0$ (where m_0 is the value of the model parameter in the starting model) with a large variance, typically 0.5 km/s (although smaller values are specified in the LVZ due to especially strong non-linearity in this part of the model). These parameters are well-constrained by our seismic observations, so this allows them considerable freedom to satisfy the data. In addition, in the crust and shallowest portion of the mantle, we have good estimates of the velocities and density from rock samples and shallow seismic refraction data [e.g. *Shearer and Orcutt*, 1986]. These values of m_{prior} have smaller variances, more typically 0.1 km/s and 0.1 g/cm^3 for density.

We also incorporate knowledge on the density and bulk sound velocity (v_ϕ, where $v_\phi^2 = v_P^2 - \frac{4}{3}v_S^2$) of the upper mantle estimated for a pyrolite mineralogy [*Ita and Stixrude*, 1993]. These parameters can be measured reasonably well in the laboratory [e.g. *Zaug et al.*, 1993], and they are complementary to our shear wave data. We note that the choice of this particular composition is not important; the bulk sound velocity and density profiles for pyrolite are nearly identical (within assigned errors) to those for high-aluminum piclogite [*Ita and Stixrude*, 1993]. The density is also similar to that of PREM [*Dziewonski and Anderson*, 1981], differing only where the discontinuity structures differ. These constraints are applied at several discrete depths between 200 and 800 km (Figure 2.10); an error (1%) is assigned to each observation via covariance between v_S and v_P (and a variance for ρ) at each depth. The constraints also specify that both density and bulk sound velocity should be first-order continuous everywhere except at the phase-change discontinuities at 410 km and 660 km. This requirement is loosened slightly at the 520-km

discontinuity, where some mineral physics data indicate a density jump [*Rigden et al.*, 1991].

The prior probability function provides a mechanism to test hypotheses on the distribution of anisotropy. We selectively enforced isotropy (i.e. $v_{SH}=v_{SV}$, $v_{PH}=v_{PV}$, $\eta=1$) at the top and/or bottom of individual layers, systematically solving for models with different regions allowed to be anisotropic. By evaluating the misfit of each resulting model, we test hypotheses on the necessity of anisotropic structure within each layer, as well as the trade-offs of allowing anisotropy within particular combinations of layers. Furthermore, in anisotropic layers we constrain η using the values in PREM; this is supported by mineralogical calculations of expected values of η [*Nataf et al.*, 1986; *Montagner and Anderson*, 1989].

If we also assume some prior knowledge of the data space in the form of our observations and a prior data covariance matrix $\mathbf{C}_d$, we can solve for a probability density function that specifies the posterior knowledge of the model space, given the prior knowledge summarized above. When the distributions are Gaussian, the center of the posterior probability density distribution can be written as [*Tarantola*, 1987]:

$$\delta\mathbf{m} = [\mathbf{G}^T\mathbf{C}_d^{-1}\mathbf{G} + \mathbf{C}_m^{-1}]^{-1}[\mathbf{G}^T\mathbf{C}_d^{-1}\delta\mathbf{d} + \mathbf{C}_m^{-1}(\mathbf{m}_{prior} - \mathbf{m}_o)].$$

The vector $\delta\mathbf{m}$ represents the perturbations to the discretized model; the data vector $\delta\mathbf{d}$ contains 1497 frequency-dependent travel time residuals, 7 vertical travel time residuals, and 6 discontinuity impedance contrast residuals; perturbation matrix $\mathbf{G}$ incorporates the partial derivatives described in the previous section and the Appendix; and $\mathbf{m}_o$ is the starting model. The iteration we employ is a complete one: we recalculate the frequency-dependent travel times and partial derivative kernels using new synthetics and isolation filters for an improved model. The models presented here represent three complete iterations. Convergence is assured by comparing the data with forward predictions calculated from the final models.

The observations are assumed to be independent (in that $\mathbf{C}_d$ is diagonal), with prior variance estimates assigned based on the quality and resolution expected for the observation. For the frequency-dependent travel times, error estimates range from 2 s for a high-quality, high-frequency (40 mHz) observation to 10 sec or larger for a low quality, low-frequency (10 mHz) observation. We have estimated the variance of the *ScS* reverberation observations by considering the brightness of the reflector. The error estimates range from 0.005 for δR_o and 1.0 s for δt_v for the well-resolved 660 km and 410-km discontinuities, to 0.01 and 2.0 s for the more poorly resolved 520-km discontinuity.

The formal *a posteriori* model variance and resolution resulting from the inversion provide estimates of model errors, but they are difficult to interpret because of the underlying assumptions built in via our model parameterization. In general, the probability density function specifying our prior knowledge of the data and model space provides good resolution of our model parameters. We have estimated the posterior errors using a variety of guides: the formal error estimates; the variability of the model solution with different combinations of data and parameter variances and prior constraints; and forward modeling of waveforms using the resulting model. These estimates are qualitative, but they reflect the true errors much more accurately than the formal errors provided by the inversion alone. The parameters best-resolved by the data are the depths to discontinuities, the vertical shear impedance contrasts (i.e. a combination of v_{SV} and density), and the shear velocities; the *P* velocities, η, and density between discontinuities are also well-resolved, but only under the assumption that the prior mineralogical constraints are well-determined.

As is shown below, our final model provides an excellent fit to the prior seismological and mineralogical constraints; in fact, we do not at all compromise our fit to the data by applying them, indicating that the mineralogical and seismological data are entirely self-consistent. As discussed in Chapter 6, this methodology appears quite promising for joint inversions of seismological and mineral physics data to test

hypothesized mantle mineralogies. In addition, a later section discusses the successful application of prior constraints to test various hypotheses of anisotropic structure.

MODEL PA5

Our preferred model (termed PA5) for the western Pacific corridor from Tonga/Fiji to Hawaii is presented in Figure 2.11 and Table 2.3. PA5 is characterized by a high velocity (v_{SH} = 4.84 ± 0.02 km/s), thin, anisotropic lithosphere, bounded at 68 ± 4 km depth by a large, negative G discontinuity; high v_{SH} (4.56 ± 0.02 km/s) at the top of the LVZ, with a strong negative gradient leading to a minimum velocity (4.34 ± 0.04 km/s) at 166 ± 20 km depth; v_{SV} in the lid of 4.65 ± 0.03 km/s; low v_{SV} at the top of the anisotropic LVZ (4.37 ± 0.03 km/s) with a slight negative gradient to a velocity of 4.26 ± 0.04 km/s at 166 km depth; and an isotropic high-gradient region from 166 km depth to the 410-km discontinuity. The transition zone discontinuities are located at 415 ± 3 km, 507 ± 10 km, and 651 ± 4 km. The shear anisotropy is 3.8 ± 0.5% in the lithosphere, 4.1 ± 0.5% at the top of the LVZ, and grades to nearly zero at the base of the LVZ; the small discontinuity at the base of the anisotropic region is below the detection level of *ScS* reverberations. The accompanying P anisotropy is approximately 1.7 ± 1.5% through the lid and into the LVZ. The gradient between 166 km and the 410 discontinuity is quite steep, and the velocities in this depth range and into the transition zone are nearly identical to those found in regional isotropic oceanic models ATL [*Grand and Helmberger*, 1984a] and PA2 [*Lerner-Lam and Jordan*, 1987], which are designed to fit long-period SH and PSV waveforms, respectively. The final density and bulk sound velocity profiles generally satisfy the mineralogical constraints (Figure 2.10).

The fit to our data is summarized in Figure 2.9 and Table 2.1; over 90% of the variance observed relative to PA2 is explained by PA5. The *SH-SV* differences observed in the surface wave, *SSS* and *SS* phase delays have been eliminated, the relative dispersion is removed, and the *ScS*-reverberation data is now largely satisfied. Two apparent

inconsistencies are found in the *ScS*-reverberation data. The impedance contrast across the Moho must be larger than the *ScS* data indicate in order to maintain reasonable crustal velocity and density values. Also, the travel time to and impedance contrast at the G discontinuity is difficult to fit without thinning the lid further and raising lithospheric v_{SH} above 4.9 km/s, higher than typically observed *Sn* velocities from the central Pacific. The largest reported *Sn* velocity is 4.88 ± 0.12 km/s, observed just east of the Izu trench in the western Pacific [*Shimamura et al.*, 1977], and the large majority of Pacific *Sn* observations consistently show velocities less than 4.8 km/s [e.g. *Walker*, 1977]. These observations place rough constraints on our models, although they are not strictly applied because they represent much higher frequency (~1 Hz) propagation, and because the measured travel times of the emergent *Sn* phase within the *P* coda may be systematically biased towards slower times. In addition, the G discontinuity is be one of the more difficult discontinuities to extract reflectivity information from, owing to possible interference from other shallow upper-mantle reflectors such as M and H [*Revenaugh and Jordan*, 1991c]; therefore, the 2-s t_v residual and 2% R_o residual relative to PA5 may be within realistic error estimates. An alternative model which fits the travel time to G has the same general anisotropic characteristics, and our conclusions do not change regarding these characteristics. Finally, our model poorly predicts the whole-mantle *ScS* travel time. We have fit this datum as well as possible within the context of an upper mantle parameterization, and conclude that the structural differences responsible for this misfit are located in the lower mantle or at the core-mantle boundary. In fact, lower-mantle heterogeneity along this path [*Su et al.*, 1994] can almost entirely account for the remaining residual. This structure is being further analyzed using *ScS* reverberations [*Katzman and Jordan*, 1995].

A simple (though qualitative) evaluation of PA5 can be made by visual comparison of data and synthetic waveforms. Figure 2.12 presents a suite of observed seismograms that characterize our data set, along with full mode-synthetic seismograms calculated for PA5 (data and synthetics low-passed at 45 mHz; the dominant energy is ~35 mHz). These

events are truly representative of our data set in that they were chosen not because of the particularly good fit between data and synthetic, but rather because they represent a variety of source depths and distances with strong signal on both tangential and vertical components. All phase types are represented, including *S*, *R1*, *G1*, and (for 870907) *SS* from shallow events, *S*, *SS*, and *sSS* from intermediate events, and *S*, *SS*, and *SSS* from deep events. While there are obvious variability and misfit in some cases, the overall fit to this complex suite of waveforms is quite good, especially considering the additional complexity added by interfering phases such as *sS*, *ScS*, and *sScS*; in fact, observable misfit is almost always in a region of *ScS* interference (primarily because of the unmodeled lower mantle heterogeneity mentioned above).

DEPTH EXTENT OF ANISOTROPY: ALTERNATIVE MODELS

Model PA5 contains anisotropic structure between M and 166 km depth, throughout the lid and LVZ. Can alternative distributions of anisotropy provide acceptable fits to the data within the context of our prior knowledge? Azimuthal variations in *Pn* velocity [*Shearer and Orcutt*, 1986] convincingly demonstrate that oceanic lid is anisotropic, so we first explored the possibility that our data can be satisfied if the anisotropy is explicitly restricted to this region, with the LVZ and deeper regions strictly isotropic. This hypothesis was rejected because the *SH* velocity in the lid (>5.0 km/s) in such models is much greater than the highest observed *Sn* velocities, and because such models could not explain the complex interference effects observed in the multi-mode Love waves across our distance interval. Figure 2.13 displays a transversely polarized seismogram (Δ=39.8°), with the direct *S* wave arriving at ~13.5 min and the emergent Love-wave group at ~16 min. The trace labeled PA3 is a complete synthetic seismogram for an earth model where anisotropy is restricted to the lid [*Gaherty et al.*, 1992]. Synthetics of the first four mode branches for this model are displayed above the full synthetic (*topmost traces*), showing that the impulsive, large-amplitude Love wave results from the constructive interference

among the 0th, 1st, and 2nd mode branches. (Note that the first two overtones are larger in amplitude than the fundamental mode.) It is very difficult to dephase these branches to generate an emergent waveform by adjusting the lid velocity; models with *SH* velocities less than ~4.4 km/s at the top of the LVZ generally produce impulsive waveforms of this type, regardless of lid velocity. In comparison, the trace labeled PA5 is a complete synthetic for our preferred model with anisotropy extending into the LVZ. The increased *SH* velocity in the LVZ enhances and advances the 0th and 1st mode branches (shown in *lowermost traces*), thereby generating a complete synthetic with emergent, dispersed behavior similar to that observed in the data. The exact timing of the various peaks reflects not just high v_{SH} in the LVZ; it also reflects the velocity just at the top of the steep gradient region running from 170 km to 410 km depth, which strongly affects the behavior of the first higher mode. If this velocity is even slightly faster than in PA5, then the first two peaks of the Love wave will be large and early. If it is slightly slower, than these peaks will be late. Waveforms such as these lock in the *SH* velocities through the LVZ and into the high-gradient region. The dispersive characteristics observed in the Rayleigh waves require low *SV* velocities through the LVZ, and thus we reject the hypothesis that anisotropy is limited to the lid.

The alternative hypothesis that anisotropy extends to the base of the LVZ results in PA5. If anisotropy is allowed throughout the upper mantle to the 410-km discontinuity, the magnitude is constrained to be small (roughly less than 1%) below an approximate depth of 170 km by the *SS* and *SSS* splitting data. Such models yielded no observable improvement in the fit to the data relative to PA5, and we conclude that the Pacific data are consistent with anisotropy constrained above 170 km depth.

This result differs somewhat from previous analyses of anisotropy beneath the Pacific using long-period fundamental- and higher-mode surface waves. The depth extent of anisotropy in these studies ranged from 220 km [*Regan and Anderson*, 1984] to over 300 km [*Nataf et al.*, 1986; *Cara and Lévêque*, 1988; *Nishimura and Forsyth*, 1989]. Our

combination of surface-wave and multiply-reflected body-wave data is inconsistent with significant (>1%) anisotropy extending to such depths.

LID AND LVZ STRUCTURE

The lid and LVZ structure are two features of PA5 that are very well resolved by our study. The lid is substantially thinner than that inferred from a recent global model [*Zhang and Tanimoto*, 1993; *McNutt*, 1994], and it implies that the lid beneath 100 Ma ocean is no thicker than that observed directly beneath Hawaii [*Bock*, 1991]. In addition, the large lid/LVZ contrast in our anisotropic model refutes the contention [*Anderson and Dziewonski*, 1982] that large contrasts between these features are artifacts of incorrect isotropic inversion procedures. Correct inferences about this structure are very important for understanding phenomena such as cooling of oceanic lithosphere, partial melting, rheology, and dynamics in the asthenosphere [e.g. *Forsyth,* 1977*; Jordan et al.*, 1989]. We stated in Chapter 1 that our regional radial models better characterize some aspects of upper-mantle structure than current three-dimensional parameterizations. The lid and LVZ structure of oceanic upper mantle represent one example.

As evidence supporting this claim, we contrast the lid and LVZ structure in PA5 with that found in the 1-D path-average projection of the global 3-D model S12_WM13 [*Su et al.*, 1994] along the Tonga-Hawaii path (Figure 2.14). S12TH is constructed by averaging the shear velocity perturbations at each depths along the short-arc path between Tonga and Hawaii (Figure 2.1). The resulting isotropic *S* wave perturbations as a function of depth were then applied to v_{SH} and v_{SV} in PREM. The differences are dramatic: PA5 is over 4% faster than S12TH throughout the lid, while S12TH is much faster below the 220 km discontinuity. S12TH also maintains a flat gradient from 220-km to 400-km depth. Low lid velocities and a 220-km discontinuity with high velocities just below it are characteristic of PREM (the starting model for the S12_WM13 inversion), and they remain in S12_WM13, probably because of that model's reliance on long-period surface waves to

constrain upper-mantle structure. Such data essentially average the upper 300 km of the mantle (Figure 2.15a), and therefore they cannot distinguish between PA5 and S12_WM13. The higher-frequency data incorporated in our study can easily distinguish between these two models (Figure 2.15b), and PA5 is clearly preferable. We note that S12_WM13 was constructed to fit data with frequencies less than 30 mHz, and therefore should not necessarily be expected to match data above this frequency. Extremely strong gradients in radial velocity structure are clearly required by such data, however, and such features apparently are not resolvable with the lower-frequency data and/or radial parameterizations currently incorporated in 3D models. Regional models can incorporate the higher-frequency data that resolve such structure; PA5's lid and LVZ structure is quite similar to that found for the 52-110 Ma portion of the Pacific from a regionalized analysis [*Nishimura and Forsyth,* 1989], despite substantial differences in data and model parameterization (Figure 2.16).

The steep velocity gradient between the base of the LVZ and the 410-km discontinuity appears to be a robust feature of oceanic upper mantle. This gradient is very well-resolved by our data (Figure 2.13), and the velocities in this range are nearly identical to those observed in the North Atlantic [*Grand and Helmberger*, 1984a], the East Pacific Rise [*Grand and Helmberger*, 1984b], and the Northwest Pacific [*Lerner-Lam and Jordan*, 1987] (Figure 2.16). In contrast, the gradient in this region in S12TH is much lower, similar to typical continental models [*Grand and Helmberger*, 1984b; *Lerner-Lam and Jordan*, 1987; see Chapters 4 and 5].

TRANSITION ZONE STRUCTURE

The combination of *ScS*-reverberation data with *SS* and *SSS* travel times makes PA5 an excellent average model for examining the transition zone structure beneath the central Pacific. *Revenaugh and Jordan* [1991b] demonstrate that the general thermal properties of the transition zone can be inferred from the vertical travel times extracted from

ScS reverberations, yet such inferences are dependent on mapping the travel times into a depth estimate through an assumed velocity model. The addition of *SS* and *SSS* data allows us to fix the location of the discontinuities in velocity and depth, providing a more concrete analysis of variability in depth and strength of the reflectors. In addition, we now have good estimates of the gradients between the discontinuities, which are particularly important for evaluating the mineralogy of the transition region [*Bass and Anderson*, 1984; *Duffy and Anderson*, 1989; *Ita and Stixrude*, 1993]. We defer the bulk of this discussion for Chapter 6; here we present the general properties of PA5's transition zone.

The location of the "410" is at 415 ± 3 km depth. This is somewhat deeper than that in either ATL or PA2 (Figure 2.16), but it is nearly identical to the average value (414 ± 2 km) reported for the southwest Pacific and Australasia by *Revenaugh and Jordan* [1991b]. The magnitude of this discontinuity is 4% in shear velocity, only slightly lower than *Revenaugh and Jordan's* average, and very similar to other regional and global models. The gradient below the 410-km discontinuity is in excellent agreement with ATL, although it is somewhat lower than PREM.

PA5 includes a 520-km discontinuity located at 507 ± 10 km, with an impedance contrast of 1.3% that is split into a 1.5% S-velocity increase and a 0.7% density increase. The presence of a global 520-km discontinuity has been advocated by *Shearer* [1990] and *Revenaugh and Jordan* [1991b], although its signature is still disputed in short-period profiles [*Cummins et al.*, 1992; *Jones et al.*, 1992], and *Shearer's* [1990] results have been recently challenged [*Bock*, 1994]. Our *S*, *SS*, and *SSS* data provide good constraints on the average velocity structure of the transition zone, but they offer little help in characterizing a 520-km discontinuity, because of the poor resolution available from their relatively long wavelengths. The presence of a 520 in the reflectivity profile (Figure 2.2) leads us to include it in our model. In addition, the density and bulk sound velocity profiles for pyrolite and piclogite both have a break in slope at this point [*Ita and Stixrude*, 1993] (due to the β-phase to γ-spinel transition), and an alternative mineralogical analysis

[*Rigden et al.*, 1991] argues that a significant density jump combines with a small velocity jump at this phase boundary to produce a shear impedance contrast of up to 5%. Given the uncertainties in the mineral physics observations and the limited bandwidth and/or geographic distribution in the seismological observations, we maintain a discontinuity that conservatively fits our *ScS*-reverberation observation with a discontinuity in both velocity and density.

The gradient between 507 km and the 660-km discontinuity is shallow relative to ATL and PA2 (Figure 2.16), primarily because of the relatively large 520-km and 660-km discontinuities. The average velocity in this depth range is about the same for the three models. PREM incorporates a very flat gradient just above the 660-km discontinuity that is similar to PA5. The 660-km discontinuity is relatively shallow (651 ± 4 km). The depths of the 410-km and 660-km (415 km and 651 km) relative to their global averages are consistent with a hot transition zone beneath the Pacific. The direct comparison with continental upper mantle is made in Chapter 6.

SUMMARY

We present a new seismic model for a corridor beneath the western Pacific. This model represents the first in a generation of radially anisotropic models that are constructed using a broad spectrum of seismic and other data. We measure and analyze 1497 frequency-dependent travel times from three-component recordings of *R1*, *G1*, *SSS*, *sSS*, *SS*, and *S* waveforms, which constrain the anisotropic shear velocity structure within the upper mantle. The use of the GSDF procedure allows for a very complete analysis of the observed seismograms across a broad frequency band (10-50 mHz), and it also allows us to accurately analyze very complex waveforms (for example, oceanic multi-mode Love waves) that are difficult to analyze using traditional techniques. These data are considered in conjunction with *ScS*-reverberation data, which provide well-constrained depths and impedance contrasts of discontinuities along this corridor. As a result, both anisotropy and

discontinuities can be considered in a regional context. Distributions of density and bulk sound velocity expected for mineralogical models of the upper mantle are used to further constrain the model in a realistic manner. We successfully invert these data for one-dimensional, path-average, radially anisotropic models for Pacific upper mantle between Tonga-Fiji and Hawaii, specifically testing hypotheses on the depth distribution of the anisotropic structure.

Model PA5 represents the significant result of this chapter -- a simply-parameterized seismic model that can be utilized and tested in further seismic analyses. While PA5 holds several implications for the anisotropic structure of oceanic upper mantle, we delay discussion of these issues pending further analysis of the western Pacific in Chapter 3. This chapter also focuses on the analysis and inversion procedures that lead to PA5. The successful compilation and inversion of three discrete data sets that were not guaranteed to be self-consistent is a significant result in itself, and it bodes well for incorporation of a variety of data types in future seismic analyses. We use an identical procedure in Chapters 3 and 4, and future work described in Chapter 6 will take this analysis to new levels.

We find that anisotropy must be present through the oceanic lithosphere and into the low-velocity zone to ~170 km depth. A small amount of anisotropy is allowed, but not preferred, below this depth. Other features of preferred model PA5 include a thin, high velocity seismic lithosphere bounded at ~70 km depth by a sharp G discontinuity, a well-defined low-velocity zone extending to ~170 km depth, no observable L (~200 km) discontinuity, and very high gradients in velocity between 170-415 km depth. The transition zone is consistent with mineralogical data for either pyrolite or high-aluminum piclogite.

Table 2.1. ScS Reverberation Data, Tonga-Fiji to Oahu

Discontinuity	Observed		PA5 Prediction		PA2 Prediction	
	t_v	R_O	t_v	R_O	t_v	R_O
Moho	1.7	0.120	2.1	0.164	2.3	0.184
G	12.0	-0.055	14.2	-0.036	21.8	-0.034
L	----	0.000	36.8	0.004	41.1	0.008
"410"	91.1	0.046	91.8	0.039	89.7	0.045
"520"	107.7	0.021	109.7	0.013	----	0.000
"660"	136.6	0.078	136.5	0.080	141.2	0.071
CMB	470.1	----	468.5	----	470.1	----

t_v represents one-way travel time in seconds; R_O is the shear wave impedance contrast. Observations extracted from *Revenaugh and Jordan* [1991a,c].

Table 2.2. Tonga/Fiji Seismic Sources

Date			Harvard CMT Location Origin Time UT	Latitude °N	Longitude °E	Depth km	Station	Delta °
1984	11	17	22:43:42.5	-18.28	-175.73	10	HON	43.01
1985	11	02	19:49:31.5	-18.21	175.99	10	HON	46.82
1988	04	02	14:26:39.8	-15.08	-172.96	15	HON	39.03
1989	04	08	03:06:08.7	-15.90	-172.91	15	HON	39.77
1991	01	01	17:28:08.4	-21.28	-173.98	15	KIP	45.21
1991	01	08	22:04:19.0	-17.76	-173.12	15	KIP	41.65
1991	02	09	02:08:57.0	-15.00	-176.81	15	KIP	40.62
1991	04	06	14:34:28.2	-14.86	-175.36	15	KIP	39.87
1991	04	19	11:25:37.3	-15.01	-174.90	15	KIP	39.81
1991	08	05	06:05:50.3	-21.58	-173.68	15	KIP	45.39
1983	09	17	12:11:43.1	-16.67	-177.24	16	HON	42.20
1987	01	09	08:01:40.2	-19.28	-176.52	17	HON	44.23
1983	05	15	00:24:01.4	-19.09	-175.72	20	HON	43.74
1990	09	08	20:32:06.5	-20.39	-173.96	21	KIP	44.38
1987	09	07	11:57:16.9	-28.06	-177.77	23	HON	55.55
1991	03	03	15:20:32.0	-22.09	-174.58	23	KIP	46.17
1988	12	05	16:05:44.7	-14.76	-173.49	44	HON	38.94
1985	06	03	12:06:29.7	-15.41	-173.28	46	HON	39.46
1991	10	30	10:35:51.9	-15.11	-173.07	48	KIP	39.19
1985	07	06	03:37:25.5	-29.50	-177.64	54	HON	53.95
1988	06	11	12:17:33.6	-15.06	-173.40	59	HON	39.18
1985	09	26	07:27:58.9	-34.79	-178.40	61	HON	59.07
1991	10	17	09:05:28.4	-14.83	-173.41	62	KIP	39.06
1987	11	03	08:15:09.5	-17.06	-173.55	107	HON	41.07
1988	01	29	16:48:11.7	-15.02	-173.71	119	HON	39.26
1988	02	06	21:30:11.0	-16.10	-173.49	124	HON	40.17
1989	01	02	01:52:14.5	-18.49	-174.39	128	HON	42.69
1984	04	18	06:49:21.9	-16.10	-174.02	158	HON	40.37
1988	07	19	01:00:24.9	-19.71	-174.39	159	HON	43.81
1991	11	11	16:15:55.2	-23.94	-176.97	179	KIP	48.71
1990	06	23	21:38:29.4	-21.29	-176.22	195	KIP	46.02
1986	10	30	01:29:05.1	-21.68	-176.45	196	HON	46.37
1987	03	19	22:51:45.9	-20.30	-175.96	215	HON	44.93
1988	01	15	08:40:30.5	-20.68	-175.77	221	HON	45.21
1986	06	28	05:03:55.4	-19.96	-175.71	222	HON	44.53
1984	06	15	14:22:32.8	-15.90	-174.66	270	HON	40.43
1991	06	09	07:45:10.9	-20.15	-175.90	292	KIP	44.86
1987	04	29	14:27:44.3	-19.06	-177.84	411	HON	44.58
1987	02	10	00:59:35.9	-19.47	-177.38	419	HON	44.75
1984	11	17	13:45:56.4	-18.84	-177.96	472	HON	44.43
1989	10	23	13:08:39.4	-25.51	179.15	480	HON	51.56
1990	06	08	15:05:19.2	-18.51	-178.93	504	KIP	44.66
1989	11	16	08:39:53.7	-17.36	-179.43	555	HON	43.80
1989	05	08	14:28:39.3	-23.62	-179.99	558	HON	49.53
1990	07	22	09:26:25.1	-23.15	-179.83	559	KIP	49.13
1983	06	20	05:43:41.8	-23.68	179.23	562	HON	49.92

Table 2.2. (continued)

Date	Harvard CMT Location				Station	Delta
	Origin Time UT	Latitude °N	Longitude °E	Depth km		°
1986 06 16	10:48:35.6	-21.86	-178.87	565	HON	47.50
1991 12 03	10:33:47.3	-26.11	178.69	575	KIP	52.37
1990 10 10	05:55:03.2	-23.08	178.93	575	KIP	49.61
1991 09 30	00:21:54.0	-20.67	-178.52	590	KIP	46.38
1990 07 11	19:48:17.0	-25.22	178.22	596	KIP	51.79
1989 04 16	19:48:22.9	-20.79	-179.18	601	HON	46.68
1986 05 26	18:40:54.5	-21.57	-179.30	603	HON	47.42
1990 06 26	12:08:38.5	-21.71	-179.60	614	KIP	47.76
1988 03 10	10:25:13.3	-21.02	-178.44	636	HON	46.57
1985 08 28	20:50:55.5	-20.89	-179.00	640	HON	46.70
1984 11 22	17:07:44.8	-17.72	-178.05	663	HON	43.48

Table 2.3. Model PA5

Depth, km	Density, gm/cm^3	v_{SV}, km/s	v_{SH}, km/s	v_{PV}, km/s	v_{PH}, km/s	η
0	1.03	0.00	0.00	1.50	1.50	1.00
5.0	1.03	0.00	0.00	1.50	1.50	1.00
5.0	1.50	0.92	0.92	2.01	2.01	1.00
5.2	1.50	0.92	0.92	2.01	2.01	1.00
5.2	3.03	3.68	3.68	5.93	5.93	1.00
12.	3.03	3.68	3.68	5.93	5.93	1.00
12.	3.34	4.65	4.84	8.04	8.27	0.90
68.	3.38	4.67	4.83	8.06	8.30	0.90
68.	3.35	4.37	4.56	7.88	8.05	0.90
166.	3.41	4.26	4.34	8.04	8.09	1.00
166.	3.42	4.29	4.29	8.06	8.06	1.00
415.	3.58	4.84	4.84	8.92	8.93	1.00
415.	3.71	5.04	5.04	9.29	9.29	1.00
507.	3.85	5.20	5.20	9.64	9.64	1.00
507.	3.88	5.28	5.28	9.71	9.71	1.00
651.	4.02	5.43	5.43	10.11	10.11	1.00
651.	4.29	5.97	5.97	10.76	10.76	1.00
791.	4.46	6.23	6.23	11.08	11.08	1.00
791.	4.46	6.23	6.23	11.08	11.08	1.00
801.	4.46	6.24	6.24	11.10	11.10	1.00

Model is identical to PREM through the remainder of the lower mantle and core.

FIGURE CAPTIONS

Fig. 2.1. Mercator projection of the Tonga/Fiji-to-Hawaii corridor sampled by our data. The propagation path (dotted line) is highly oblique to the fossil spreading direction (as depicted by plate age contoured in 25 Ma intervals) [*Mueller et al.*, 1993]) and is roughly perpendicular to current plate motion relative to a hotspot reference frame (arrow) [*Gripp and Gordan*, 1990]. Epicenters of the 55 Tonga-Fiji earthquakes are shown.

Fig. 2.2. (Left) Observed reflectivity profile and its interpretation obtained for central Pacific corridor, connecting events in the Tonga/Fiji seismic zone with station KIP. The profile and its interpretation both display vertical-incidence shear reflectivity (R_o), in percent. Apparent depths in interpretation were computed using the aspherical M84C velocity structure of *Woodhouse and Dziewonski* [1984]; these depths are refined in the model presented in this paper. (Right) Seismic Q structure for the Tonga/Fiji to Oahu path. (a) Average Q_{ScS} from multiple-*ScS* observations. (b) Q_{UM} and Q_{LM} from *ScS*-reverberation observations. (c) A priori Q structure assumed for the modeling in this paper. Q_{UM} is partition into lid, LVZ, and transition zone values. The vertical average Q is maintained within each column, i.e. (c) maintains the average upper- and lower-mantle values in (b), and (b) maintains the average value in (a).

Fig. 2.3. Direct observational evidence of anisotropy in long-period seismograms. (a) Data from a shallow-focus (10 km depth) event. Top pair of traces are vertical-component data and full synthetic seismogram for isotropic model PA2, with an *S* wave arriving at ~14.5 min and a Rayleigh wave at ~20 min. The bottom pair of traces are tangential-component observation and synthetic seismogram for PA2, with the *S* wave again at ~14.5 min and multimode Love wave at ~18 min. Although the group arrival of the Rayleigh

wave roughly matches the PA2 synthetic, the dispersion is quite different, and the fit to the Love wave is extremely poor. (b) Data from a deep-focus (562 km) event. Top pair of traces are vertical-component data and full synthetic for PA2 centered on an *SSS* arrival at ~21 min. The bottom pair of traces are the tangential-component data and synthetic for this arrival. The synthetics have been shifted so that the vertical-component *SSS* synthetic is aligned with the data. The LPT *SSS* arrival is faster than PA2 (and the vertical-component *SSS* observation) by nearly half a cycle, over 10 s. *SH-SV* differences in phases such as this one place good constraints on anisotropy in the deeper upper mantle and the transition zone. Mode-summation synthetic seismograms are complete to 50 mHz, filtered like the data, and convolved with Harvard CMT source mechanisms.

Fig. 2.4. Example of the GSDF processing, as discussed in the text. a) Observed (top), full synthetic (middle), and isolation filter (bottom) seismograms for vertical-component data from a deep focus event (472 km depth). Observed phases are *S* (13.5 min), *sS* (16 min), *SS* (17 min), and *sSS* (19 min). The isolation filter is for *sSS*, constructed by summing mantle modes with group velocities of 4.20 ± 0.1 km/s. b) Phase delays $\delta\tau_p$ as a function of frequency, relative to the starting model. The frequency-dependent trend indicates the relative dispersion observed in these "body" waves, and illustrates the value of using a broad-band approach to processing the data. This data is fast at high frequencies, but is well fit by the model at low frequencies. c) Three sets of partial derivative kernels as a function of depth; the kernels relative to the two shear velocities for 15, 30, and 45 mHz are shown for this example. Solid line is the v_{SV} kernel, and dashed is for v_{SH}. While the low-frequency observation (15 mHz) is sensitive to v_{SV} in the upper 400 km, the higher-frequency observations become increasingly sensitive to structure in the transition zone.

Fig. 2.5. Example of the ability of GSDF to account for interference of complex waveforms. a) Observed (top), full synthetic (middle), and isolation filter (bottom)

synthetics for tangential-component data from a shallow-focus (10 km depth) event. The *S* wave arrives at ~14.5 min, the multimode Love wave at ~18 min. The isolation filter (Filt1) is constructed by summing only the fundamental mode branch, and thus it does not include higher mode contributions and is a poor match to even the full synthetic Love wave. b) Initial phase delay estimates $\delta\tau_p+\tilde{t}_p$, and final phase delays $\delta\tau_p$, as a function of frequency. The $\delta\tau_p$ have been corrected by up to 6 s by removing the interference term $\tilde{t}_p$. c) Partial derivative kernels for v_{SH} (solid line) that are used to invert the $\delta\tau_p$ observations in 2.5c. The dash line represents the kernels that would be used if the Love wave were assumed to be fundamental mode only (i.e. the interference corrections were not applied).

Fig. 2.6. a) Same data and full synthetic as Figure 2.5a, but with a new isolation filter (Filt2) constructed by summing all mantle modes with group velocities 4.34 ± 0.2 km/s. This Filter represents an excellent match to the full synthetic Love wave, and interference corrections are negligible. b) Final phase delays $\delta\tau_p$ for both Filt2 and Filt1 from Fig. 2.5b. c) v_{SH} partial derivative kernels for Filt2 and Filt1. The nearly identical behavior for the phase delays and kernels for these two filters demonstrates the robustness of the GSDF procedure.

Fig. 2.7. Partial derivative kernels for examples of different phase types. a) Rayleigh wave kernels. b) Tangential-component *SS* kernels. c) Vertical-component *S* kernels. For each phase, two frames are shown: low frequency (15 mHz) on the left, high frequency (40 mHz) on the right. Within each frame, 3 pairs of kernels are shown: shear kernels on the left, compressional kernels in the middle, and η and density kernels on the right. *P* and η kernels for tangential-component observations are identically zero. Relative scales are maintained for each phase, with a scale on the far right in units of s km^{-3} $unit^{-1}$ perturbation. η is also scaled by a factor of 4000 to facilitate plotting with density.

Fig. 2.8. Partial derivative kernels for the same *sSS* phase on vertical (a) and tangential (b) component seismograms. Plotting is the same format as Figure 2.7. Note the different depth extent of the sampling depth for the two phases, with sSS_H sampling deeper than sSS_V, especially at high frequency. Also, note that while sSS_V has no sensitivity to v_{SH}, sSS_H has significant sensitivity to v_{SV} at shallow depths.

Fig. 2.9. Summary of the frequency-dependent travel time data. Phase delays are categorized by phase type (Surface wave, *SSS* , *SS*, or *S*), and then separated into tangential (*SH*) or radial/vertical (*SV*) observations, and averaged in each frequency band. Symbols represent the residuals relative to PA2, while the lines represent the predicted fit of model PA5 to these data. Dispersion relative to PA2 is indicated by a frequency-dependent trend, while evidence of anisotropy can be observed as a separation of the *SH* and *SV* observations for a given phase type. a) Love and Rayleigh waves. b) *SSS* and *sSS* waves. c) *SS* waves. d) *S* waves. Error bars are determined by a weighted average of estimated *a priori* errors.

Figure 2.10. Values of density ρ and bulk sound velocity v_ϕ calculated by *Ita and Stixrude* [1992] for the pyrolite model (*circles*); error bars represent arbitrary ±1% errors for the calculated profiles. These were used to construct prior distributions for ρ and v_ϕ that were used in the inversion. The values calculated from resulting model PA5 (*solid lines)* are shown for comparison. Neither the density nor the bulk sound velocity constraints are critically dependent on the choice of pyrolite for a model composition; the general behavior of both density and bulk sound velocity is similar for high-aluminum piclogite, for example.

Fig. 2.11. Model PA5. From left to right, η, density, shear velocities, and compressional velocities are plotted as a function of depth. The model is radially anisotropic through the

lithosphere and the low-velocity zone, with v_{SH} and v_{PH} being higher than v_{SV} and v_{PV}, respectively. Below 800 km depth, the model is the same as PREM.

Fig. 2.12a. Comparisons between observed and synthetic seismograms from 4 representative shallow- and intermediate-focus events. Each event is represented by both tangential- (LPT) and vertical- (LPZ) component seismograms; for each event pair, the top trace is the data, the bottom trace is the synthetic (complete to 50 mHz) for final model PA5. The traces are aligned (at 0 min) on the *S* wave, with the synthetic seismograms further corrected for an event static. Both data and synthetic are low-passed with a 45 mHz corner.

Fig. 2.12b. Same as Figure 2.11a, except for 4 representative deep-focus events.

Fig. 2.13. Seismograms showing a multi-mode Love wave that is diagnostic of high v_{SH} in the LVZ. The observed seismogram (center trace, labeled *KIP*) is the transverse component recorded at KIP from a shallow-focus event. The direct *S* wave arrives at ~13.5 min and the emergent Love-wave group at ~16 min. The trace labeled PA3 is a complete synthetic seismogram for an earth model where anisotropy is restricted to the lithosphere. Synthetics of the first four mode branches for this model are displayed above the full synthetic (*topmost traces*, with the 0th mode branch being the thickest line, and the 3rd higher-mode branch being the thinnest). The trace labeled PA5 is a complete synthetic for PA5, where the anisotropy extends into the LVZ. The increased SH velocity in the LVZ enhances and advances the 0th and 1st mode branches (shown in *lowermost traces*), thereby generating a complete synthetic with emergent, dispersed behavior similar to that observed in the data.

Fig. 2.14. Shear velocities for model PA5, a path-average approximation of S12_WM13 appropriate for the Tonga-Hawaii path (labeled "S12TH"), and PREM. For each model, the higher lid/LVZ velocity is v_{SH}, the lower velocity is v_{SV}. S12TH is calculated by determining the average S12_WM13 perturbation to PREM as a function of depth over the path from Tonga/Fiji to Hawaii. Comparison between PA5 and S12TH indicates that S12 is too slow in the lithosphere and too fast near 220 km along this path, similar to (though less severe than) the discrepancy between PA5 and PREM.

Fig. 2.15. Observed and synthetic seismograms for models PA5 and S12_WM13, for a shallow-focus event. The *S* wave arrives at 14.5 min, the G_1 at ~18 min, and R_1 at ~20 min. Vertical component seismograms are on top, and tangential component seismograms are on the bottom. Synthetics are aligned on the *S* wave to remove the source static, and the S12_WM13 seismograms are calculated using the spherical harmonic coefficients and the asymptotic perturbation scheme of *Woodhouse and Dziewonski* [1984]. a) Seismograms low-pass filtered with a corner at 15 mHz; PA5 and S12_WM13 both fit the data. b) Seismograms low-pass filtered with a corner at 35 mHz; PA5 fits the data much better than S12_WM13.

Fig. 2.16. Comparison of PA5 to other oceanic upper mantle shear velocity models. PA2 [*Lerner-Lam and Jordan*, 1987] is a Pacific model designed to fit Rayleigh waves, and it compares to the *SV* (lower) PA5 velocity quite well; the inclusion of *ScS* reverberations and higher frequencies in our analysis allows for better resolution of the lid velocity/thickness tradeoff. ATL [*Grand and Helmberger*, 1984b] is an *SH* model for the Atlantic, and thus compares to v_{SH} in PA5. While the differences in lid thickness and LVZ velocity may be true regional variations, this depth interval is the most poorly constrained aspect of ATL, and our model has better constraints on this part of the model due to our use of the dispersive information in the Love waves. TNA [*Grand and Helmberger*, 1984a] is

an *SH* model for the East Pacific Rise, and is thus much slower than other v_{SH} models in the uppermost mantle. The model we label NF4 [*Nishimura and Forsyth*, 1989] is the 52-110 Ma portion from a regionalized anisotropic model of the Pacific. PA5's high lid velocities and general depth extent of anisotropy agree quite well with this model, despite substantial differences in parameterization. The depth region of the termination of anisotropy (170-300 km) is probably better constrained in PA5 due to the inclusion of *SS* and *SSS* phases. Note the remarkable agreement between PA5, ATL, TNA, and PA2 on the gradient between 200-410 km. This steep gradient is not present in PREM, S12_WM13, or our Australian model, and it appears to be an extremely robust feature of oceanic upper mantle.

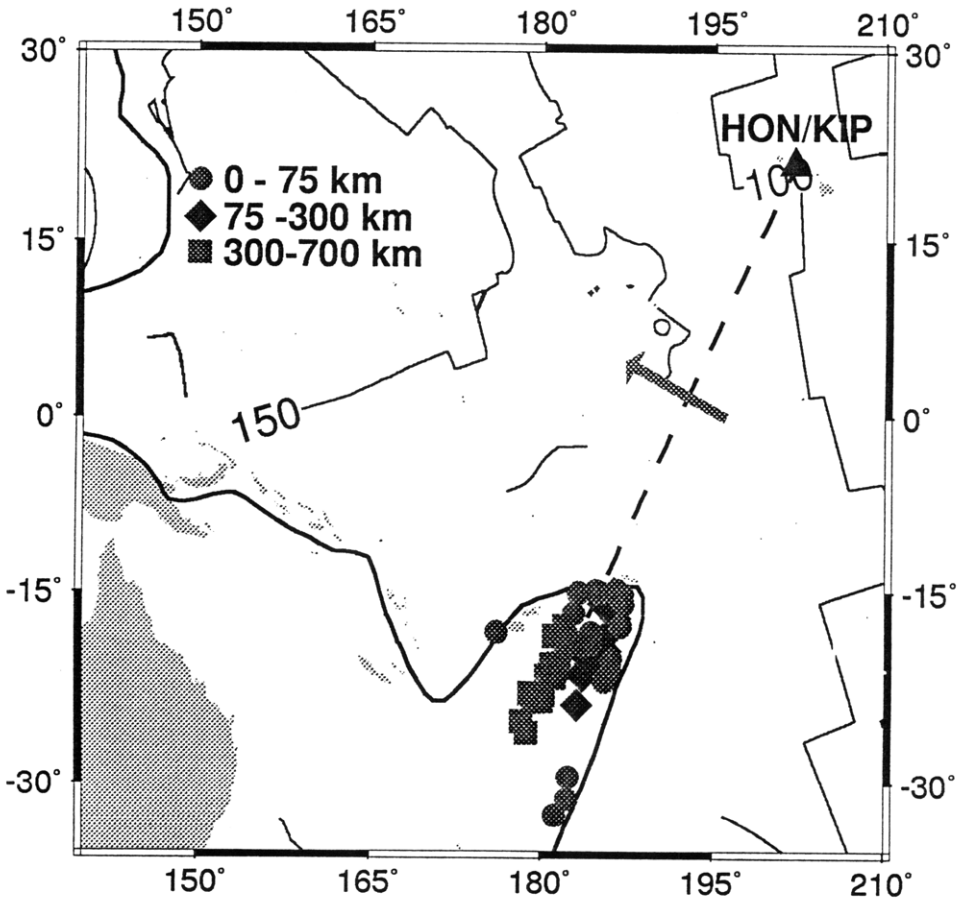
150°
165°
180°
195°
210°
30°
15°
0°
-15°
-30°
HON/KIP
0 - 75 km
75 -300 km
300-700 km
100
150

Figure 2.1

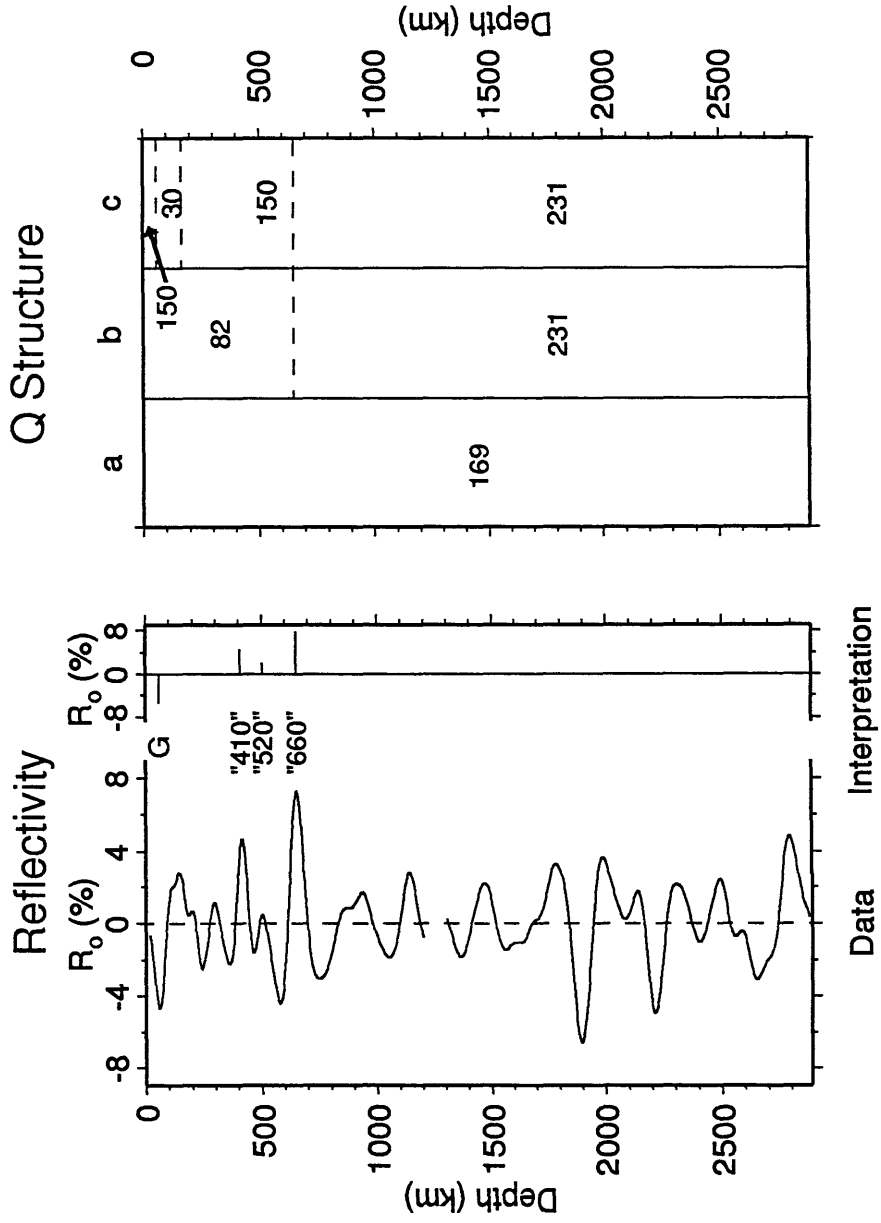
Q Structure
Depth (km)
0
500
1000
1500
2000
2500
a
b
c
169
82
150
30
150
231
231
Reflectivity
R_o (%)
-8
-4
0
4
8
G
"410"
"520"
"660"
Data
Interpretation

Figure 2.2

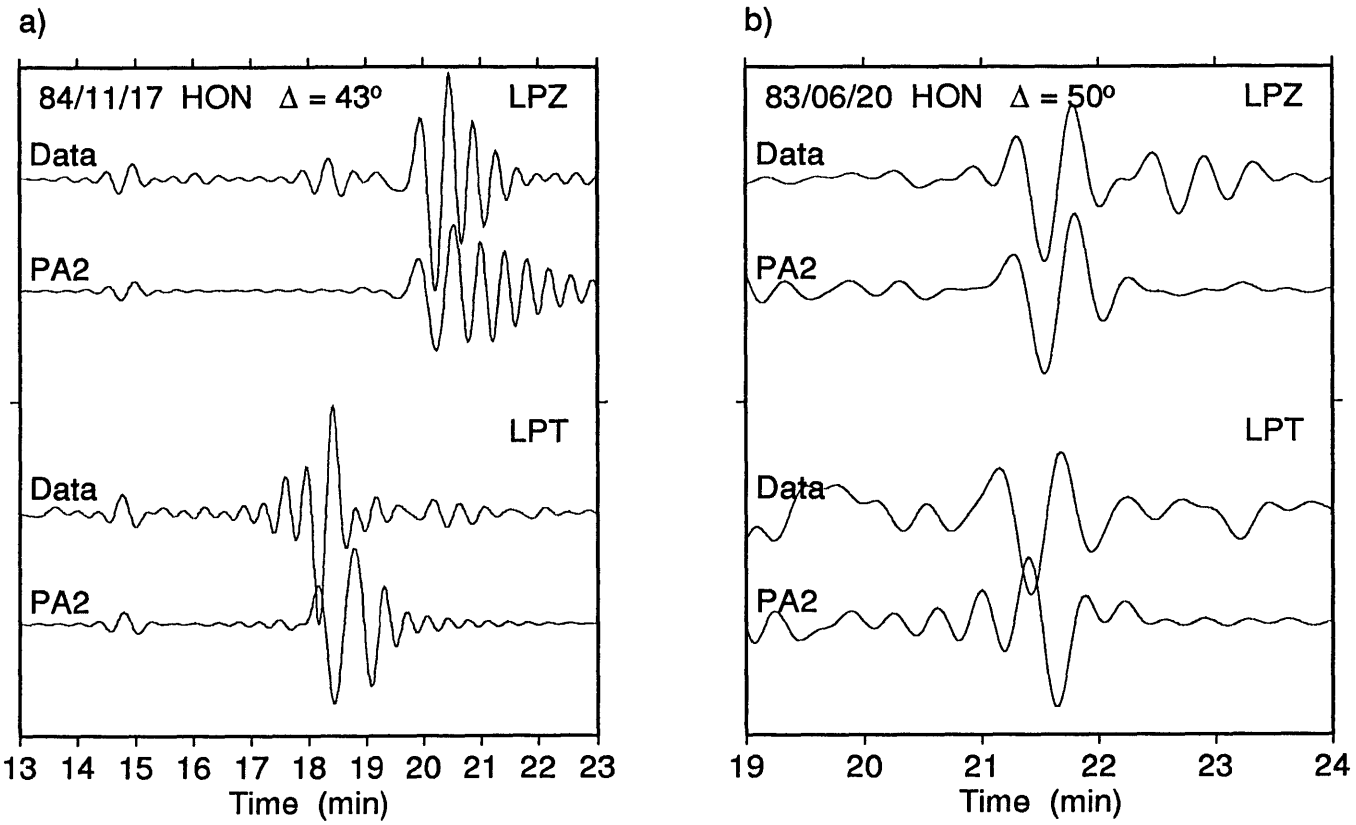
a)
84/11/17 HON Δ = 43°
LPZ
Data
PA2
LPT
Data
PA2
13 14 15 16 17 18 19 20 21 22 23
Time (min)
b)
83/06/20 HON Δ = 50°
LPZ
Data
PA2
LPT
Data
PA2
19 20 21 22 23 24
Time (min)

Figure 2.3

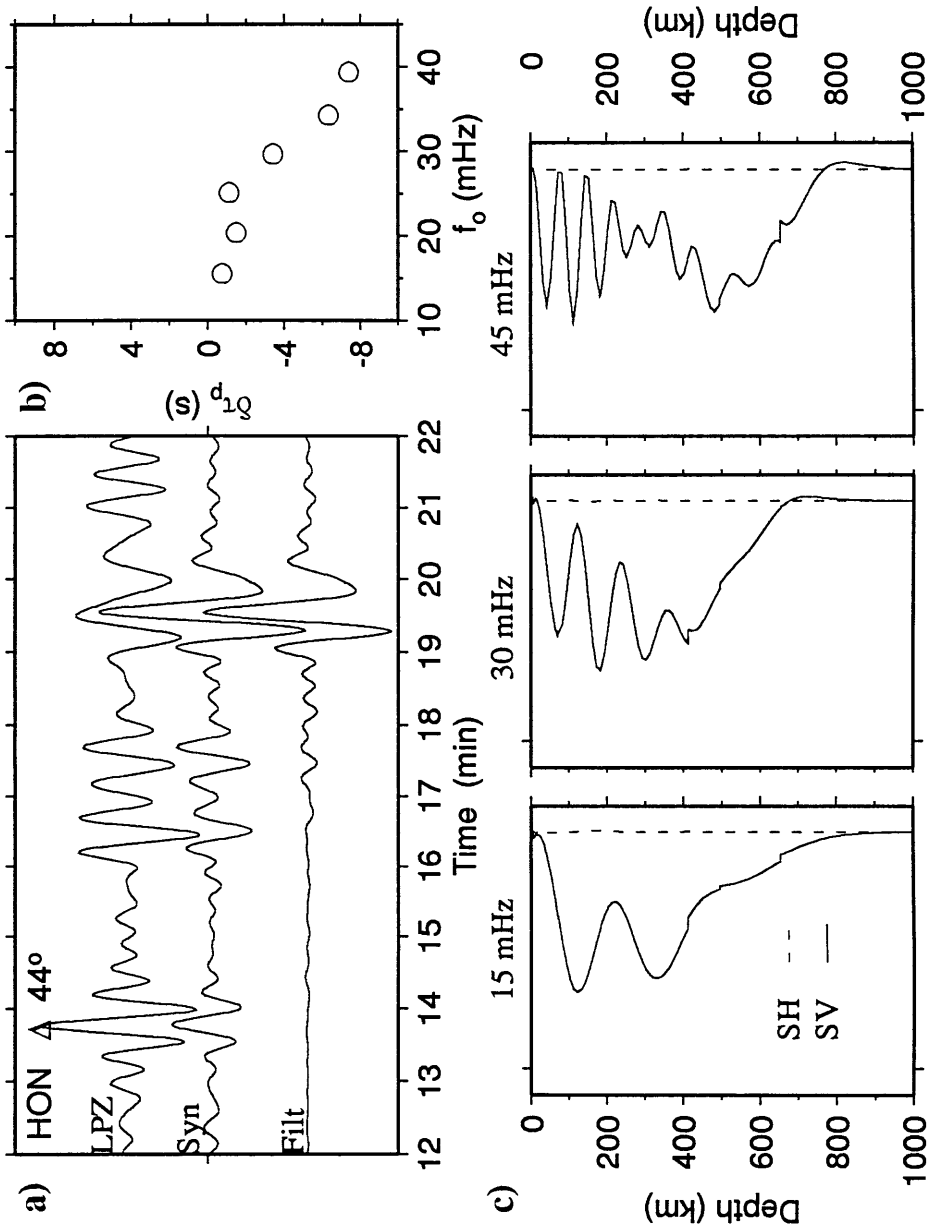
a)
HON
Δ 44°
LPZ
Syn
Filt
Time (min)
b)
δτp (s)
fo (mHz)
c)
15 mHz
30 mHz
45 mHz
SH
SV
Depth (km)

Figure 2.4

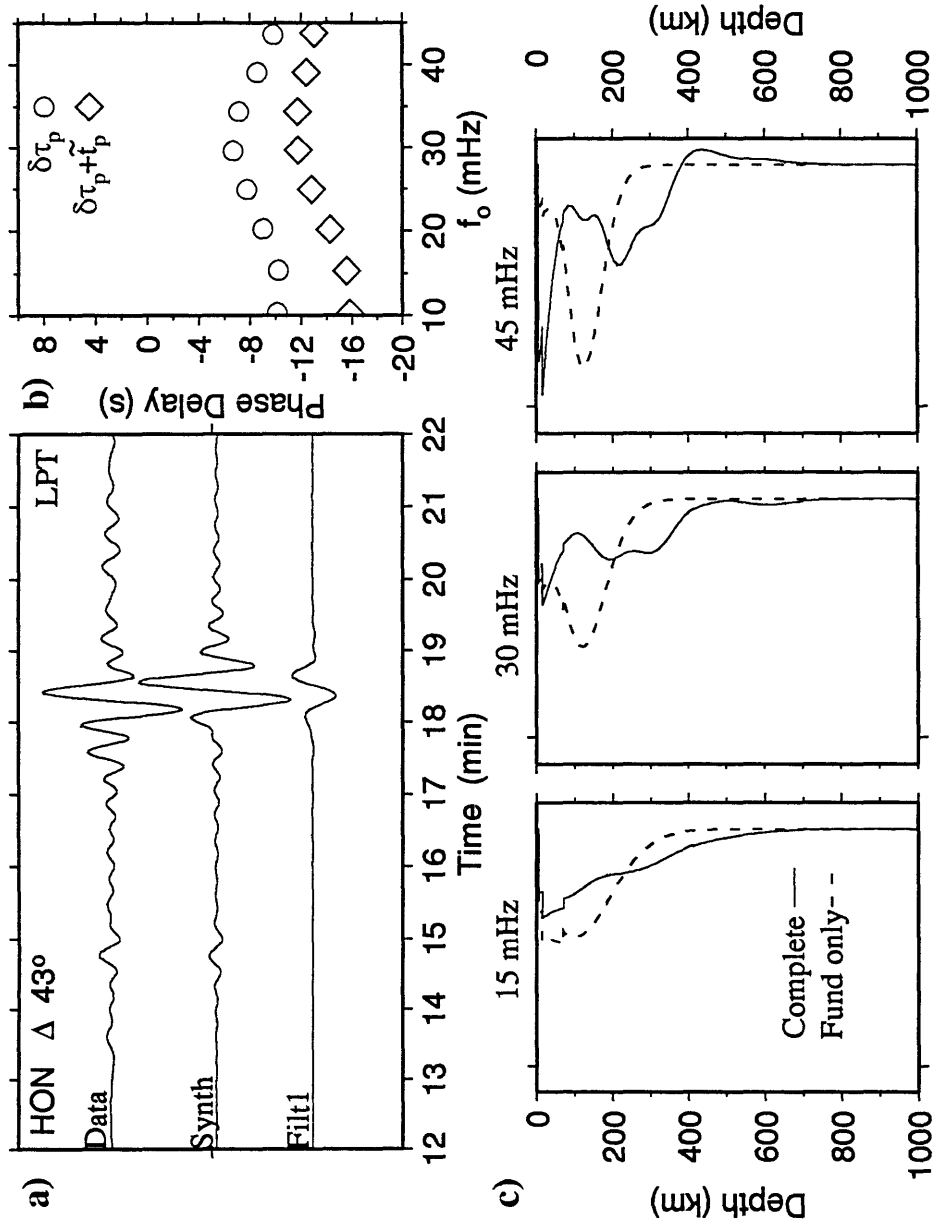
a)
HON Δ 43°
LPT
Data
Synth
Filt1
Time (min)
b)
Phase Delay (s)
$\delta\tau_p$
$\delta\tau_p+\tilde{t}_p$
f_o (mHz)
c)
15 mHz
30 mHz
45 mHz
Complete
Fund only
Depth (km)

Figure 2.5

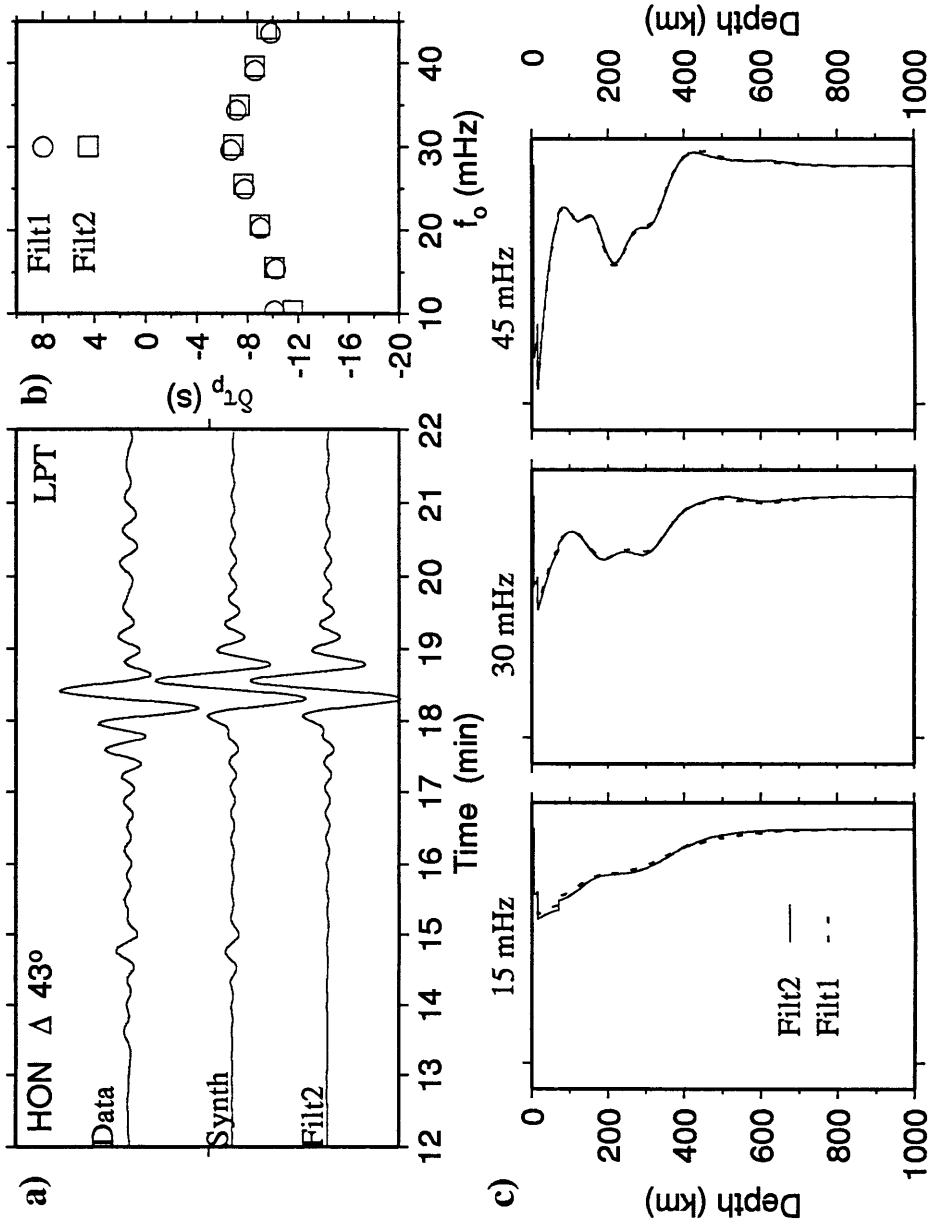
a)
HON Δ 43°
LPT
Data
Synth
Filt2
Time (min)
b)
Filt1
Filt2
δτp (s)
fo (mHz)
c)
15 mHz
30 mHz
45 mHz
Filt2
Filt1
Depth (km)

Figure 2.6

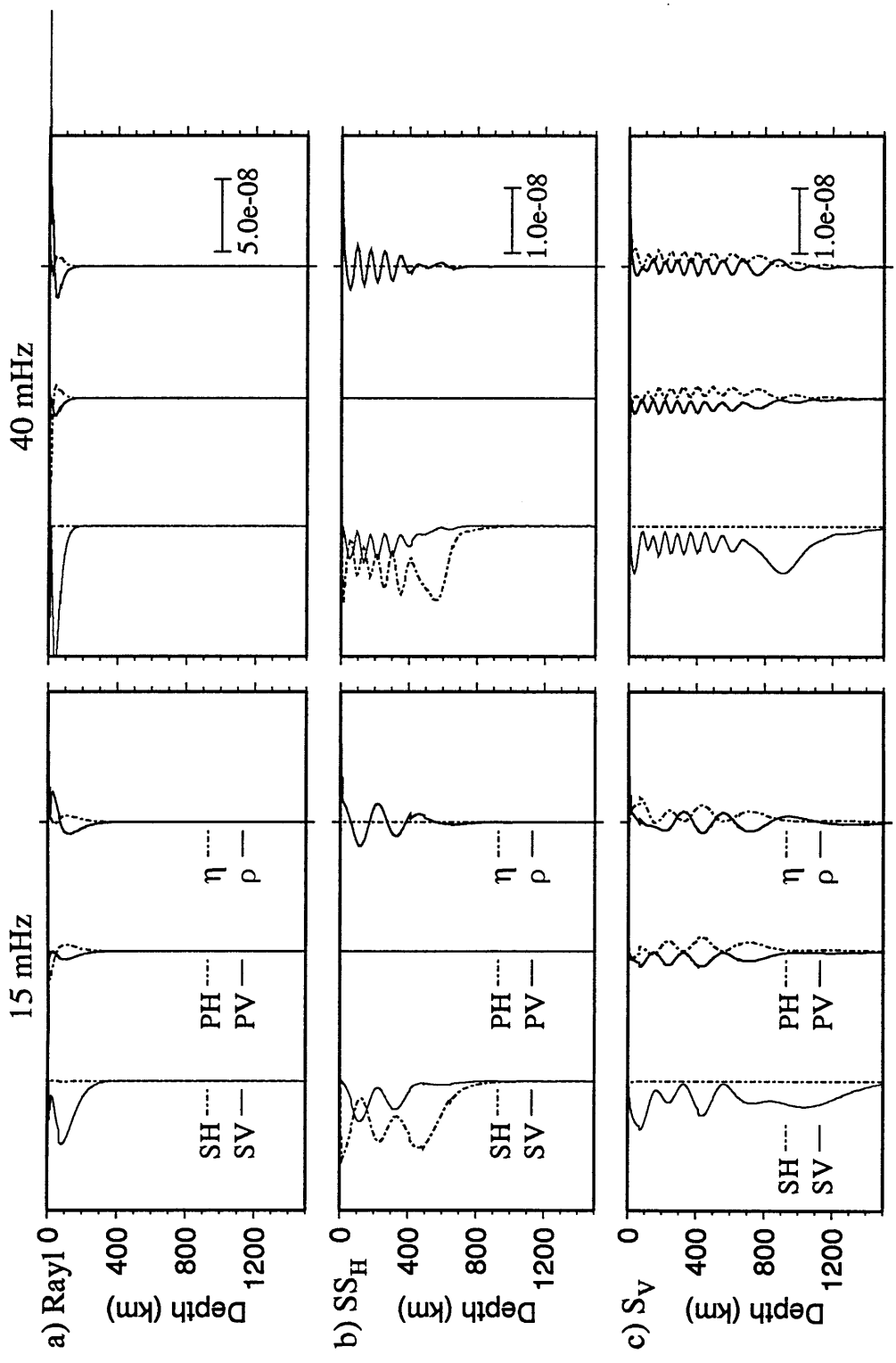
15 mHz
40 mHz
a) Ray1
b) SS_H
c) S_V
Depth (km)
0
400
800
1200
SH
SV
PH
PV
η
ρ
5.0e-08
1.0e-08
1.0e-08

Figure 2.7

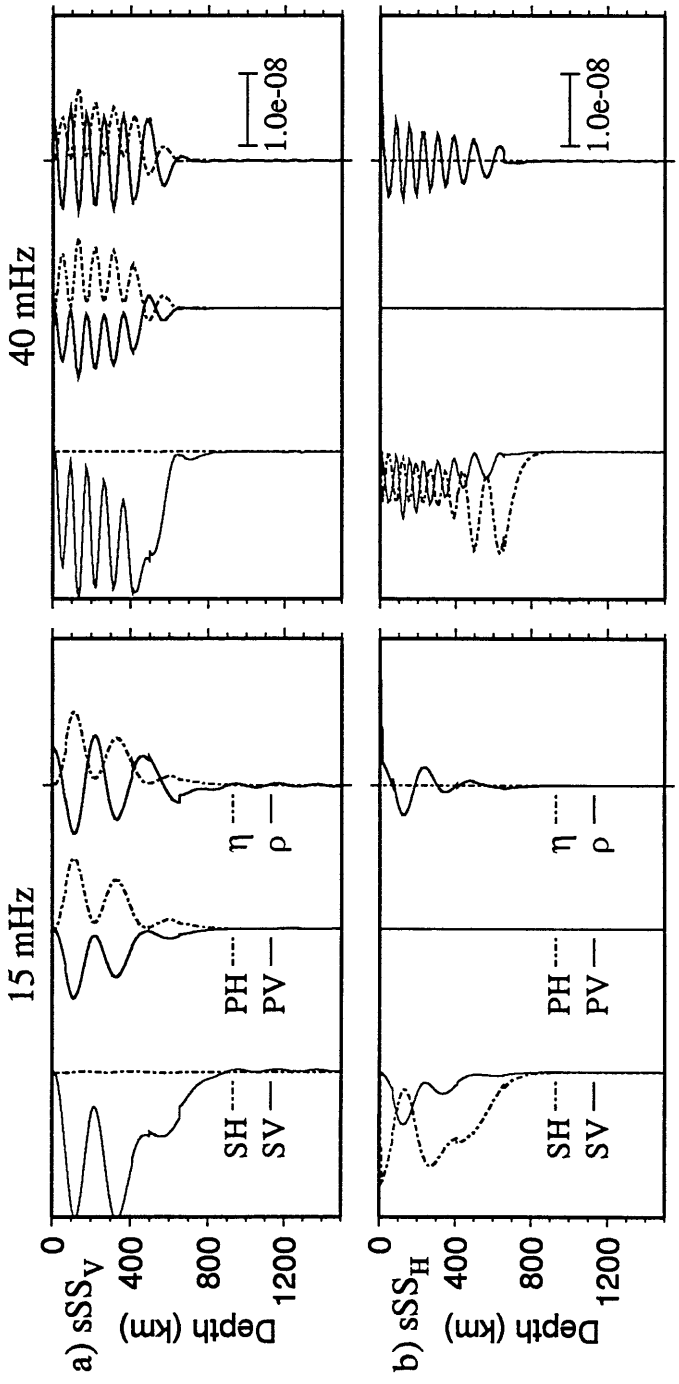
40 mHz
15 mHz
1.0e-08
1.0e-08
η
ρ
PH
PV
SH
SV
η
ρ
PH
PV
SH
SV
0
400
800
1200
Depth (km)
a) sSS$_V$
0
400
800
1200
Depth (km)
b) sSS$_H$

Figure 2.8

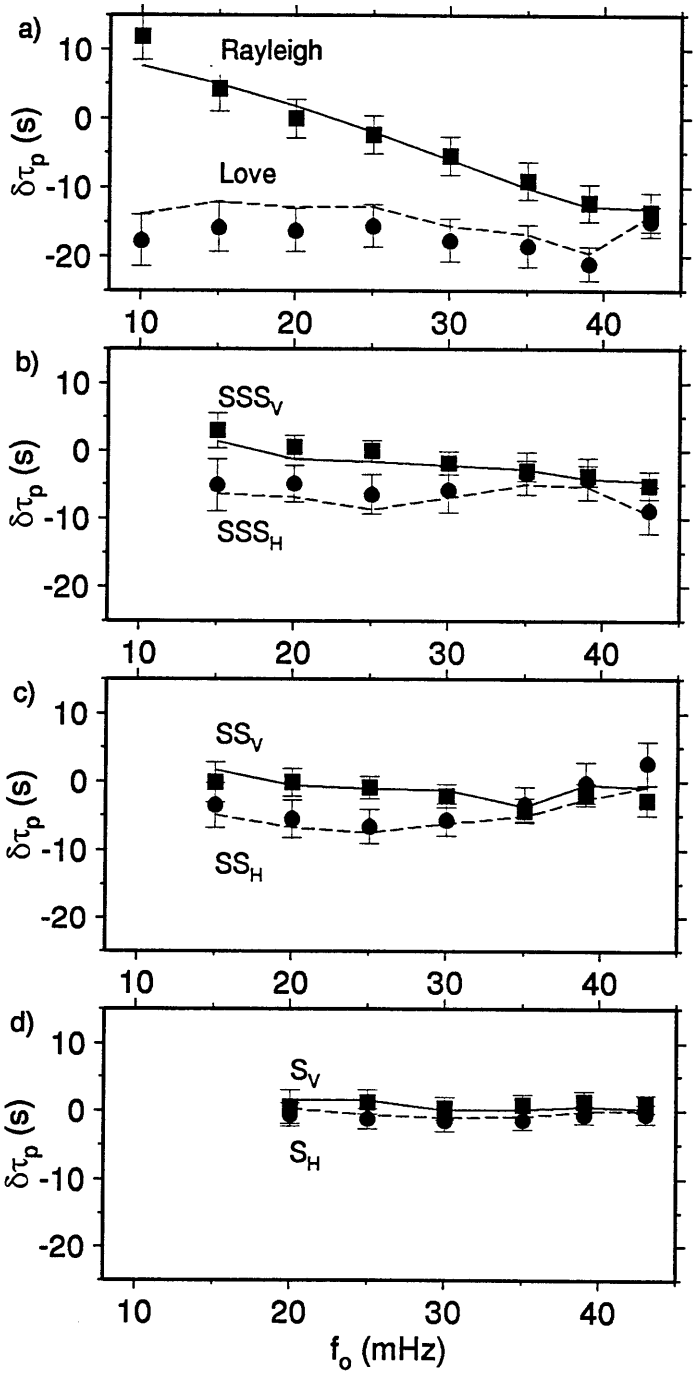
a)
Rayleigh
Love
b)
SSS$_V$
SSS$_H$
c)
SS$_V$
SS$_H$
d)
S$_V$
S$_H$
$\delta\tau_p$ (s)
10
0
-10
-20
10
20
30
40
f_o (mHz)

Figure 2.9

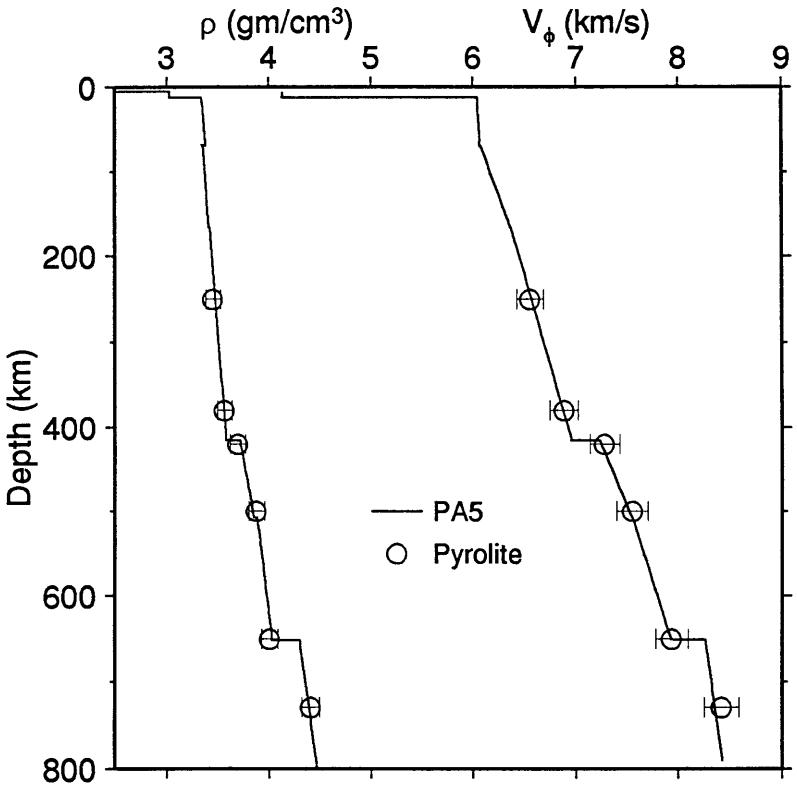

Figure 2.10

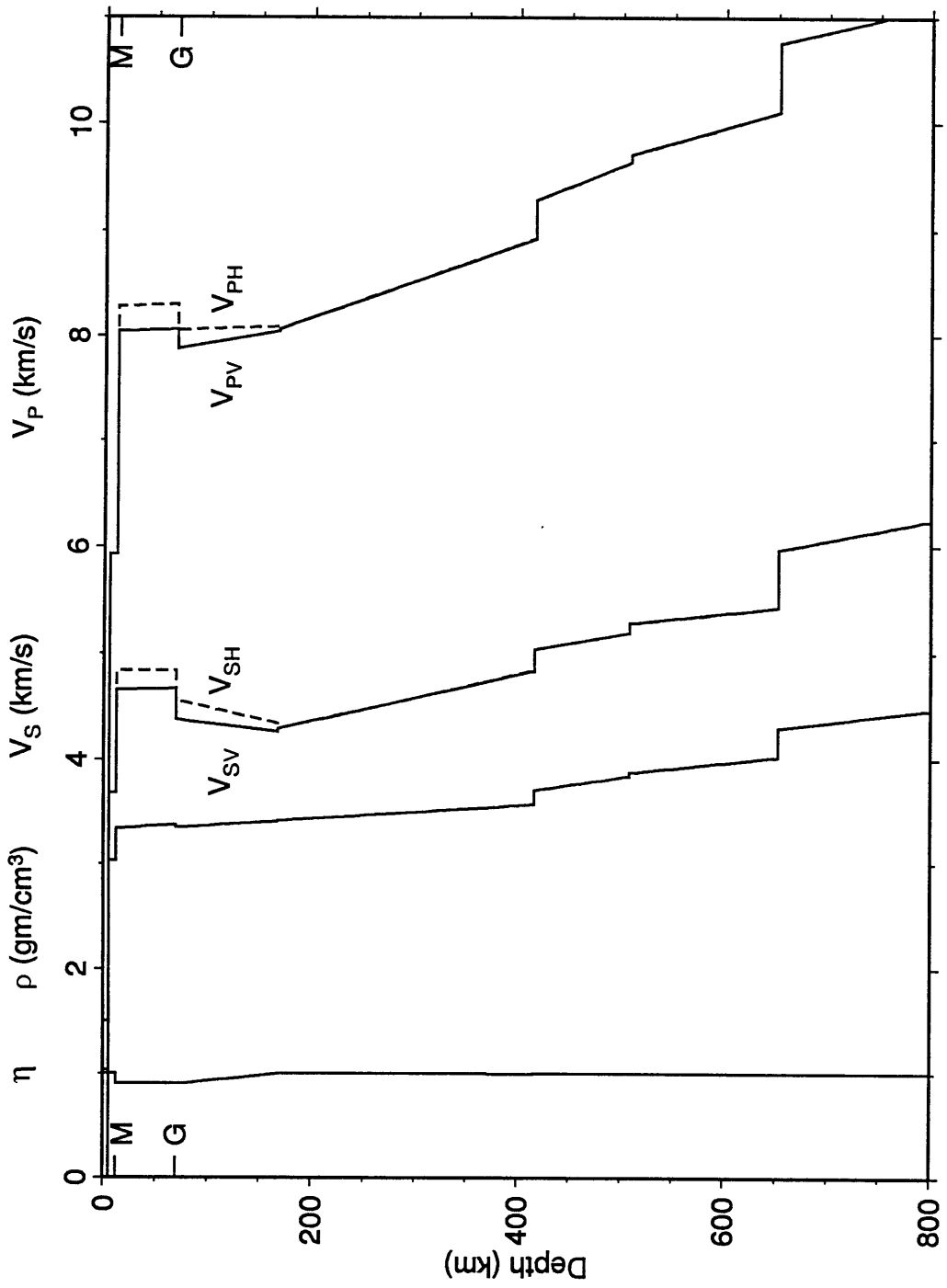
M
G
V_{PH}
V_{PV}
V_{SH}
V_{SV}
η
ρ (gm/cm³)
V_S (km/s)
V_P (km/s)
Depth (km)
0
2
4
6
8
10
0
200
400
600
800

Figure 2.11

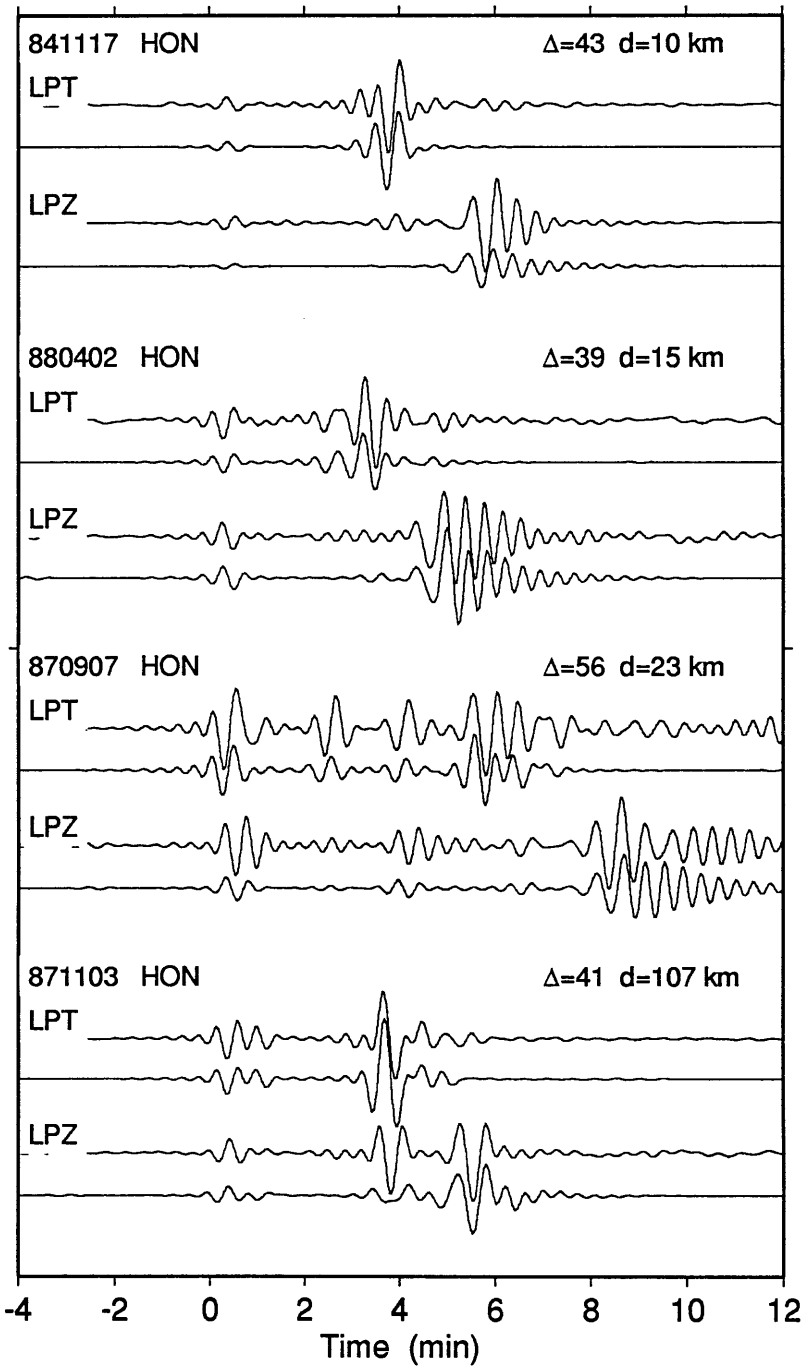
841117 HON
Δ=43 d=10 km
LPT
LPZ
880402 HON
Δ=39 d=15 km
LPT
LPZ
870907 HON
Δ=56 d=23 km
LPT
LPZ
871103 HON
Δ=41 d=107 km
LPT
LPZ
-4
-2
0
2
4
6
8
10
12
Time (min)

Figure 2.12a

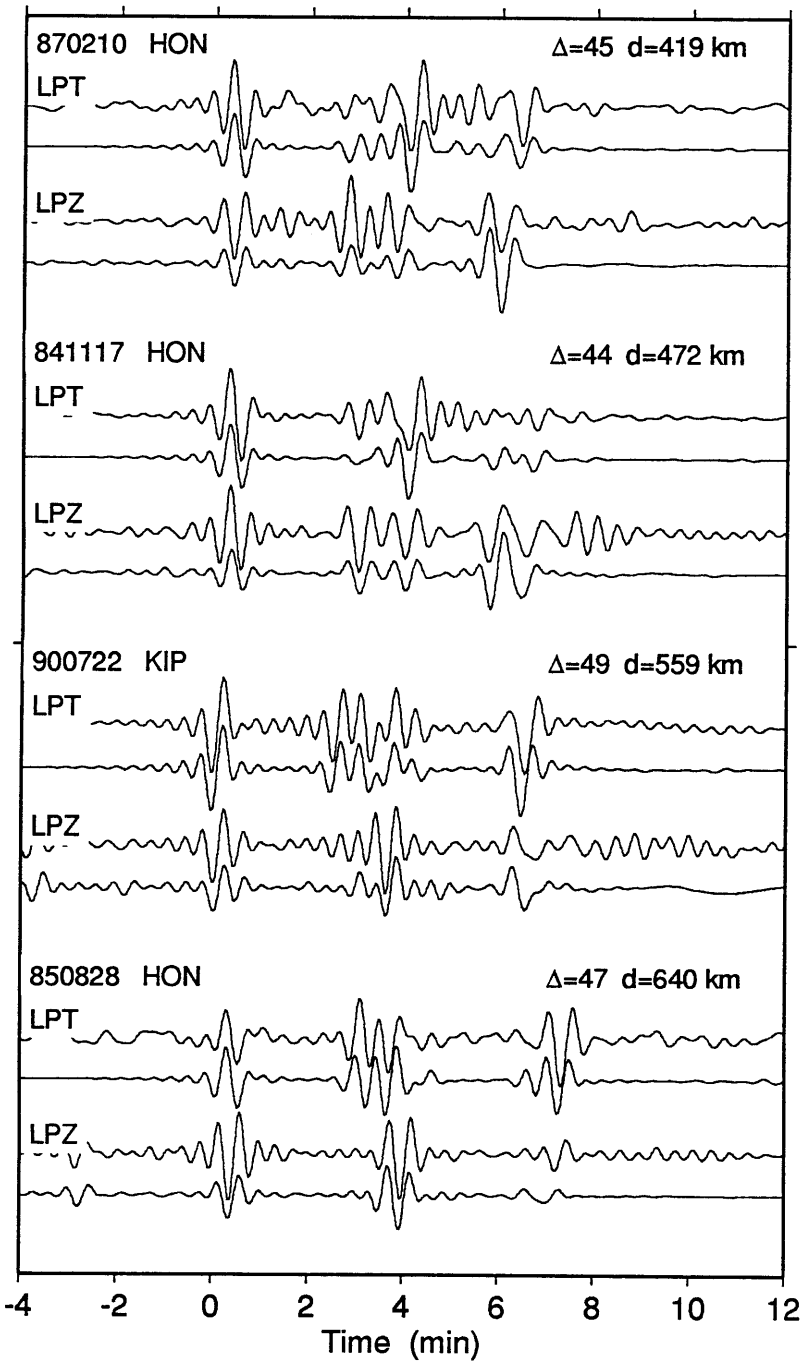
870210 HON
Δ=45 d=419 km
LPT
LPZ
841117 HON
Δ=44 d=472 km
LPT
LPZ
900722 KIP
Δ=49 d=559 km
LPT
LPZ
850828 HON
Δ=47 d=640 km
LPT
LPZ
-4
-2
0
2
4
6
8
10
12
Time (min)

Figure 2.12b

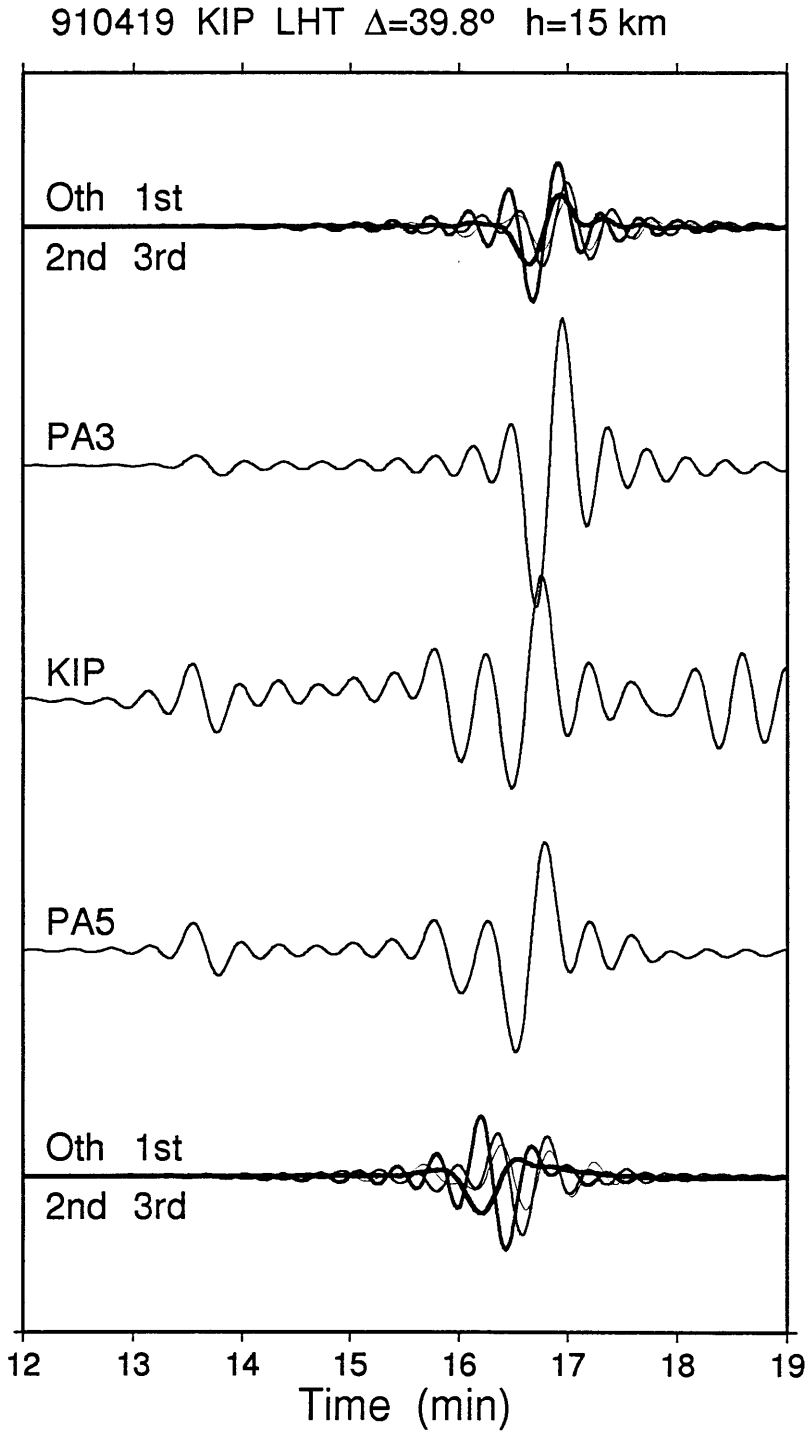
910419 KIP LHT Δ=39.8° h=15 km
Oth 1st
2nd 3rd
PA3
KIP
PA5
Oth 1st
2nd 3rd
12
13
14
15
16
17
18
19
Time (min)

Figure 2.13

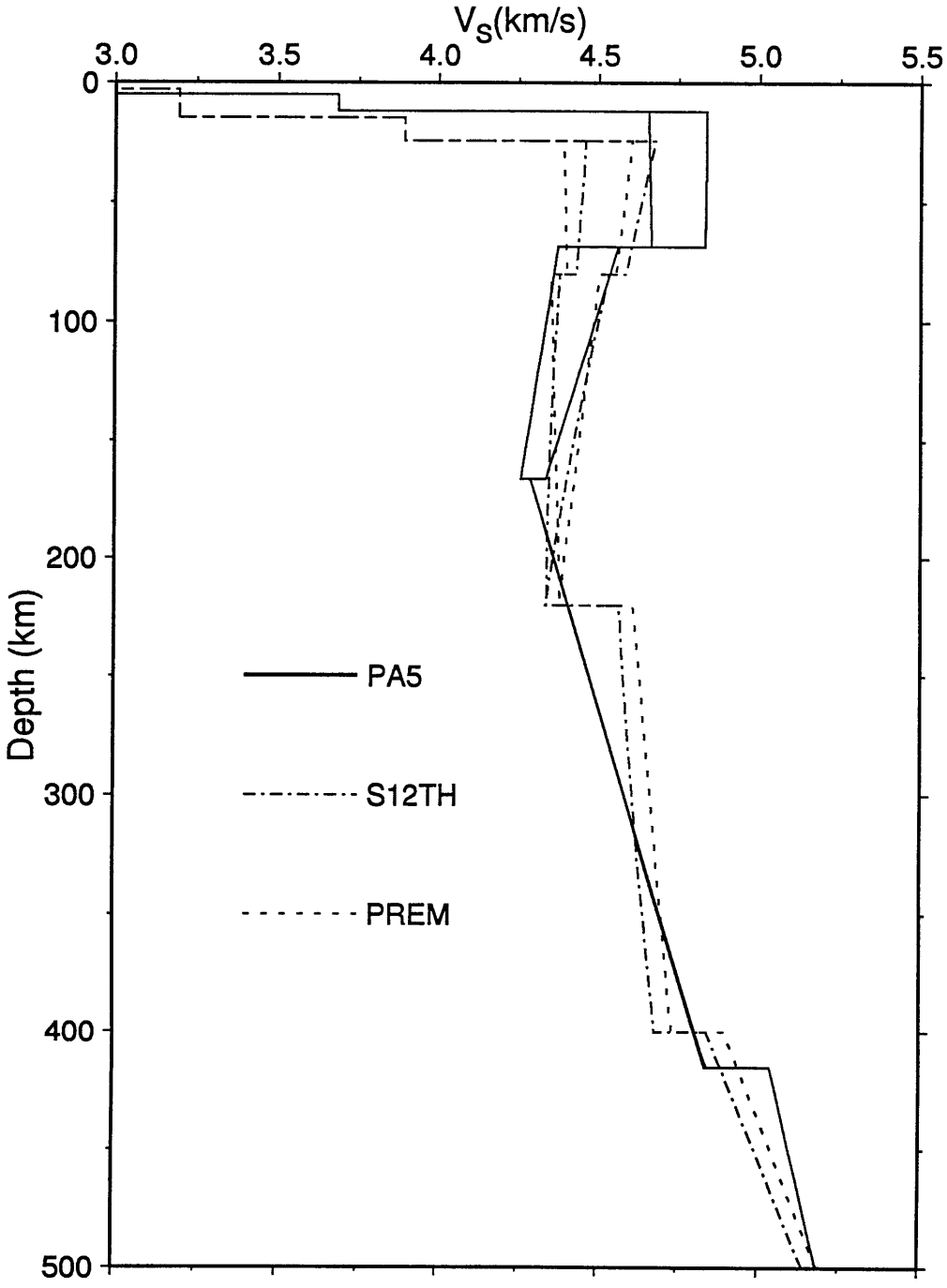
V_S(km/s)
3.0
3.5
4.0
4.5
5.0
5.5
0
100
200
300
400
500
Depth (km)
PA5
S12TH
PREM

Figure 2.14

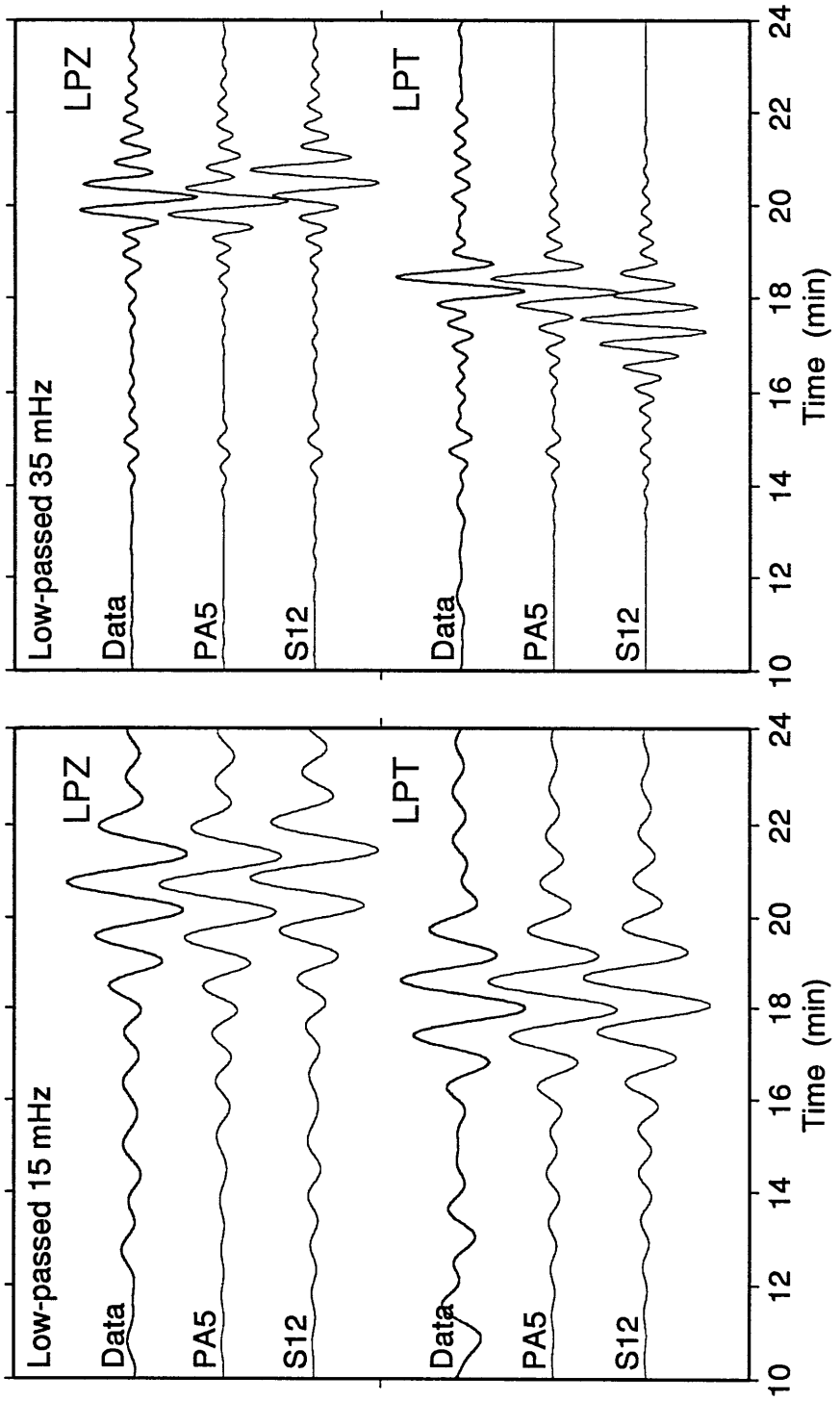
Low-passed 15 mHz
LPZ
Data
PA5
S12
LPT
Data
PA5
S12
10
12
14
16
18
20
22
24
Time (min)
Low-passed 35 mHz
LPZ
Data
PA5
S12
LPT
Data
PA5
S12
10
12
14
16
18
20
22
24
Time (min)

Figure 2.15

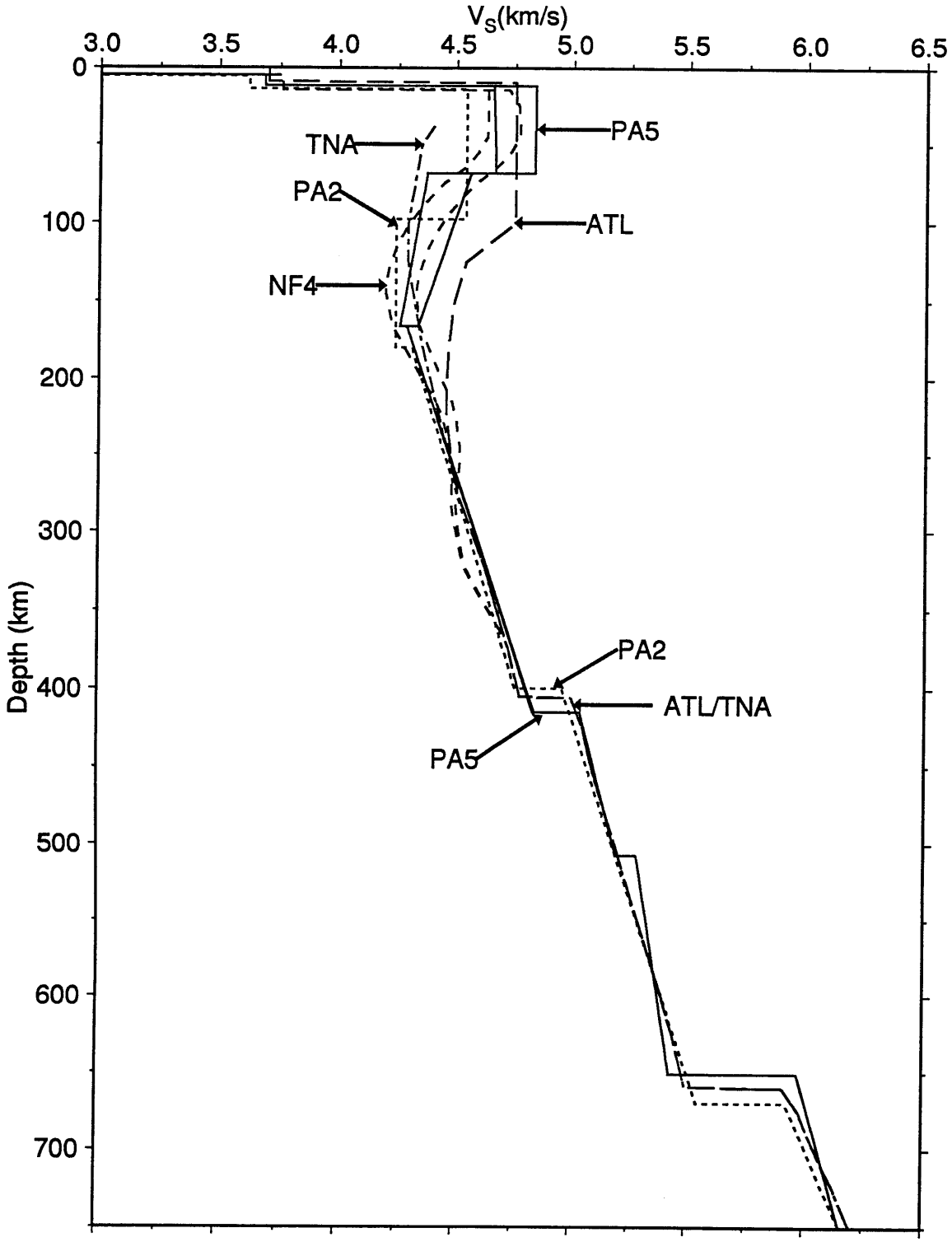
V_S(km/s)
3.0
3.5
4.0
4.5
5.0
5.5
6.0
6.5
0
100
200
300
400
500
600
700
Depth (km)
TNA
PA5
PA2
ATL
NF4
PA2
ATL/TNA
PA5

Figure 2.16

CHAPTER 3

Searching for Azimuthal Anisotropy in Western Pacific Upper Mantle

Characterization of the mantle flow field responsible for observed plate motions remains an elusive goal of geophysicists. While plate motions (relative to hotspots and each other) are generally well defined [*Minster and Jordan*, 1978; *DeMets et al.*, 1990; *Gripp and Gordon*, 1991], the extent of coupling between the plates and the underlying mantle flow is debated, leading to the need for more indirect forms of inference to discern the internal dynamic motions [e.g. *Hager et al.*, 1985; *Jordan et al.*, 1989; *Russo and Silver*, 1994].

Seismic anisotropy has long been recognized as a valuable tool for analyzing the stress, strain, and/or flow associated with plate motions [e.g. *Hess*, 1964; *Francis*, 1969]. While the accumulation of laboratory, field, and seismic observations have formed a remarkably self-consistent portrait of seismic anisotropy in mantle rocks due to olivine alignment during formation of the oceanic lithosphere [e.g. *Nicolas and Christensen*, 1987], quantifying the underlying mantle flow via this mechanism has proven elusive. This is partially due to difficulties in inferring deep seismic structure through the filter of the overlying lithosphere, but it is also due to poor constraints to the expected nature of the alignment.

Recently, a number of analyses have mapped large scale azimuthal variations in surface wave phase velocity, and have interpreted these results in terms of olivine alignment due to flow in the direction of absolute plate motion (APM). In this chapter we perform an explicit test of this hypothesis. We first develop a reasonable expectation for the form of this anisotropy by considering the current state of understanding of olivine

alignment in the upper mantle, and its relationship to dynamic flow. We then summarize the seismic observations to date, which in conjunction with forward predictions establishes the type of seismic signal for which we are searching. We then utilize our corridor analysis to examine paths that are particularly diagnostic of the potential effects of anisotropy due to APM.

ANISOTROPY IN MANTLE MINERALS

As discussed in Chapter 1, it has been generally established that upper-mantle anisotropy arises via lattice-preferred orientation (LPO) of olivine and pyroxene in mantle rocks [*Estey and Douglas*, 1986; *Nicolas and Christensen*, 1987; *Kern*, 1993]. Evidence of such alignment is abundant in experimentally-deformed samples [*Nicolas et al.*, 1973; *Zhang and Karato*, 1995], as well as in field samples from ophiolites and mantle xenoliths [*Peselnick and Nicolas*, 1978; *Christensen and Salisbury*, 1979; *Christensen and Smewing*, 1981; *Mainprice and Silver*, 1992]. In ophiolites, this alignment is well defined, with olivine *a* crystallographic axes aligned roughly perpendicular to the sheeted dikes, and *b* and *c* axes forming a girdle parallel to the dikes. Measured seismic velocities indicate that upper mantle peridotites can be represented with orthorhombic (or even hexagonal) symmetry with the fast propagation direction parallel to the axis of symmetry. This implies that seismic *P* waves should be observably fast parallel to the direction of fossil spreading in oceanic lithosphere. Regional-scale seismic refraction experiments [*Hess*, 1964; *Raitt et al.*, 1969; *Shimamura*, 1984] are remarkably consistent with these geologic observations.

While the association between sea-floor spreading direction and the direction of LPO in olivine is well established, the mechanism controlling this preferred direction is less clear. Two models have been advocated: alignment parallel to the flow plane [*Nicolas et al.*, 1973; *Nicolas and Christensen*, 1987], and alignment parallel to the strain ellipse [*McKenzie*, 1979; *Ribe*, 1992]. Recent numerical and laboratory experiments have shown

that both mechanisms are important [*Zhang and Karato*, 1995]. The former appears to hold only for the case of progressive simple shear at relatively large strains [*Ribe*, 1989, 1992; *Wenk et al.*, 1991]. The second case holds for more general shear deformation, including at smaller strains [*Ribe*, 1992; *Zhang and Karato*, 1995].

The generation of LPO is also dependent on the creep mechanism; in particular, LPO in olivine occurs via dislocation creep, but not via diffusion creep [*Nicolas and Christensen*, 1987; *Karato*, 1988, 1992]. This implies that observed anisotropy is dependent on the environmental parameters that control creep mechanisms: temperature, pressure, grain-size, stress, and activation energy and volume [e.g. *Karato and Wu*, 1993]. While the detailed behavior of some of these parameters at mantle conditions is poorly known, it is generally accepted that dislocation creep dominates in the upper few hundred kilometers of the mantle, with diffusion creep possibly becoming increasingly important at greater depths due to a decrease in grain size [*Karato*, 1992].

From these properties of lattice-preferred orientation in olivine, we form the following expectations of anisotropy in the oceanic upper mantle. First, anisotropy is presumed to be controlled by LPO in olivine, with at least orthorhombic symmetry. Within the lithosphere, the olivine is aligned with a seismically fast orientation nearly parallel to the horizontal flow direction of fossil spreading [*Ribe*, 1989]. In the hypothesized zone of anisotropy maintained below the plate by APM, we assume that the flow has generated sufficient simple shear to result in alignment parallel to the flow plane [*Ribe*, 1989; *Zhang and Karato*, 1995]. These assumptions imply that the symmetries apparent in laboratory and outcrop samples of peridotite rocks are maintained in deeper deformation. While this assumption may prove to be too strong, it allows us to perform a search for this simple form of anisotropy.

PREVIOUS OBSERVATIONS OF AZIMUTHAL ANISOTROPY

As noted above, azimuthal variations in the travel times of refracted *P* waves [*Hess*, 1964; *Raitt et al.*, 1969; *Shimamura*, 1984] are in excellent agreement with the laboratory and field observations of LPO, and *Francis's* [1969] model of olivine alignment in the lithosphere parallel to the plate spreading direction is now accepted as the starting point of anisotropic models of oceanic upper mantle. Refracted *P* waves give little depth resolution, however, and other observations are required to extend the anisotropy into the lower lithosphere and asthenosphere.

Surface waves provide a means of detecting anisotropy at greater depths in the upper mantle. Based on *Backus's* [1965] result for *P* waves, *Smith and Dahlen* [1973] first demonstrated that a slight general anisotropic media gives rise to an azimuthal dependence of the phase velocities of both Love and Rayleigh waves of the form

$$c(\omega,\theta) = A_1(\omega) + A_2(\omega)\cos2\theta + A_3(\omega)\sin2\theta + A_4(\omega)\cos4\theta + A_5(\omega)\sin4\theta,$$

where $c(\omega)$ is phase velocity as a function of frequency and θ represents azimuth. The five constants A_i are dependent on the form and magnitude of the anisotropic perturbation to the isotropic media. To illustrate these relationships, *Maupin* [1985] explored the variation of Love and Rayleigh phase velocities for a simple model of olivine alignment with a horizontal axis of symmetry, similar to the one being considered here (Figure 2.1). For anisotropy generated by such a media, the Rayleigh wave phase velocities display a strong 2θ variation, while Love waves display a 4θ dependence. The magnitude of this variation is dependent on the magnitude of the anisotropy, but the general pattern depends only on the direction of the symmetry axis.

Forsyth [1975a] first reported observations of azimuthal variations of long-period surface waves (in particular, a 2θ variation in Rayleigh waves), with an apparent fast direction parallel to the fossil spreading direction in the Nazca plate. While surface waves improve the depth sampling of potential anisotropic structure, they also require long propagation paths, and thus along-path isotropic heterogeneity must be accounted for in the

anisotropic analysis. In general, two methodologies have been employed: regionalization of the phase velocities according to *a priori* models of the age of the sea floor [*Forsyth*, 1975a; *Nishimura and Forsyth*, 1988], and formal inversion for 2-dimensional maps of the phase velocity variations without assuming an age model [*Tanimoto and Anderson*, 1985; *Montagner*, 1986; *Suetsugu and Nakanishi*, 1987; *Montagner and Tanimoto*, 1990]. Both are equivalent in that they allow for known variations due to thermal structure of oceanic plates to be absorbed in the azimuthally invariant A_1 term in the expression for phase velocity; the latter is less restrictive in that it does not presume the form of the variations. The result of these processes are maps of the azimuthal terms of the phase velocity expansion.

In practice, there are several subtle differences in these analyses, primarily in the data utilized and assumptions on the allowable form of the anisotropy. First, many of the analyses have relied entirely on the azimuthal behavior of Rayleigh waves [*Montagner*, 1986; *Suetsugu and Nakanishi*, 1987; *Nishimura and Forsyth*, 1988]. This is justified by the fact that Rayleigh waves display significant (2%) azimuthal variations, while Love wave variations are more difficult to discern [e.g. *Forsyth*, 1975a; *Kawasaki and Kon'no*, 1984; *Nishimura and Forsyth*, 1989]. This is possibly due to the fact that Love waves will display a dominant 4θ variation for an orthorhombic symmetry with a roughly horizontal axis (e.g. Figure 3.1), and thus is averaged out more easily that the slower 2θ variation of Rayleigh waves. Alternatively, the small Love wave variation could be due to the intrinsic nature of the elasticity tensor for olivine [*Kawasaki and Kon'no*, 1984]. In addition, Rayleigh wave variations are assumed to have a 2θ pattern (i.e. the 4θ terms are ignored). This is justified on expected symmetry arguments (Figure 3.1; also *Montagner and Nataf* [1986]). However, it should be noted that some analyses that incorporate the complete 2θ and 4θ description of Love and Rayleigh waves find azimuthal anisotropy that obeys no symmetry conditions; the azimuthal behavior of Love and Rayleigh waves are often

inconsistent with a single fast direction, for example. *Montagner and Nataf* [1988] and *Tanimoto and Anderson* [1990] briefly discuss the implications of such structure.

Figure 3.2 presents three examples of the results of these analyses, two for the Pacific, and one global. The data sets and modeling procedures differ, but the authors of all three analyses come to the same conclusion: observed azimuthal anisotropy of 1-2% correlates well with APM. Close inspection of these figures implies that this may be an over-simplification. While it is clear that azimuthal anisotropy is quite strong near spreading centers, with a fast direction parallel to spreading, it is not clear that the correlation holds for the western Pacific, where APM deviates substantially from the direction of fossil spreading frozen in the lithosphere. *Nishimura and Forsyth* [1988] argue that the apparent reduction in anisotropy due to APM in the western Pacific is because of destructive interference between the APM and lithospheric signals, or because of uncertainties associated with regionalization due to the complex spreading history in the western Pacific. This is problematic because it is precisely in these regions that an anisotropy/APM correlation is unique; at younger ages, the effects of APM cannot be separated from the effects of fossil spreading. These uncertainties arise because the inference on anisotropy is still in the form of phase velocities at discrete frequencies, which integrate the lithospheric and underlying asthenospheric signals.

Recently, this shortcoming has been addressed by formulation of an approach to invert the Love and Rayleigh wave phase velocities maps (such as those in Figure 3.2a-c) for three-dimensional maps of the complete velocity description of the upper mantle, with anisotropic terms directly incorporated [*Montagner and Nataf*, 1986, 1988; *Montagner and Jobert*, 1988; *Montagner and Tanimoto*, 1991]. These models thus describe the azimuthal anisotropy as a function of depth, ostensibly separating the lithospheric and asthenospheric signals. The shear-wave azimuthal anisotropy at 200 km depth inferred globally [*Montagner and Tanimoto*, 1991] is presented in Figure 3.2d. Based on this figure, Montagner and Tanimoto's conclusion that anisotropy agrees well with APM beneath the

Pacific is debatable. In addition, Montagner and Tanimoto invert for all 6 independent 2θ and 4θ terms in the description of the velocities, with *a priori* correlations enforced between them, but no strict assumptions on symmetry were made. This makes it very difficult to interpret this result in terms of simple models of olivine alignment. Their technique can resolve a general (slight) anisotropy with any orientation, but it is not clear how the inferred anisotropy relates to the symmetries implicitly assumed when relating anisotropy to flow in peridotite rocks. An example of this is that the result presented in Figure 3.2d gives the fast direction of shear wave anisotropy. If the other anisotropy parameters are independent, this "fast direction" may be entirely different for *P* velocities, making it difficult to interpret the anisotropy in a simple way. *Montagner and Tanimoto* [1991] acknowledge that strict symmetry assumptions (such as those suggested by *Montagner and Nataf* [1988]) would simplify the interpretation of their model, but to date analyses incorporating such assumptions have been performed only in selected regions [*Montagner and Jobert*, 1988].

SKS splitting observations have also been used to argue for a correlation between anisotropy and APM, primarily using widely-spaced point observations from the continents [*Vinnik et al.*, 1992, 1995]. Recently, suboceanic anisotropy has been investigated using split shear waves that reflect from the surface beneath oceanic regions, providing an estimate of splitting near the bounce point [*Su and Park*, 1994; *Farra and Vinnik*, 1994]. These observations have little depth resolution, and thus separation of lithospheric and asthenospheric signals is difficult. In general, the fast directions inferred from these observations are highly variable, with no convincing pattern of anisotropy strongly correlated with current plate motion.

It is our conclusion that these previous studies have failed to illustrate a clear correlation between APM and azimuthal anisotropy in the western Pacific. We further investigate this hypothesized correlation.

TESTS FOR AZIMUTHAL ANISOTROPY IN THE WESTERN PACIFIC USING PA5

The primary evidence of anisotropy in data collected along a single azimuth is the *LR* discrepancy and the associated phenomenon (*SH-SV* splitting) observed in the upper-mantle shear waves. Assuming the simple model of olivine alignment presented above, the magnitude of the *LR* discrepancy and *SH-SV* splitting (and thus the inferred magnitude of v_{SH}-v_{SV} differences) is strongly dependent on the angle between the propagation azimuth and the fast-axis direction, as shown in Figure 3.1 [*Maupin*, 1985]. Note that this behavior assumes a constant angle between the propagation and fast-axis directions; if this angle varies significantly, the phase-velocity behavior will be averaged across the relevant angular region, with complete azimuthal averaging resulting in a transversely isotropic model with $v_{SH} > v_{SV}$ [e.g. *Dziewonski and Anderson*, 1981]. This behavior implies that the form and magnitude of anisotropy found in PA5 holds for azimuths oblique or perpendicular to a constant fast direction, but azimuths roughly parallel to the fast direction will result in models that are isotropic or even have "negative" ($v_{SV} > v_{SH}$) anisotropy.

We search for anisotropy due to APM by comparing our observations from the Tonga/Fiji corridor to some new observations from the Kurils recorded at Oahu (Figure 3.3). This new path is nearly parallel to the current motion of the Pacific plate relative to a hotspot reference frame, while that for Tonga-Fiji is perpendicular to this motion (arrows in Figure 3.3). According to Figure 3.1, the Love wave phase velocities should be relatively invariant between these two paths, while the Rayleigh waves from the Kurils should be up to 20-s fast relative to those from Tonga-Fiji, with the magnitude of the Rayleigh wave variation dependent on the strength of the anisotropy. In addition, the Kuril corridor samples plate structure nearly identical to that in the Tonga-Fiji corridor (isochrons in Figure 3.3), essentially controlling for age-dependent thermal structure and fossil-spreading anisotropy in the lithosphere. This eliminates the need for regionalizing according to plate age; in fact, the age span (100-120 Ma) crossed by our corridors is much smaller than that typically assumed in regionalization [e.g. *Nishimura and Forsyth*, 1988,

1989]. The assumption of similar plate structure is further verified by comparing high-frequency surface waves that are restricted to the lithosphere. These corridors form an ideal experimental geometry to search for azimuthal anisotropy due to current plate motion.

We first test for an azimuthal signature by comparing the average frequency-dependent phase delays of surface and multiply-reflected body waves from the Kurils and Tonga-Fiji (Figure 3.4), relative to isotropic model PA2; surface wave residuals from an azimuthally-intermediate corridor from the Aleutians (Figure 3.3) are also shown for comparison. If APM were responsible for the observed polarization anisotropy, then the *LR* discrepancy and SS_H-SS_V splitting should be greatly reduced for the Kuril path, especially at the lowest frequencies. To the contrary, the phase delays are slightly larger for the Kuril path, and the Aleutian path is quite similar. Small variations (up to 5 s) in phase delays are observed for the different paths, but these are probably due to the effects of isotropic heterogeneity between the paths. To first order, such heterogeneity perturbs vertical/radial and tangential waveforms in the same way, thus, while the individual phases are sensitive to it, the differential times of equivalent phases (for example, G_1-R_1, or SS_H - SS_V) will be largely independent of it. The nearly identical splitting in the R_1/G_1, *SS*, and *SSS* phases from the three corridors implies that the path-averaged anisotropy is quite similar throughout the western Pacific, and PA5 provides an excellent radial model for this structure.

Using PA5 as a reference model, we examine the phase delays from the Kuril events in more detail. The Kuril path itself spans a 30° range of source-receiver azimuths, and we thus look for azimuthal behavior in the individual observations. Figure 3.5 presents individual Rayleigh, Love, SS_V, and SS_H phase delays relative to PA5 at three frequencies as a function of azimuth. The presence of APM would present itself in two forms in this Figure. First, the lowest frequency (15 mHz) Rayleigh waves should be fast relative to PA5: 1% azimuthal variation between the Tonga and Kuril corridors would correspond to an average $\delta\tau_P$ of -12 s for R_1 in Figure 3.5a. These observations average

around -3 s, implying a difference in phase velocity of less than 0.25%. Second, APM for these paths corresponds to an azimuth span of 115-125°, and if it were present the R_1 phase delays would have a minimum at this azimuth, while the tangential phase delays would display a maximum. Assuming a 1% (peak-to-peak) azimuthal signal, the variation in the lowest frequency surface waves within this 30° window would span approximately 6 s in each component, with a 12-s variation in their difference. Despite the scatter in the data, it is clear that the phase delays have no azimuthal trend over this azimuth span. While the detailed behavior of the *SS* and *SSS* body waves (Figure 3.5d-f) is harder to predict, their general pattern should be similar to that for the surface waves, with a peak to peak amplitude of up to 6 s [*Kuo et al.*, 1987]. Again, they display no general offset relative to PA5, and no smooth azimuthal trend is observed. Finally, by examining the azimuthal behavior of the highest frequency surface waves (Figure 3.5c), we can justify our assumption that the lithospheric anisotropy is similar between the two paths. In particular, no resolvable offset relative to PA5 is observed in the Rayleigh waves, no resolvable azimuthal trend, and the *LR* discrepancy is quite similar. Thus azimuthal anisotropy from the lithosphere should not be interfering with a deeper APM signal.

One interesting feature that appears in Figure 3.5 is the abrupt appearance of large negative travel-time residuals in G_1 and SS_H at 35 mHz near an azimuth of 107°. This behavior is unlikely to be caused by large-scale APM anisotropy for several reasons: it is observed exclusively in *SH* phases, while *SV* phases have generally been found to be most diagnostic of azimuthal anisotropy; its abrupt nature is inconsistent with the expected smooth azimuthal variation; and it is restricted to the highest-frequency surface waves. It is more likely due to an rapid change in anisotropic plate structure. Alternatively, because G_1 and SS_H at 35 mHz sample not just the lid but the sub-LVZ gradient region (see Figures 2.6c and 2.8), it could be due to sharp isotropic heterogeneity located between 200-400 km depth.

We quantify the differences between the Kuril and Tonga corridors by inverting the Kuril data for perturbations to PA5. Since we lack *ScS*-reverberation data for the Kuril path, we assume that it has the same discontinuity structure as PA5. The *S, SS, SSS,* and surface wave phase delays (Figure 3.5) are inverted using the procedure presented in Chapter 2. We force the difference into the upper mantle by more strictly minimizing perturbations to the structure deeper than 400 km; the fit to the *SS* and *SSS* observations is slightly compromised by this procedure, but we want to force as much heterogeneity as possible in to the LVZ and gradient region, where potential azimuthal anisotropy effects should be dominant. The resulting model (Figure 3.6) is nearly identical to PA5; the lid is slightly less anisotropic (3.9% vs. 4.1% in shear anisotropy), perhaps due to the different averaging of the heterogeneous fossil spreading signature in the plate, and the velocity near 170-200 km is slightly faster. This is in direct contrast to the predictions of azimuthal anisotropy presented in Figure 3.1, which indicate that LVZ anisotropy should be minimal (isotropic, or even negative) along a path parallel to current plate motion. The similarity of LVZ anisotropy between these two paths strongly argues that large-scale azimuthal anisotropy is not a significant contributor to the anisotropic signature.

DISCUSSION

We have utilized laboratory, geological, and numerical models of olivine alignment in the upper mantle to formulate a reasonable expectation for the form of azimuthal anisotropy generated by absolute plate motion in the sublithospheric oceanic mantle. Using this expectation as a guide, we have searched the western Pacific for azimuthal anisotropy associated with this mechanism, and failed to find it. This result is in agreement with that of *Nishimura and Forsyth* [1988], who found no correlation between the azimuthal variation of regionalized surface waves and current plate motion in the older (> 80 My) regions of the Pacific. They chose not to interpret this result as evidence against large-scale alignment from APM due to their inability to account for interference between anisotropic

effects of the fossil spreading and APM. Our results account for the anisotropy in the lithosphere by restricting our analysis to two corridors sampling very similar lithospheric structure, and we still find no evidence of deeper-seated azimuthal anisotropy.

If sublithospheric azimuthal anisotropy does not look like APM, what does it look like? The strong similarity between the anisotropic signatures from the Kuril and Tonga-Fiji corridors imply that azimuthal anisotropy in western Pacific upper mantle is effectively averaged out over 40° path lengths (i.e. it varies azimuthally with the length scale of the variation being substantially less than 40°). Assuming that convective flow in the mantle is responsible for the sub-lid anisotropy, this flow must therefore have length scales smaller than the plate. Dynamic flow driven by plumes and hotspots [e.g. *Larson*, 1991] provide one possibility, small-scale convective instabilities [e.g. *Parsons and McKenzie*, 1978] another. This flow must obviously be decoupled from the overlying plate motion; such decoupling was recently advocated near the subducting Nazca plate beneath South America [*Russo and Silver*, 1994]. Close examination of *Montagner and Tanimoto's* [1991] model (Figure 3.2d) implies such decoupling in several regions where the inferred anisotropy at 200 km depth deviates substantially from APM, including near the Kuril subduction zone.

Finally, what if our simple model of anisotropy (at least orthorhombic symmetry, with a fast axis parallel to the direction of flow) is incorrect for sublithospheric anisotropy? In this case, we can say nothing about dynamic flow from anisotropy. This holds for all analyses of azimuthal anisotropy, not just ours. Even analyses that solve for more general forms of anisotropy in the upper mantle [*Montagner and Tanimoto* , 1991] require similar assumptions in order to interpret their results in terms of a flow field, as do shear wave splitting analyses. As such, our assumption is no more restrictive than in other studies that search for similar structure, and it will require further advances in our knowledge of olivine deformation under mantle conditions [e.g. *Zhang and Karato*, 1995] to significantly improve these assumptions.

FIGURE CAPTIONS

Fig. 3.1 Phase velocity anomalies of fundamental mode (left) and first higher-mode (right) surface waves as a function of propagation azimuth, for a model of olivine with a symmetry axis oriented horizontally with an azimuth of 0°, relative to an isotropic model. Olivine is distributed throughout the upper mantle, with 1/6 of the crystals perfectly aligned. Rayleigh waves are labeled with an R, and Love waves with an L. Period of observation is 60 s. Propagation parallel to the axis of symmetry results in fast Rayleigh waves and slow Love waves, while the opposite is true for all azimuths larger than 30° away from the axis of symmetry. Figure from *Maupin* [1985].

Fig. 3.2. Examples of azimuthal anisotropy inferred from various analyses of long-period surface waves. The first three maps represent the 2θ component of the azimuthal variation of long-period Rayleigh waves, at roughly equivalent periods. The line segments indicate the fast Rayleigh wave propagation direction at each point. Maximum phase-velocity variations are listed on each panel, in percent. a) Azimuthal phase-velocity variations in the Pacific at a period of 83 s [*Suetsugu and Nakanishi*, 1987]. b) Azimuthal phase-velocity variations in the Pacific at 91 s [*Nishimura and Forsyth*, 1988]. c) Global azimuthal phase-velocity variations at 91 s [*Montagner and Tanimoto*, 1990]. d) The last panel displays a depth slice of the 2θ component of shear wave anisotropy from a global three-dimensional anisotropic model of the mantle, at 200 km depth. Line segments indicate the fast propagation direction. Maximum anisotropy is expressed in GPa [*Montagner and Tanimoto, 1991*]. In each case the maps are taken unaltered from the referenced paper.

Fig. 3.3. Mercator projection map of the western Pacific, highlighting the additional western Pacific paths utilized to assess the azimuthal variability of upper mantle anisotropy in this region. In particular, note the significant difference in the angle between the Kuril-

KIP path and the direction of current plate motion (nearly parallel), relative to the Tonga-KIP path (nearly perpendicular). Since the plate age is relatively constant between these two paths, this allows for a controlled experiment to evaluate the plate-motion signature of anisotropy. Also shown as an intermediate path from the Aleutians.

Fig. 3.4. Comparison of the *LR* discrepancy and SS_H - SS_V splitting between the three paths. Similarity of the splitting observations indicates that western Pacific upper mantle is largely radially anisotropic (and not azimuthally anisotropic) over these path lengths. In particular, similarity between the Kuril and Tonga/Fiji paths indicate that the current plate motion is not responsible for the bulk of the observed signal.

Fig. 3.5. Raw phase delays from the Kuril events, as a function of source-receiver azimuth. a) R_1 and G_1, at 15 mHz. b) R_1 and G_1, at 25 mHz. c) R_1 and G_1, at 35 mHz. d) SS_H, SSS_H, SS_V, and SSS_V, at 15 mHz. e) SS_H, SSS_H, SS_V, and SSS_V, at 25 mHz. f) SS_H, SSS_H, SS_V, and SSS_V, at 35 mHz. Error bars are *a priori* estimates.

Fig. 3.6. Summary of the frequency-dependent travel time data from the Kuril events. Phase delays are categorized by phase type (Surface wave, *SSS* , *SS*, or *S*), and then separated into tangential (*SH*) or radial/vertical (*SV*) observations, and averaged in each frequency band. Symbols represent the residuals relative to PA5, while the lines represent the predicted fit of the perturbation to these data. Little additional splitting is observed relative to PA5. a) Love and Rayleigh waves. b) *SSS* and *sSS* waves. c) *SS* waves. d) *S* waves. Over 1300 observations are represented. Error bars are determined by a weighted average of estimated *a priori* errors.

Fig. 3.7. Model for the Kuril path (solid line), compared to model PA5 (dashed line). From left to right, η, density, shear velocities, and compressional velocities are plotted as a

function of depth. The similarity between the Kuril model and PA5 indicate that large-scale azimuthal anisotropy aligned with current plate motion does not exist beneath this part of the western Pacific.

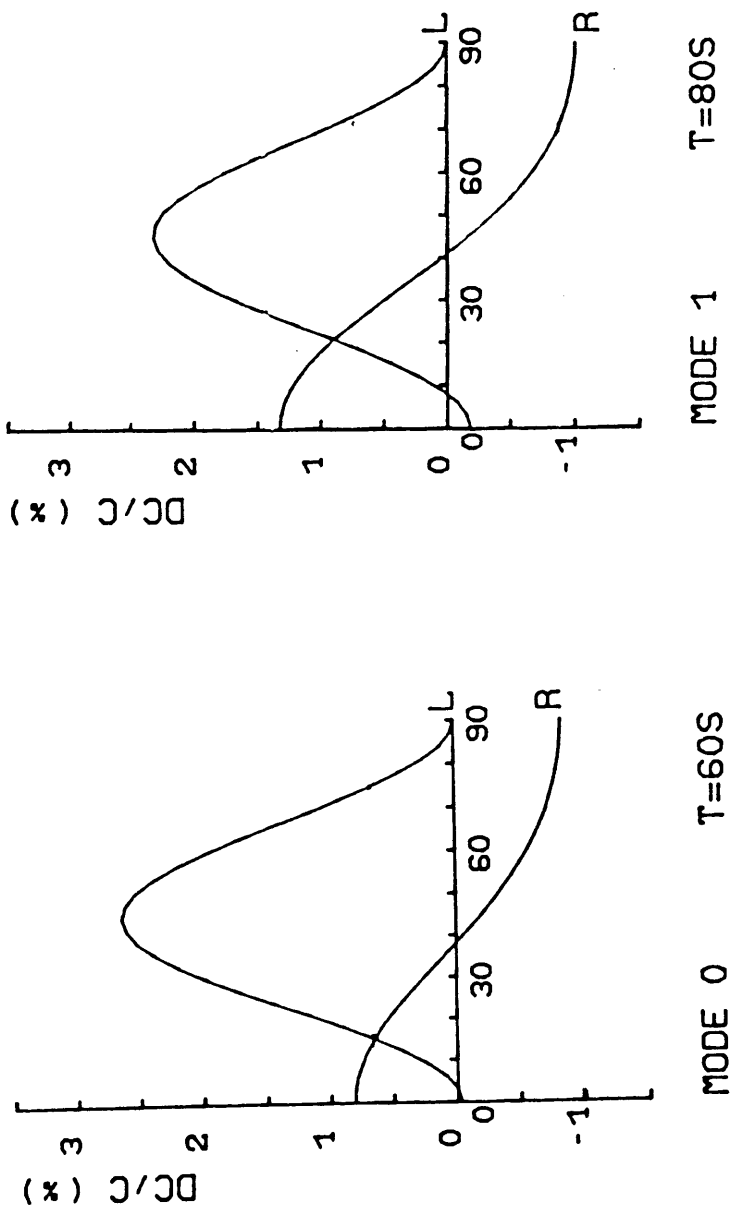
DC/C (x)
3
2
1
0
-1
0
30
60
90
L
R
MODE 1
T=80S
DC/C (x)
3
2
1
0
-1
0
30
60
90
L
R
MODE 0
T=60S

Figure 3.1

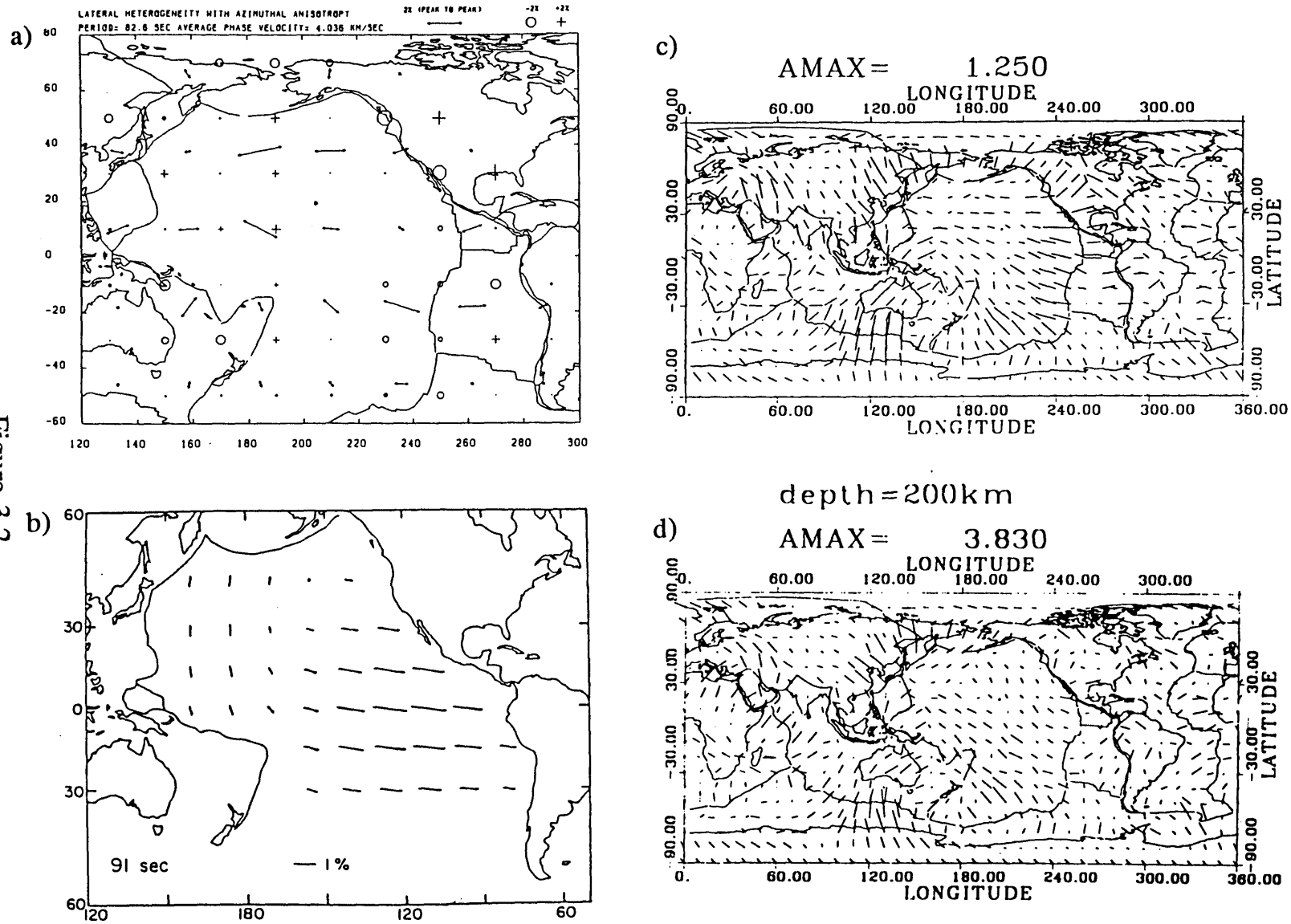
a)
LATERAL HETEROGENEITY WITH AZIMUTHAL ANISOTROPY
2% (PEAK TO PEAK)
-2%
+2%
PERIOD= 82.6 SEC AVERAGE PHASE VELOCITY= 4.036 KM/SEC
b)
91 sec
— 1%
c)
AMAX= 1.250
LONGITUDE
LATITUDE
depth=200km
d)
AMAX= 3.830
LONGITUDE
LATITUDE

Figure 3.2

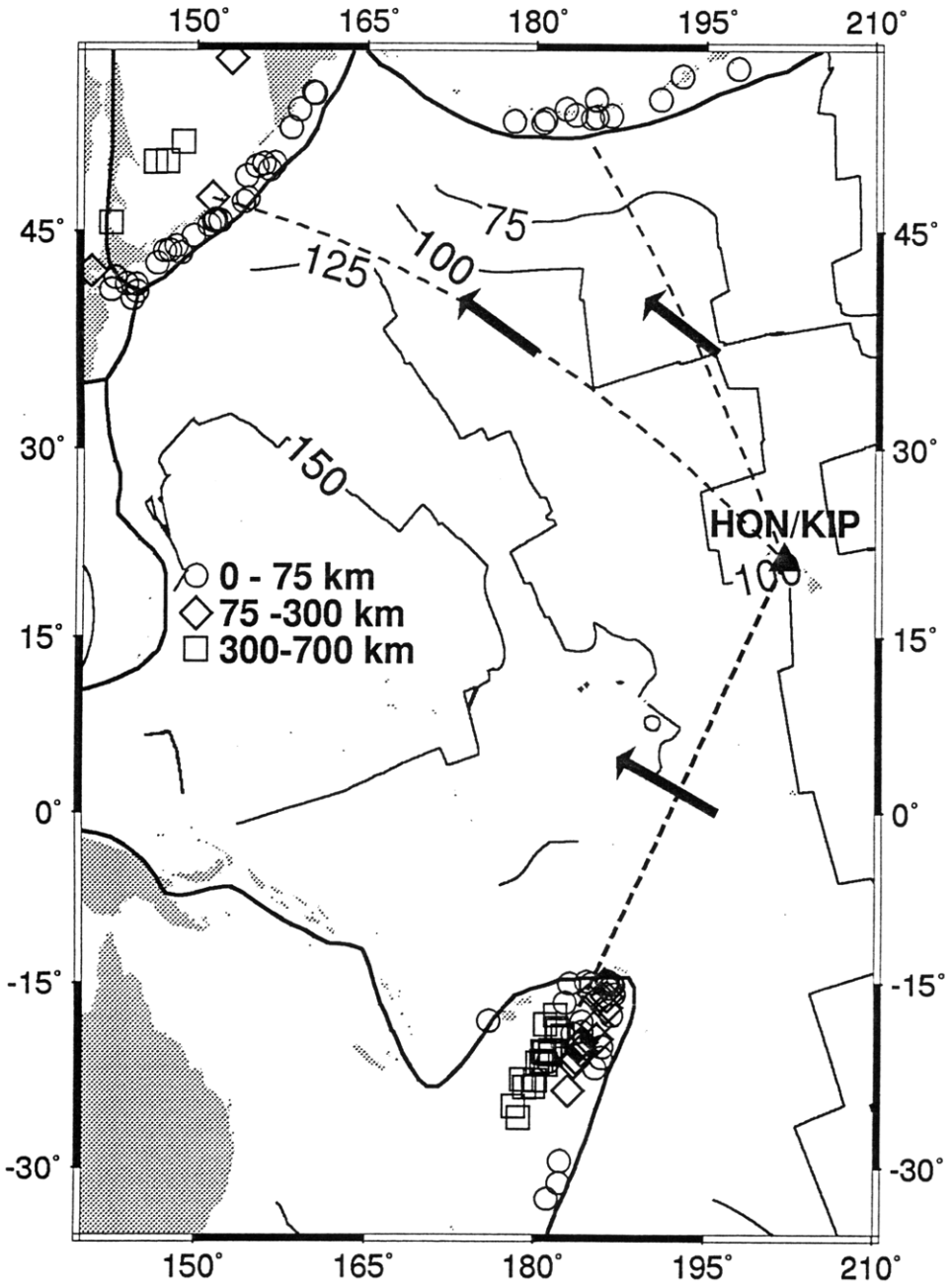
150°
165°
180°
195°
210°
45°
30°
15°
0°
-15°
-30°
75
100
125
150
HQN/KIP
0 - 75 km
75 -300 km
300-700 km

Figure 3.3

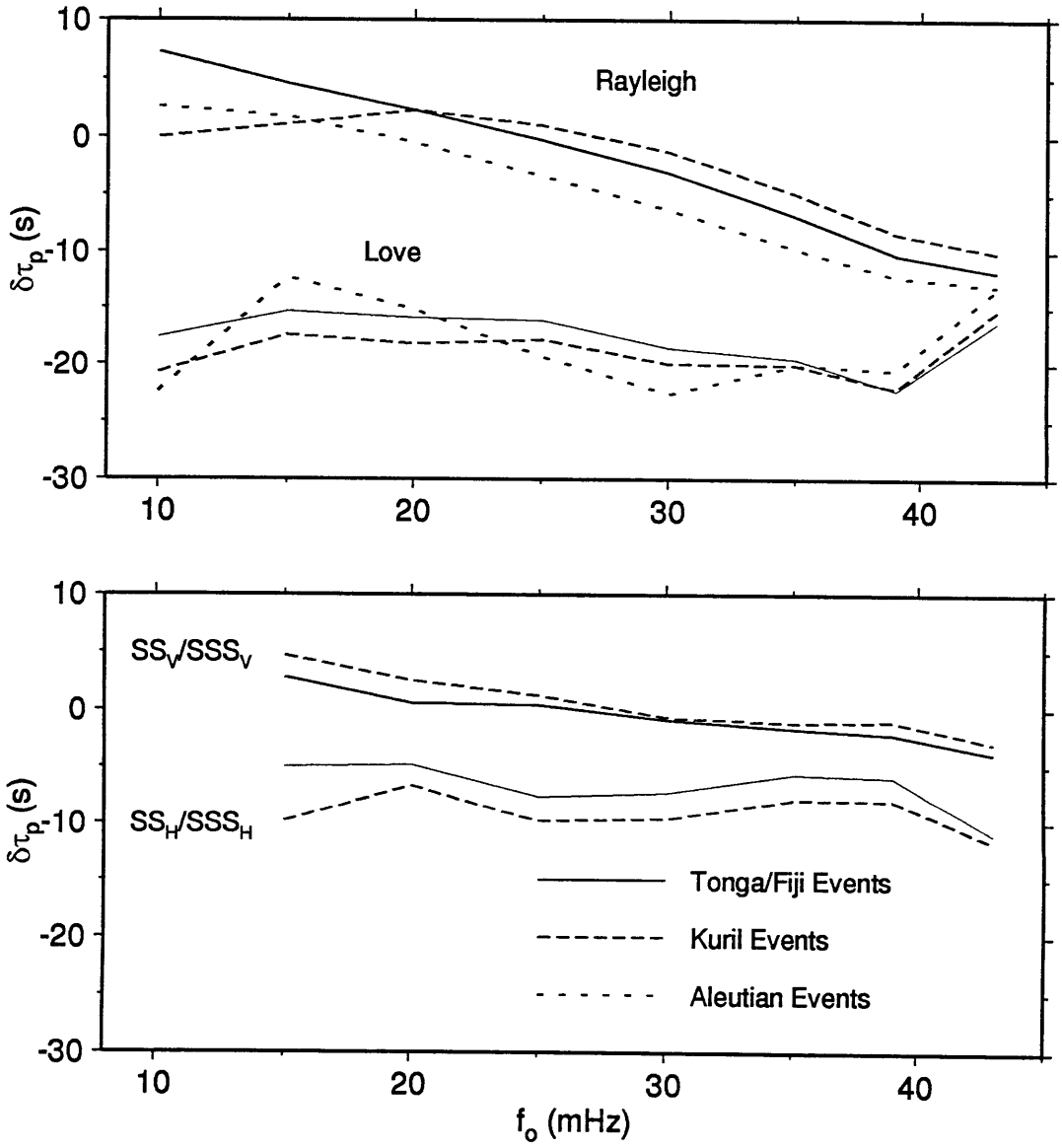
Rayleigh
Love
$\delta\tau_p$ (s)
10
0
-10
-20
-30
10
20
30
40
SS_V/SSS_V
SS_H/SSS_H
Tonga/Fiji Events
Kuril Events
Aleutian Events
f_o (mHz)

Figure 3.4

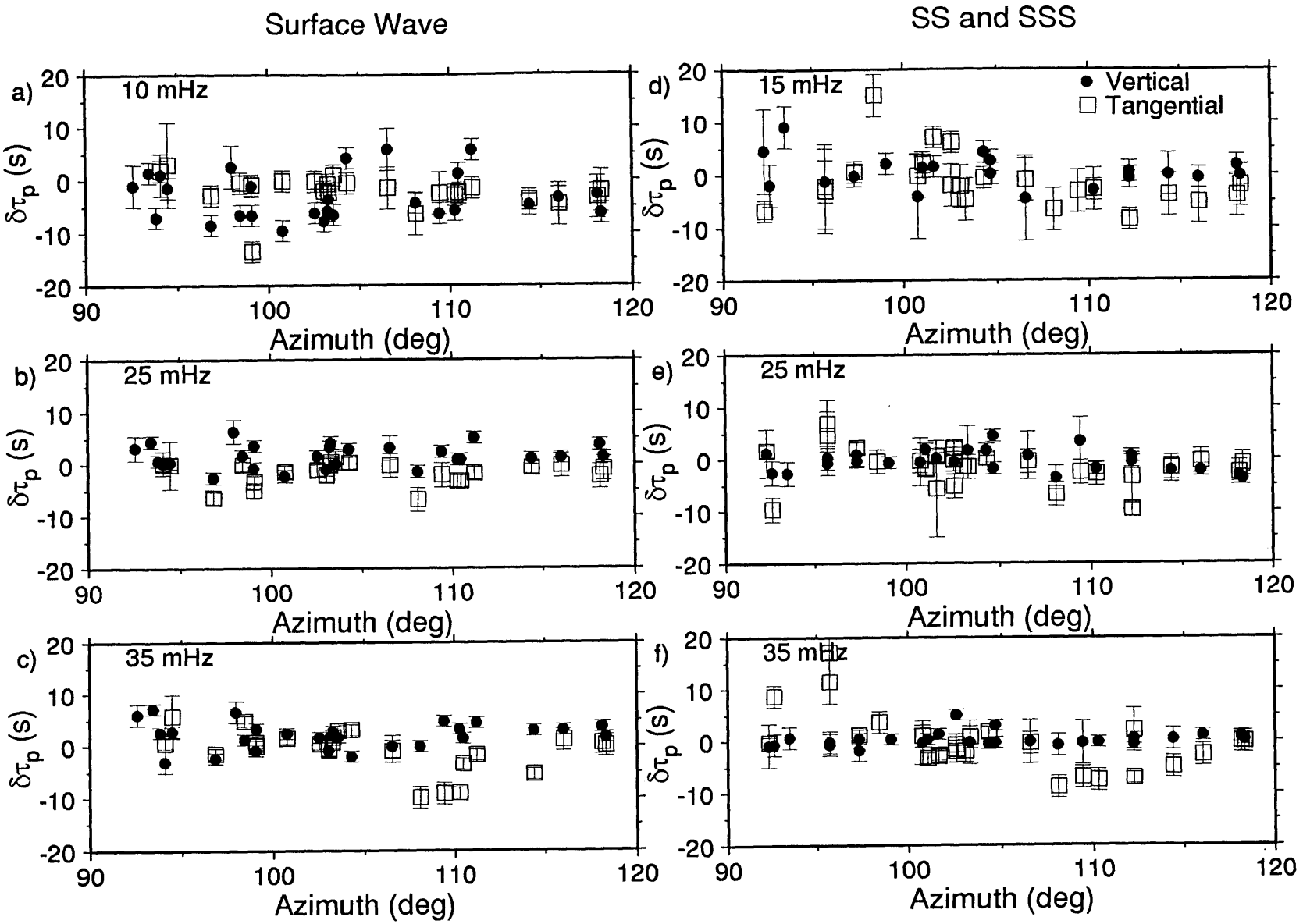
Surface Wave
SS and SSS
a)
10 mHz
b)
25 mHz
c)
35 mHz
d)
15 mHz
e)
25 mHz
f)
35 mHz
Vertical
Tangential
$\delta\tau_p$ (s)
Azimuth (deg)
20
10
0
-10
-20
90
100
110
120

Figure 3.5

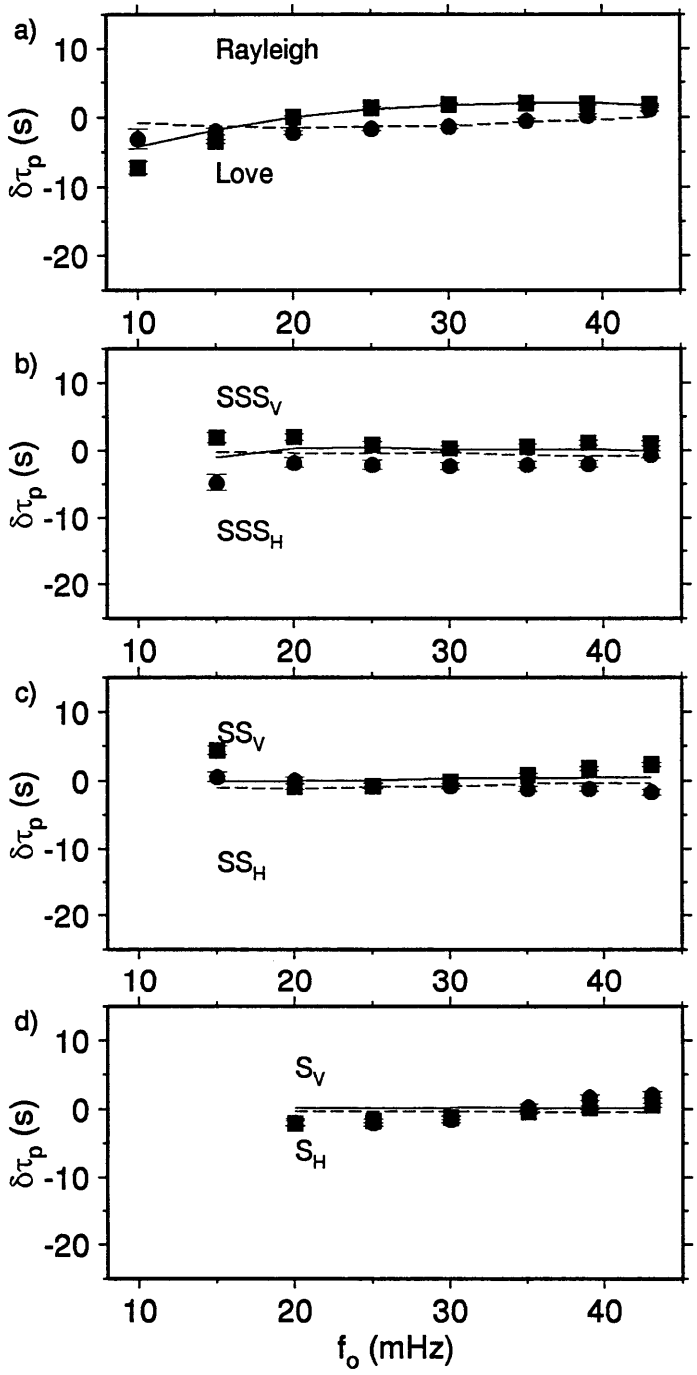
a)
Rayleigh
Love
b)
SSS$_V$
SSS$_H$
c)
SS$_V$
SS$_H$
d)
S$_V$
S$_H$
$\delta\tau_p$ (s)
10
0
-10
-20
10
20
30
40
f_o (mHz)

Figure 3.6

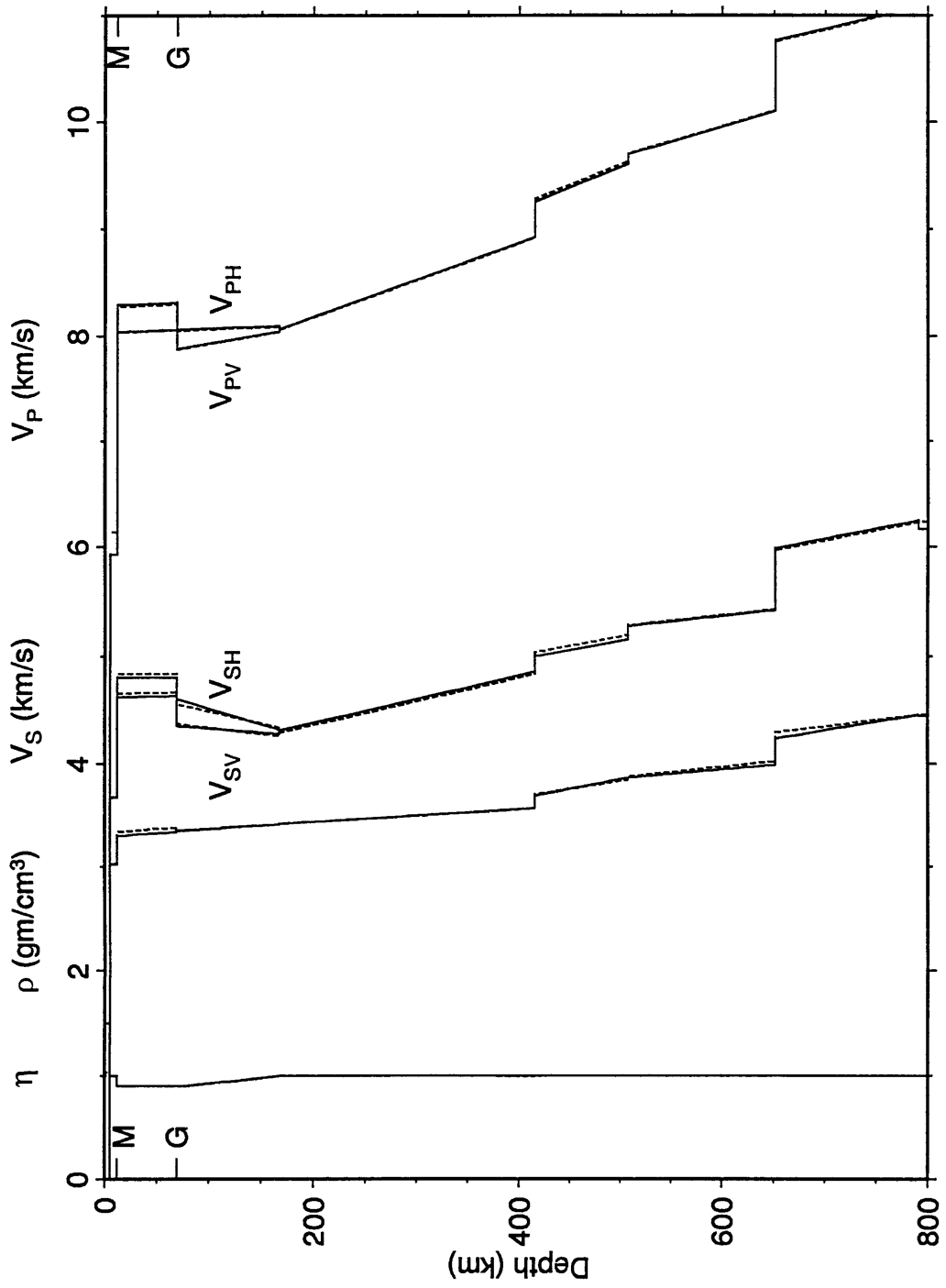
M
G
V_{PH}
V_{PV}
V_{SH}
V_{SV}
V_P (km/s)
V_S (km/s)
ρ (gm/cm³)
η
0
2
4
6
8
10
0
200
400
600
800
Depth (km)

Figure 3.7

CHAPTER 4

A Radially Anisotropic Model of the Upper Mantle in an Australian Corridor

The comparison between continental and oceanic models in Figure 1.2 implies substantial differences in upper mantle structure between these tectonic environments, but these differences have never been clearly established in anisotropic models. This is most likely because the regionalized surface wave analyses that have been successful in evaluating oceanic regions are much more difficult in continents where variability in tectonic style and crustal structure is more heterogeneous. Rapid changes in crustal structure can severely scatter surface waves, so propagation paths must be carefully selected to be long enough to resolve structure to transition zone depths, yet still have minimal lateral variability over their lengths. Given the relatively sparse distribution of seismicity and stations, this requirement is quite restrictive, and thus regional anisotropic models of continental upper mantle are rare [*McEvilly*, 1964; *Leveque and Cara*, 1983, 1985; *Mitchell*, 1984; *Gee and Jordan*, 1988].

We have succeeded in isolating a seismic corridor that is largely restricted to the Phanerozoic platform and Precambrian shield regions that characterize stable continental cratons, with minimal contamination from oceanic or tectonically-active structure. This corridor connects the New Guinea and New Britain seismic zones and station NWAO in southwestern Australia (Figure 4.1), with stable continental structure characterizing over 60% of the path. Surface geology indicates that western Australia was constructed during two tectonic regimes in the Archean and Proterozoic that supported the progressive growth of the continental platform to the north and east [*Rutland*, 1981; see also *Plumb*, 1979; *Gee*, 1979]. Since 1400 Ma, tectonic activity in Australia has consisted of growth

and deformation restricted to the eastern third of the continent (south and east of our corridor), while western Australia has remained stable. The topography reflects this stability; the mean altitude of our profile is sea level, and the median (reflecting the continental portion) is less than 300 m.

Western Australia is characterized in global tomographic models as several percent fast throughout the upper mantle [*Zhang and Tanimoto*, 1993; *Su et al.*, 1994], roughly similar to other shield regions. Higher-resolution regional analyses also have produced models that are in general agreement with other stable continents [*Hales et al,* 1980; *Drummond et al.*, 1983; *Levin*, 1985; *Bowman and Kennett*, 1993; *Kennett et al.*, 1994]. However, the limited data types (refracted high-frequency *P* waves, high-frequency *Sn* phases restricted to the lithosphere), and/or restricted sampling regions (generally the northern margin of the continent) make it difficult to compare these models to those presented in Figure 1.2, for example. The lack of a good long-period *P*-wave, *S*-wave, and density starting model for our analysis (such as PA2 in Chapter 2) leads us to develop our own. We dub this isotropic starting model AU1, and it has been constructed using EU2 and SNA as a guide, with the constraint that it roughly predict (via forward modeling) the *ScS* reverberation, *S*, *SS*, and surface wave data presented in the next section.

An ambiguity in constructing AU1 is specifying the crustal structure, which is poorly determined in Australia [*Mooney*, 1994]. Using *ScS* reverberation results [*Revenaugh and Jordan,* 1991a], we incorporate a single layer crust with a Moho at 30 km depth, which represents the path-average of the continental and margin crustal structure. While upper mantle models from Australia [*Hales et al,* 1980; *Drummond et al.*, 1983; *Bowman and Kennett,* 1990, 1993; *Kennett et al.*, 1994] typically include a two-layer crust with a slightly deeper Moho (33-40 km depth), we are dissuaded from imposing such a structure because it does not incorporate along-path averaging. Also, we note than none of the models with a deeper Moho include a Hales discontinuity, i.e. the

velocity jumps directly from crustal to typical "lithospheric" values (v_S > 4.5 km/s, v_P > 8 km/s). The model presented below includes an H discontinuity that, when paired with the shallow Moho, produces an average velocity value that is very similar to these other models through the upper 60 km. It is also qualitatively similar to regional surface wave analyses of crustal structure from western Australia [*Ellis and Denham*, 1985], which incorporate several velocity jumps between 10 and 50 km before reaching "lithospheric" values.

We present here a radially anisotropic model for this corridor, which contrasts sharply with the models for the oceanic corridors presented in Chapters 2 and 3. The model parameterization and analysis is very similar to that presented in Chapter 2, to which we refer for much of the general discussion. The Australian data are distinct from those in the Pacific in several significant aspects, however, resulting in subtle differences in processing that require a fairly complete discussion.

ScS REVERBERATION DATA

Like the Pacific path (Chapter 2), this corridor has been examined using *ScS* reverberations [*Revenaugh and Jordan*, 1991a-d]. This analysis provides whole mantle travel time and Q estimates, and impedance contrast and vertical travel times for internal mantle discontinuities (Figure 4.2). The reflectivity profile is characterized by Hales (H, near 54 km depth), Lehmann (L, near 255 km depth), 410-km, 520-km, 660-km, and 900-km discontinuities. Notably absent is evidence for the Gutenburg discontinuity (lid/LVZ contrast), which is ubiquitously observed on paths with a significant oceanic or back-arc component [*Revenaugh and Jordan*, 1991c]. Table 4.1 presents t_v and R_Q (as given by *Revenaugh and Jordan* [1991b,c]) for the observed discontinuities. The residuals relative to starting model AU1 are quite small, since this model was constructed to roughly fit these data, and the data effectively define all the discontinuities required in our model. The discontinuity near 900-km depth is observed on only one other corridor analyzed by

Revenaugh and Jordan [1991c], that being a very short, arc-dominated path between New Britain and CTAO in the northeast corner of Australia. The fact that it occurs only for events from New Britain, and in particular is not observed on the other three paths that traverse Australia to NWAO, indicates that it is a localized to the New Britain region, and is not a characteristic of the top of the lower mantle beneath the Australia continent. We thus downweight this observation in the inversion process, and the discontinuity does not appear in subsequent models.

The whole mantle Q_{ScS} estimate is 243 ± 40 [*Revenaugh and Jordan*, 1991a]. As we expect there to be a significant Q contrast between the lid, LVZ and transition zone, and lower mantle [*Gudmundsson et al.*, 1994] , we set Q_{LM}=312 (the value for PREM), and we then partition the upper mantle Q into Q_{LID}=300 and Q_{TZ}=120. This partitioning integrates to the observed value of Q_{ScS} , and it is validated by forward modeling. These Q values are maintained throughout the analysis.

THREE-COMPONENT BODY- AND SURFACE WAVE DATA

We complement the *ScS*-reverberation data with frequency-dependent phase delays of surface, *SS*, and *S* waveforms extracted from 3-component, long-period seismograms of 22 earthquakes in the New Britain and New Guinea seismic zone recorded at GSN station NWAO (Figure 4.1 and Table 4.2). The source depths range from 10 to 233 km, and epicentral distance spans 37°-44°. The recorded seismograms are rotated into the tangential-radial-vertical coordinate system and low-passed with a zero-phase filter with a corner at 45 mHz. Full mode synthetic seismograms (complete to 50 mHz, filtered like the data) are calculated for each event using isotropic model AU1 and assuming Harvard CMT source parameters.

The Australia seismograms display several characteristics that distinguish them from the Pacific seismograms in Chapter 2. The surface waves are represented by relatively slow, dispersed wavetrains for both R_1 and G_1 (Figure 4.2), G_1 in particular

being notably different from the impulsive Love waves in Chapter 2 and 3. This is primarily due to the effect of a thick continental crust, which greatly slows down the higher frequencies relative to the lower frequencies (though it also slows the lower frequencies). This dispersion makes it difficult to directly observe the effects of anisotropy in the surface waves; in Figure 4.3a, the Rayleigh wave is fit somewhat better by AU1 than is the Love wave, but the magnitude of this difference is not clear from a simple visual comparison. The GSDF analysis quantifies this difference. One benefit of increased dispersion, however, is that it clearly separates the fundamental model Love waves from the *SS* phases within this distance range. Although it was not emphasized in Chapters 2 and 3, the shallow-focus Pacific events contribute no SS_H observations at distances less than 52°, due to Love wave interference; all the *SS* data came from intermediate and deep-focus events in that case. As Figure 4.3a demonstrates, such phases are clearly observed on seismograms sampling Australia. These phases are quite sensitive to anisotropic structure in the upper mantle, which results in splitting relative to an isotropic model that can be observed directly on the seismograms (Figure 4.3b). Because of the absence of deep focus earthquakes in New Guinea and New Britain, such data play a critical role in constraining the depth extent of anisotropic structure.

GSDF Analysis

The relatively clean separation of the surface and *SS* body waves, as well as the lack of deep-focus events, allows for a straightforward analysis of these data: much of the complexity and non-linearity discussed in Chapter 2 (for example Figures 2.5, 2.6, and 2.12) was caused by interference between G_1 and *SS* for shallow events, and between *SS*, *SSS*, and a variety of depth phases (*sS*, *sSS*, *sScS*) for intermediate- and deep-focus events. An example of the GSDF processing applied to a Love wave from a 36 km event is presented in Figure 4.4. The isolation filter is simply a sum of fundamental modes, and the cross-correlation and extraction of phase delays shows that AU1 approximately predicts the relative dispersion, but the model is much too slow. The partial derivatives

are quite different than those for oceanic Love waves, again due to the lack of interference with higher mode phases. They are sharply peaked for v_{SH} in the crust at 45 mHz, with a broader sensitivity to the upper 200 km at 15 mHz; the sensitivity to v_{SV} is minimal.

The process is depicted for a vertical-component *SS* phase in Figure 4.5. The isolation filter is formed by summing the eigenfunctions for all excited modes with group velocities of 4.33-4.53 km/s and phase velocities less than 8 km/s, excluding the fundamental modes; this process isolates the phase in time and eliminates contributions from core-interaction modes. The phase delays (Figure 4.5b) quantify the early arrival of the observed *SS* waveform as approximately 8 s, with approximately 3 s of dispersion (frequency dependence) relative to the synthetic model. The corresponding partial derivatives (Figure 4.5c) demonstrate the excellent sensitivity of these data to upper mantle structure. At low frequency, the *SS* phase averages the *SV* velocity in the upper 500 km. At higher frequency, the kernel peaks more sharply within the upper 300 km.

As shown by representative partial derivatives for each of these phase types (Figures 4.4, 4.5, and 4.6), the combination of surface-wave, reflected-body-wave, and direct-body-wave data provides good sensitivity to shear velocity structure throughout the upper 1000 km of the mantle. While the Rayleigh wave (Figure 4.6a) is confined to the upper 300 km of the mantle, the *SS* kernels (Figures 4.5c and 4.6b) sample the upper 600 km, increasing our sensitivity to anisotropic structure in the sublithospheric mantle beyond that provided by surface waves alone. The frequency-dependent variability of these kernels demonstrates the advantage of our broad-band analysis of these "body" waves relative to a more typical narrow-band analysis at a single center frequency [*Sheehan and Solomon*, 1991; *Woodward and Masters*, 1991]. The path-average, finite-frequency *S* wave (Figure 4.6c) also averages over much of the upper mantle and transition zone, with a peak near its ray-theoretical turning point at ~1000 km. As can be seen from Figure 4.6, the sensitivity of the observations to density, P and η structure is

much smaller than the shear sensitivity, but it is not negligible (with the exception of P and η kernels for tangential-component observations, which are zero), and we include these parameters in our inversion.

Figure 4.7 summarizes the GSDF data from all 22 events. These averages are for display only; our inversion includes the 797 individual observations from nearly 150 isolated waveforms. All data have been corrected for source anomalies, which are calculated from the average tangential and radial broad-band S-wave anomalies for each event. The large difference in the Love and Rayleigh wave residuals (20-30 s) relative to isotropic model AU1 is the LR discrepancy, and points to the presence of anisotropy in the upper mantle. Shear-wave splitting is observed in the SS phases, with the SS_H phases being advanced by up to 10 s. The S waves show little evidence of splitting or relative dispersion. Though the dispersive characteristics (relative to a starting model) of the Australia and Pacific data (Figure 2.8) are quite different, the magnitude of the LR discrepancy and SS splitting are quite similar; therefore, we might expect that the general magnitude of upper mantle anisotropy is similar between the two regions.

INVERSION

The inversion algorithm is identical to that described in Chapter 2. We invert the ScS-reverberation and turning-wave data set for perturbations to isotropic starting model AU1, using a set of Bayesian constraints [*Tarantola*, 1987]. Perturbations to depths to discontinuities and intercepts and linear gradients of the six radially anisotropic parameters within each of 7 upper mantle layers result in a total of 97 parameters. The data vector (797 frequency-dependent travel time residuals, 8 vertical travel time residuals, and 7 discontinuity impedance contrast residuals) and perturbation matrix elements are as described above and in the Appendix. The data are of similar quality to that observed in the Pacific, and the error estimates range from 2 s for a high-quality, high-frequency (40 mHz) observation to 10 sec for a low quality, low-frequency (10

mHz) observation. Error estimates for ScS reverberations are the same, with the exception of the 900-km discontinuity, which is given a large error value to effectively remove it from the inversion. We fully iterate the process, including recalculation of the travel time residuals and partial derivatives using synthetics and isolation filters for each new model. The results presented here represent two complete iterations.

The probability density function describing our prior state of knowledge of the model is very similar to that in Chapter 2. We specify minimal prior knowledge on the shear velocities through most of the upper mantle (a starting value with a large uncertainty of 0.5 km/s). This allows the data to constrain these parameters. The strong non-linearity associated with interfering arrivals from the low-velocity zone is not observed here, and thus the constraints that were required to stabilize this non-linearity in Chapter 2 are not needed here. We utilize nearly identical mineralogical constraints on density, bulk sound velocity, and η [*Ita and Stixrude*, 1993;*Nataf et al.*, 1986; *Montagner and Anderson*, 1989], with the only differences arising because of the different discontinuity structure. While the density across H is allowed to be discontinuous (~3% contrast, reflecting the spinel-to-garnet phase boundary inferred by *Revenaugh and Jordan* [1991c]), the density (and bulk sound velocity) across L are constrained to be first-order continuous, consistent with a mechanical (rather than phase or compositional) change across this boundary (see Chapter 5). A small density increase is again allowed at the 520-km discontinuity, due uncertainty in the expected density and velocity contrast across the β-phase to γ-spinel transition [*Revenaugh and Jordan,* 1991c; *Rigden et al.*, 1991; *Ita and Stixrude*, 1993]. The specification of a variety of prior distributions of anisotropy allow for the testing of a number of hypothesized models; these tests are discussed in the following sections.

We have estimated the posterior errors using a variety of guides: the formal error estimates; the variability of the model solution with different of combinations of data and parameter variances and prior constraints; and forward modeling of waveforms using the

resulting model. These estimates are qualitative, but they reflect the true errors much more accurately than the formal errors provided by the inversion alone. The parameters best-resolved by the data are the depths to discontinuities, the vertical shear impedance contrasts (i.e. a combination of v_{SV} and density), and the shear velocities; the *P* velocities, η, and density between discontinuities are also reasonably well-resolved through the inclusion of the mineral physics data. As is shown below, the our final model provides an excellent fit to the prior seismological and mineralogical constraints; in fact, we do not at all compromise our fit to the data by applying them, indicating that the mineralogical and seismological data are entirely self-consistent.

MODEL AU3

Our preferred model AU3 for the western Australia corridor from New Guinea to NWAO is presented in Figure 4.9 and Table 4.3. AU3's upper mantle is characterized by an anisotropic, moderate-velocity uppermost lithosphere above the H discontinuity at 54 ± 5 km depth; a fast (v_{SH}=4.69 ± 0.02 km/s), thick, anisotropic lithosphere, bounded at 252 ± 5 km depth by the L discontinuity; v_{SV} in the lid of 4.65 ± 0.02 km/s; and high isotropic v_S (4.63 ± 0.03 km/s) just below L, with a very flat gradient leading to the 410-km discontinuity. The transition zone discontinuities are located at 406 ± 3 km, 499 ± 10 km, and 659 ± 4 km. The shear anisotropy is 3.3 ± 0.5% in the lithosphere, terminating at L with a decrease in v_{SH} and an increase in v_{SV}; the mean isotropic velocity profile is piece-wise continuous across this boundary. The accompanying *P* anisotropy is 3.7 ± 1.5%, although this value relatively poorly constrained by our data. The final density and bulk sound velocity profiles generally satisfy the bulk sound velocity constraints (Figure 4.8).

The fit to our data is summarized in Figure 4.7 and Table 4.1; over 80% of the variance observed relative to AU1 is explained by AU3. The *SH-SV* differences observed in the surface wave and *SS* phase delays have been eliminated, and the *ScS*-reverberation

data is now largely satisfied. Except for the omission of the 900-km discontinuity, AU3 provides a good fit to the *ScS*-reverberation data. The impedance contrast across the Moho must be larger than the *ScS* data indicate in order to maintain reasonable crustal velocity and density values. Also, we can achieve a better fit to the *S* waves by allowing a slightly larger impedance contrast across the 660-km discontinuity. Revenaugh and Jordan's observed impedance contrast at 660-km along this corridor is the lowest observed in the Australasian region, matched only by the path from New Britain to CTAO. As with the 900-km discontinuity, the small 660-km discontinuity may be related to anomalous near-source structure. The magnitude of the 660-km discontinuity in AU3 is similar to the average for the entire region, although it is still somewhat small compared to other paths traversing western Australia.

A simple qualitative evaluation of AU3 can be made by visual comparison of data and synthetic waveforms. Figure 4.10 presents a suite of observed seismograms that characterize our data set, along with full mode-synthetic seismograms calculated for AU3. All phase types are represented, including *S*, *SS*, *R1*, and *G1*. While there is obvious variability and misfit in some cases, the overall fit to this complex suite of waveforms is quite good.

DEPTH EXTENT OF ANISOTROPY: ALTERNATIVE MODELS

AU3 does not uniquely fit our data; there are a large number of similar models that fit the observations equally well, and the error estimates on the depths and velocities attempt to account for this non-uniqueness. The general form of AU3 appears to be well-determined, however; in particular, we have explicitly tested the general magnitude and distribution of anisotropy by systematically forcing the anisotropy into restricted depth intervals, and we find that acceptable models do not deviate substantially from that presented in Figure 4.9.

We first require the model to be isotropic everywhere except between the M and H discontinuities; this model is only a slight improvement over isotropy, and neither the *LR* discrepancy nor the *SS* splitting can be satisfied across the frequency band, even with very large (>5%) amounts of anisotropy. If we then allow anisotropy to extend from M to L, the result is AU3, and the data are well satisfied. The data can also be fit if anisotropy is restricted to the layer between H and L (i.e. M to H is isotropic), but since there is no known reason for the spinel-to-garnet transition at H to affect anisotropy we do not to force this region to be isotropic.

The behavior of the anisotropic structure near the L discontinuity is an important issue to address, as *Revenaugh and Jordan* [1991c] have proposed that this boundary arises due to a transition from anisotropic to isotropic structure. By applying a variety of prior constraints on the distribution of anisotropy near L, we find that a relatively rapid reduction, if not termination, of anisotropy appears to be required by our data. The hypothesis that anisotropy smoothly terminates at or above L (similar to PREM; Figure 4.11) is rejected, as such a model does not fit the data. If we hypothesize that anisotropy is required to extend across L and down towards the 410-km discontinuity, we find that the magnitude of the *SS* splitting only allows for a small amount, less than 1%, and no improvement in data fit is provided by this allowance (i.e. less than 1% anisotropy in this depth range is below the resolution of our data). Acceptable models are not exactly like AU3; for instance, the equal-but-opposite discontinuities in v_{SH} and v_{SV} at L (resulting in nearly continuous mean velocities across the boundary) is not explicitly required by our data, and alternative models without a v_{SH} discontinuity also fit the data. The hypothesis that such a balance is acceptable cannot be rejected, however, because enforcing it results in no additional misfit. AU3 is thus consistent with L being entirely due to a change in anisotropic structure, with no resolvable change in mean shear or compressional velocities or density across the discontinuity. We discuss the implications of this result in more detail in Chapter 5.

An important caveat is that this analysis is restricted to our linear model parameterization. It is possible that anisotropic structure is independent of the discontinuity structure, and anisotropy may terminate, for example, near 200 km depth. To test for such bias, we have inverted for models in which the anisotropy is forced to terminate at depths of 150 km and 200 km, respectively. Models in which this termination is required to be smooth do not fit the data; this is not surprising, since even a smooth termination at L (250 km) does not fit the data. A discontinuous termination near 150 km also produces an unsatisfactory fit to the data. A model with a relatively discontinuous termination of anisotropy near 200 km appears to fit the data as well as AU3; such a discontinuity is larger than L, however, and given the added unnecessary complexity of such a model, we prefer AU3. These tests are not perfect given that they maintain the layered parameterization, but they imply that our data require ~3% anisotropy above a depth of 200 to 250 km with relative isotropy below this depth.

Upper-Mantle and Transition-Zone Structure

It is instructive to compare our regional anisotropic model with a 1-D path-average projection of the global 3-D model S12_WM13 [*Su et al.*, 1994] along the New Britain-to-NWAO path ("S12AU"; Figure 4.11). As in most shield regions, S12_WM13 is substantially faster than PREM throughout the Australian upper mantle, evidence of a deep seismic keel beneath the continent. This inference can also be made from AU3, although the comparison with PREM is of questionable meaning because of the global-average nature of this model; comparisons with the PA5 structure (deferred to Chapter 5) are much more conclusive. When examined in this radial fashion, S12_WM13 retains the low-velocity zone of PREM, even in a shield region such as this one. A simple visual comparison of examples of our data with seismograms calculated for AU3 and S12_WM13 indicates that the AU3 synthetics match the data better, even below 15 mHz (Figure 4.12). This is probably due to the inability of long-period data incorporated in

global parameterizations to isolate structure at the scale of the western Australia craton. (We note that S12_WM13 is constructed to fit data with frequencies less than 30 mHz, and therefore should not necessarily be expected to match data above this frequency.)

High velocities extending to greater than 200 km depth with minimal or no LVZ are consistent with shear velocity models from Australia and other stable continental regions inferred from a variety of data types (Figure 4.13). Peak SH velocities (4.70 km/s) are somewhat lower than those observed in North America using *SH* body waves (4.77 km/s in SNA [*Grand and Helmberger*, 1984b]); this may be a regional difference, but it may also be due to Grand and Helmberger's isotropic modelling of SS_H body waves, which are sensitive to both v_{SV} and v_{SH} in the shallowest portion of the mantle (see Figure 4.6b). The SV velocity is nearly identical to that found in Eurasia from long-period Rayleigh waves [EU2; *Lerner-Lam and Jordan*, 1987]. NJPB is a recent model for the northern margin of Australia, generated by jointly modeling S_H and S_V refraction profiles [*Kennett et al.*, 1994]; it is quite similar to the mean value of the anisotropic lithosphere in AU3. Interestingly, a model for western Australia derived from high-frequency *Sn* observations [SOZ; *Bowman and Kennett*, 1993] is very consistent with v_{SH} in our model. Such phases (observed on vertical-component seismograms) might be expected to be reflective of v_{SV}. As discussed in Chapter 5, however, we believe that high-frequency *Sn* is forward-scattered through heterogeneous anisotropic structure, scrambling polarizations and resulting in first arrivals consistent with the fast (v_{SH}) velocity, rather than v_{SV}. Observations of long-duration, high-velocity, high-frequency *Pn* from the Eurasian shield have been similarly interpreted [*Ryberg et al.*, 1995].

In contrast to the steep velocity gradient between 200-400 km in oceanic upper mantle, AU3 and other shield regions appear to be characterized by remarkably flat shear-velocity gradients in this depth interval (Figure 4.13). The velocities in this depth range are well-resolved by our data, and they are similar to those observed in North America (SNA), Eurasia (EU2), and northern Australia (NJPB).

The combination of *ScS*-reverberation data with *SS* travel times makes AU3 an excellent model for examining the average transition zone structure beneath western Australia. The location of the "410" is at 406 ± 3 km depth. This is identical to that in SNA and NJPB, and slightly deeper to that in EU2 (Figure 4.13). It is shallow relative to the average values reported for the entire southwest Pacific and Australia region (414 ± 2 km; *Revenaugh and Jordan* [1991b]), and it is much shallower than the value found in PA5 (Chapter 3). The magnitude of this discontinuity is 5.5% in shear velocity, slightly larger than other regional and global models; this results in a slightly shallower gradient below the 410-km discontinuity.

AU3 includes a 520-km discontinuity located at 499 ± 10 km, with an impedance contrast of 0.8% that is split equally between shear velocity and density. As discussed in Chapter 2, the *SS* data provide good constraints on the average velocity structure of the transition zone, but they cannot resolve a 520-km discontinuity due to their relatively long wavelengths. Short-period *P* wave profiles from the northern margin of Australia [*Cummins et al.*, 1992] show no evidence of a large, sharp 520, but they cannot rule out a discontinuity spread out over 30-50 km, especially if it is quite small or distributed more substantially in density than velocity, as suggested by mineral physics data [*Rigden et al.*, 1991]. Given the uncertainties in the mineral physics observations and the limited bandwidth and/or geographic distribution in the seismological observations, we maintain a discontinuity that fits our *ScS*-reverberation observation with a discontinuity in both velocity and density.

The gradient between 499 km and the 660-km discontinuity is similar to SNA, NJPB, and EU2 (Figure 4.13), and the average velocity in this depth range beneath Australia is slightly higher than beneath North America or Eurasia.

SUMMARY

Model AU3 represents the significant result of this chapter -- a simply-parameterized seismic model that describes the radially anisotropic structure of the upper mantle in a stable continental region. While AU3 holds several implications for the anisotropic structure of continental tectosphere, we present a detailed discussion of these issues in Chapter 5.

AU3 is constructed via self-consistent analysis of 797 frequency-dependent travel times from three-component recordings of *R1*, *G1*, *SS*, and *S* waveforms along with *ScS*-reverberation data from western Australia. Distributions of density and bulk sound velocity expected for mineralogical models of the upper mantle are used to further constrain the model in a realistic manner. We successfully invert these data for one-dimensional, path-average, radially anisotropic models of the upper mantle beneath western Australia, specifically testing hypotheses on the depth distribution of the anisotropic structure.

We find that anisotropy must be present throughout the thick, high-velocity continental lithosphere to a depth of approximately 250 km, where it terminates at the L discontinuity. The magnitude of the radial anisotropy is approximately 3% in v_S and 4% in v_P, similar to the magnitude found in the western Pacific. High velocities with relatively low radial gradients extend to the 410-km discontinuity. The depths of the 410-km and 660-km discontinuities are 406 km and 659 km, respectively. The model is in excellent agreement with upper mantle models from other stable continental regions, and it is consistent with mineralogical data for either pyrolite or high-aluminum piclogite.

Table 4.1. ScS Reverberation Data, New Britain to NWAO

Discontinuity	Observed		AU3 Prediction		AU1 Prediction	
	t_v	R_O	t_v	R_O	t_v	R_O
Moho	7.5	0.120	8.3	0.156	7.7	0.073
H	13.9	0.049	13.9	0.047	14.1	0.044
L	57.5	0.021	57.5	0.015	57.7	0.021
"410"	90.1	0.044	90.1	0.042	90.3	0.043
"520"	109.4	0.008	108.4	0.008	109.6	0.008
"660"	138.0	0.041	138.0	0.057	138.2	0.040
"900"	171.5	0.019	----	----	171.7	0.018
CMB	468.1	----	468.5	----	470.3	----

t_v represents one-way travel time in seconds; R_O is the shear wave impedance contrast. Observations extracted from *Revenaugh and Jordan* [1991a,c].

Table 4.2. New Guinea/New Britain Seismic Sources

Date	Harvard CMT Location				Station	Delta
	Origin Time UT	Latitude °N	Longitude °E	Depth km		°
1987 05 06	12:40:01.1	-5.78	152.83	15.	NWAO	42.73
1981 10 04	00:01:30.6	-4.55	146.37	20.	NWAO	39.20
1980 06 18	09:18:48.4	-5.23	152.16	25.	NWAO	42.63
1985 07 17	08:09:34.7	-4.48	152.68	25.	NWAO	43.52
1986 09 11	00:18:29.2	-5.33	152.58	25.	NWAO	42.86
1983 12 22	01:02:11.3	-5.51	152.09	34.	NWAO	42.37
1983 12 21	23:32:15.4	-5.79	152.14	36.	NWAO	42.23
1986 10 24	02:58:52.4	-5.95	153.77	40.	NWAO	43.29
1982 06 09	03:08:37.7	-5.86	150.90	44.	NWAO	41.30
1987 10 16	20:48:17.9	-6.22	149.44	48.	NWAO	40.03
1984 07 05	05:21:59.9	-6.10	154.08	50.	NWAO	43.41
1985 12 30	11:13:18.3	-5.82	150.64	77.	NWAO	41.15
1980 06 04	09:31:56.6	-5.45	151.11	91.	NWAO	41.74
1983 05 10	11:02:40.1	-5.42	150.94	101.	NWAO	41.64
1986 03 07	02:46:58.4	-5.19	151.91	101.	NWAO	42.48
1982 08 14	14:27:46.5	-5.12	143.73	114.	NWAO	37.09
1986 10 23	03:54:27.1	-6.21	146.11	118.	NWAO	37.78
1987 11 25	16:08:40.6	-5.61	149.46	142.	NWAO	40.47
1987 12 04	19:51:41.7	-5.85	154.42	155.	NWAO	43.83
1984 05 30	07:49:55.1	-5.02	151.64	157.	NWAO	42.41
1984 04 13	22:05:14.6	-5.69	148.44	170.	NWAO	39.72
1981 03 21	22:52:45.1	-5.48	146.88	233.	NWAO	38.83

Table 4.3. Model AU3

Depth, km	v_{PH}, km/s	v_{PV}, km/s	v_{SH}, km/s	v_{SV} km/s	ρ, g/cm^3	η
0	6.05	6.05	3.62	3.62	2.85	1.00
30	6.05	6.05	3.62	3.62	2.85	1.00
30	8.15	8.00	4.40	4.28	3.30	0.90
54	8.15	8.00	4.40	4.28	3.30	0.90
54	8.52	8.23	4.68	4.56	3.40	0.90
252	8.61	8.28	4.70	4.52	3.44	0.90
252	8.45	8.45	4.63	4.63	3.45	1.00
406	8.88	8.88	4.80	4.80	3.58	1.00
406	9.31	9.31	5.07	5.07	3.69	1.00
499	9.64	9.64	5.19	5.19	3.85	1.00
499	9.67	9.67	5.23	5.23	3.88	1.00
659	10.21	10.21	5.58	5.58	4.00	1.00
659	10.72	10.72	5.94	5.94	4.21	1.00
861	11.21	11.21	6.28	6.28	4.50	1.00

Model is identical to PREM through the remainder of the lower mantle and core.

FIGURE CAPTIONS

Fig. 4.1. Mercator projection of the western Australia corridor sampled by our data. The propagation path (long-dash line) from 22 New Britain and New Guinea earthquakes to NWAO is represented by model AU3. Also shown is the Banda Sea-to-CAN path (short-dash line) used to test for azimuthal variations in Chapter 5.

Fig. 4.2. (Left) Observed reflectivity profile and its interpretation obtained for the western Australia corridor. The profile and its interpretation both display vertical-incidence shear reflectivity (R_o), in percent. Apparent depths in interpretation were computed using the aspherical M84C velocity structure of *Woodhouse and Dziewonski* [1984]; these depths are refined in the model presented in this paper. (Right) Seismic Q structure for the western Australia path. (a) Average Q_{ScS} from multiple-*ScS* observations. (b) Q structure assumed for the modeling in this paper. Q_{LM} is taken from PREM, and Q_{UM} is partitioned into lid and transition zone values. The vertical average Q in (a) is maintained in (b).

Fig. 4.3. Direct observational evidence of anisotropy in long-period seismograms. (a) Data from an intermediate-focus (101 km depth) event. Top pair of traces are vertical-component data and full synthetic seismogram for isotropic model AU1, with the *S* wave arriving at ~14 min, *SS* at ~17 min, and R_1 at ~20 min. The bottom pair of traces are tangential-component observation and synthetic seismogram for AU1, with the *S* at ~14 min, *SS* at ~17 min, and G_1 at ~18 min. Although the predicted group arrival of the Rayleigh and Love waves appear early and late, respective, it is difficult to estimate by eye the relative misfit of these phases. (b) Zoom on the *SS* phases from the same event. While the *SS* synthetic provides a good fit to the data, the LPT *SS* arrival is faster than AU1 (and the vertical-component *SS* observation) by 5-10 s. *SH-SV* differences in phases

such as this one place good constraints on anisotropy in the deeper upper mantle and the transition zone. Mode-summation synthetic seismograms are complete to 50 mHz, filtered like the data, and convolved with Harvard CMT source mechanisms.

Fig. 4.4. Example of the GSDF processing for a Love wave from a shallow-focus (35 km depth) event. a) Observed (top), full synthetic (middle), and isolation filter (bottom) seismograms; the *S* wave arrives at ~14.5 min, *SS* at 17.5 min, and G_1 at ~20 min. The isolation filter is constructed by summing only the fundamental mode branch. b) Phase delays $\delta\tau_p$ as a function of frequency, relative to the starting model. AU1 is much too slow for the observed Love waves across the frequency band. c) Three sets of partial derivative kernels as a function of depth; the kernels relative to the two shear velocities for 15, 30, and 45 mHz are shown for this example. While the low-frequency observation (15 mHz) is sensitive to v_{SH} in the upper 200 km, the higher-frequency observations become increasingly sensitive to structure in uppermost mantle and crust.

Fig. 4.5. Example of the GSDF processing for vertical-component *SS* from an intermediate-focus event (170 km depth) a) Observed (top), full synthetic (middle), and isolation filter (bottom) seismograms . Observed phases are *S* (14 min), *SS* (16 min), and R_1 (19 min). The isolation filter or *SS* is constructed by summing mantle modes with group velocities of 4.43 ± 0.1 km/s. b) Phase delays $\delta\tau_p$ as a function of frequency, relative to the starting model. The ~4 s frequency-dependent variation indicates the relative dispersion observed in these "body" waves, and illustrates the value of using a broad-band approach to processing the data. This data is fast at all frequencies. c) Three sets of partial derivative kernels as a function of depth; the kernels relative to the two shear velocities for 15, 30, and 45 mHz are shown for this example. While the low-frequency observation (15 mHz) is sensitive to v_{SV} in the upper 400 km, the higher-frequency observations become increasingly sensitive to the upper 300 km of the mantle.

Fig. 4.6. Partial derivative kernels for examples of different phase types. a) Rayleigh wave kernels. b) Tangential-component *SS* kernels. c) Tangential-component *S* kernels. For each phase, two frames are shown: low frequency (15 mHz) on the left, high frequency (40 mHz) on the right. Within each frame, 3 pairs of kernels are shown: shear kernels on the left, compressional kernels in the middle, and η and density kernels on the right. Relative scales are maintained for each phase, with a scale provide on the far right in units of s km^{-3} $unit^{-1}$ perturbation. η is also scaled by a factor of 4000 to facilitate plotting with density.

Fig. 4.7. Summary of the frequency-dependent travel time data. Phase delays are categorized by phase type (Surface wave, *SS*, or *S*), and then separated into tangential (*SH*) or radial/vertical (*SV*) observations, and averaged in each frequency band. Symbols represent the residuals relative to AU1, while the lines represent the predicted fit of model AU3 to these data. Dispersion relative to AU1 is indicated by a frequency-dependent trend, while evidence of anisotropy can be observed as a separation of the *SH* and *SV* observations for a given phase type. a) Love and Rayleigh waves. b) *SS* waves. c) *S* waves. Error bars are determined by a weighted average of estimated *a priori* errors.

Figure 4.8. Values of density ρ and bulk sound velocity v_ϕ calculated by *Ita and Stixrude* [1992] for the pyrolite model (*circles*); error bars represent arbitrary ±1% errors for the calculated profiles. These were used to construct prior distributions for ρ and v_ϕ that was used in the inversion. The values calculated from resulting model AU3 (*solid lines)* are shown for comparison. Neither the density nor the bulk sound velocity constraints are critically dependent on the choice of pyrolite for a model composition; the general

behavior of both density and bulk sound velocity is similar for high-aluminum piclogite, for example.

Fig. 4.9. Model PA5. From left to right, η, density, shear velocities, and compressional velocities are plotted as a function of depth. The model is radially anisotropic through the upper 250 km, with v_{SH} and v_{PH} being higher than v_{SV} and v_{PV}, respectively. Below 860 km depth, the model is the same as PREM.

Fig. 4.10. Comparisons between observed and synthetic seismograms from 4 representative events. Each event includes both tangential- (LPT) and vertical- (LPZ) component seismograms; for each event pair, the top trace is the data, the bottom trace is the seismogram (complete to 50 mHz) for final model AU3. The traces are aligned (at 0 min) on the *S* wave, with the synthetic seismograms further corrected for an event static. Both data and synthetic are low-passed with a 45 mHz corner.

Fig. 4.11. Shear velocities for model AU3, a path-average approximation of S12_WM13 appropriate for the New Britain to NWAO path (labeled "S12AU"), and PREM. For each model, the higher lid/LVZ velocity is v_{SH}, the lower velocity is v_{SV}. S12AU is calculated by determining the average S12_WM13 perturbation to PREM as a function of depth over the path from New Britain to NWAO, and applying it to both v_{SH} and v_{SV}. Comparison between AU3, S12AU, and PREM indicates that while S12_WM13 reflects the high-velocity Australian upper mantle relative to PREM, it is still too slow in the lower lithosphere along this path.

Fig. 4.12. Observed and synthetic seismograms for models PA5 and S12_WM13, for the same event presented in Figure 4.3. The *S* wave arrives at 14 min, *SS* at 17 min, G_1 at ~19 min, and R_1 at ~20 min. Vertical component seismograms are on top, and tangential

component seismograms are on the bottom. Synthetics are aligned on the *S* wave to remove the source static, and the S12_WM13 seismograms are calculated using the spherical harmonic coefficients and the asymptotic perturbation scheme of *Woodhouse and Dziewonski* [1984]. a) Seismograms low-pass filtered with a corner at 15 mHz; b) Seismograms low-pass filtered with a corner at 35 mHz. In both frequency bands, AU3 fits the data much better than S12_WM13.

Fig. 4.13. Comparison of AU3 to other upper mantle shear velocity models from stable continental regions. EU2 [*Lerner-Lam and Jordan*, 1987] is a Eurasian model designed to fit Rayleigh waves, and it compares to the *SV* (lower) AU3 velocity quite well. SNA [*Grand and Helmberger*, 1984b] is an *SH* model for the Atlantic, and thus compares to v_{SH} in AU3. The differences in lid thickness and velocity may reflect regional variations in shield structure in different regions. NJPB [*Kennett et al.*, 1994] is constructed to fit broad-band S_H and S_V refraction profiles from northern Australia, and matches the average isotropic velocity of AU3 quite well. SOZ [*Bowman and Kennett*, 1993] is a model derived from high-frequency *Sn* observations from western Australia, and only extends to 210 km depth. Note the good agreement between AU3, EU2, SNA, and NJPB on the gradient between 250-410 km. This shallow gradient differs markedly from that observed in oceanic regions (Figure 2.16), and it appears to be a robust feature of stable continental upper mantle.

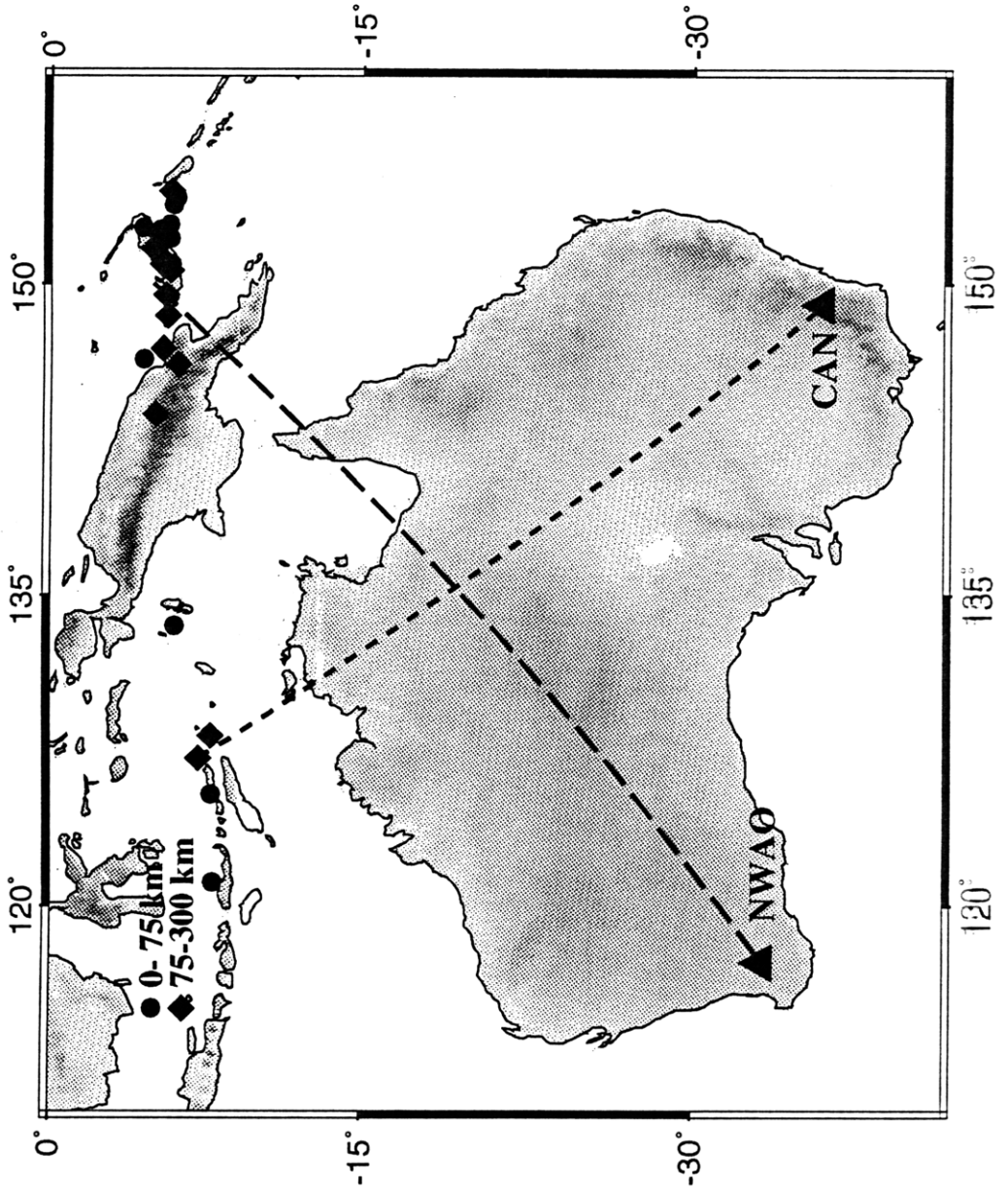

Figure 4.1

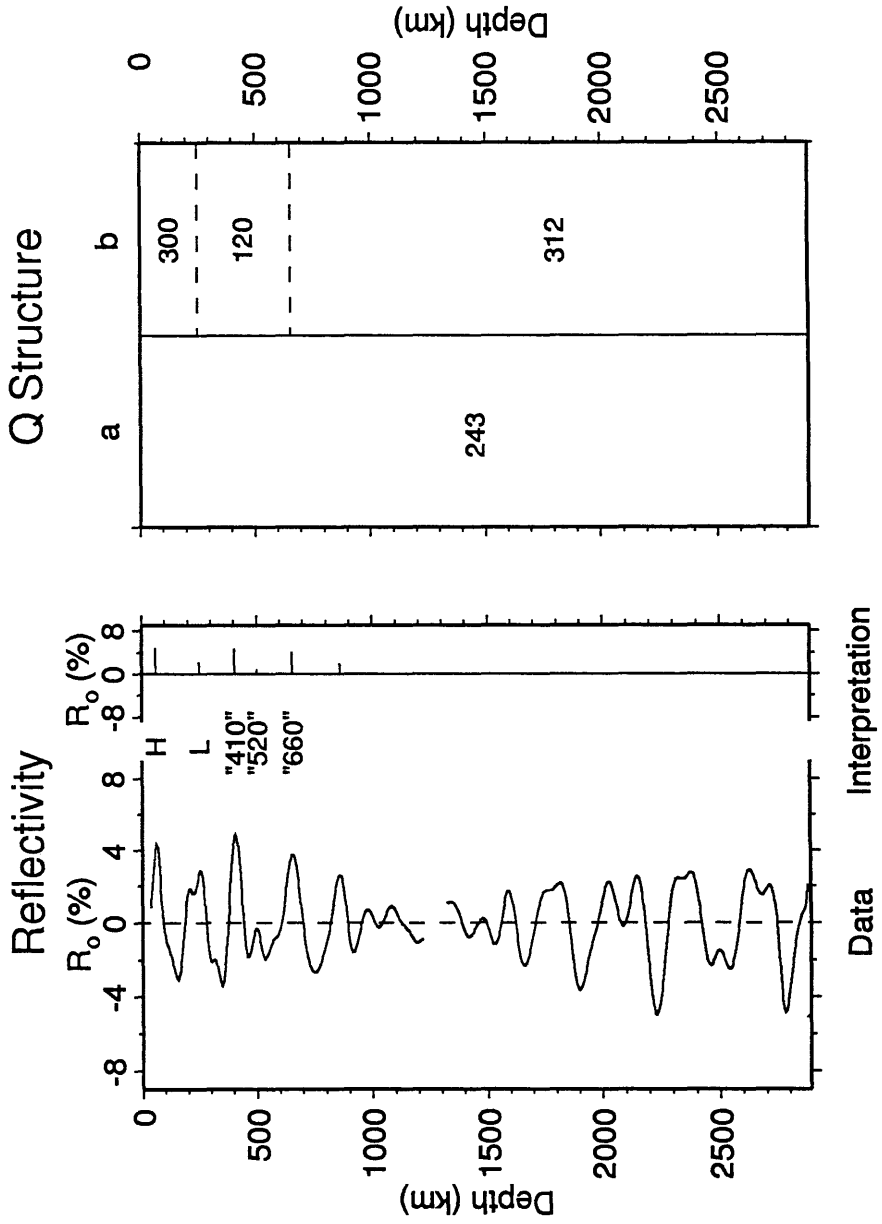
Q Structure
a
b
243
300
120
312
Depth (km)
0
500
1000
1500
2000
2500
Reflectivity
R_o (%)
-8
-4
0
4
8
H
L
"410"
"520"
"660"
Data
Interpretation

Figure 4.2

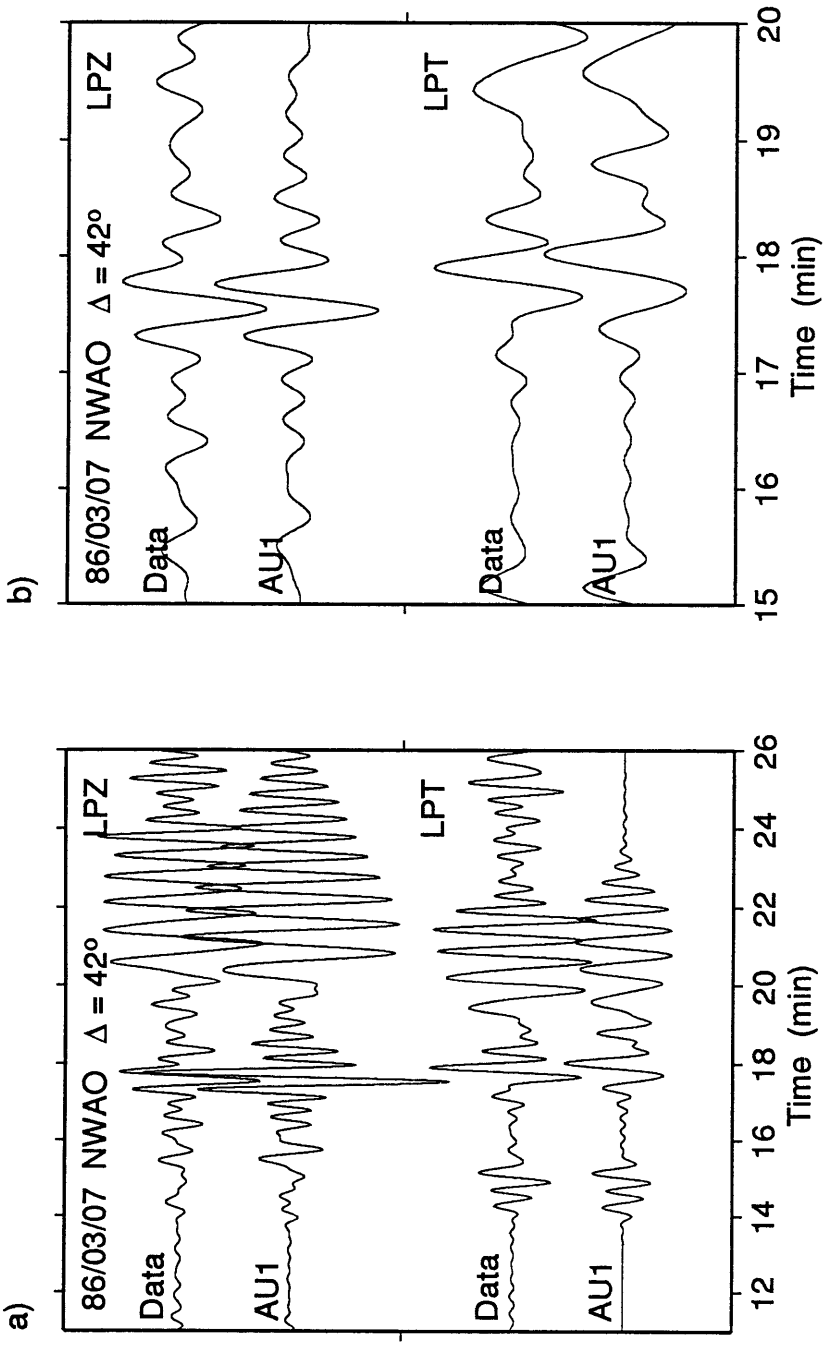
a)
86/03/07 NWAO Δ = 42°
LPZ
Data
AU1
LPT
Data
AU1
12 14 16 18 20 22 24 26
Time (min)
b)
86/03/07 NWAO Δ = 42°
LPZ
Data
AU1
LPT
Data
AU1
15 16 17 18 19 20
Time (min)

Figure 4.3

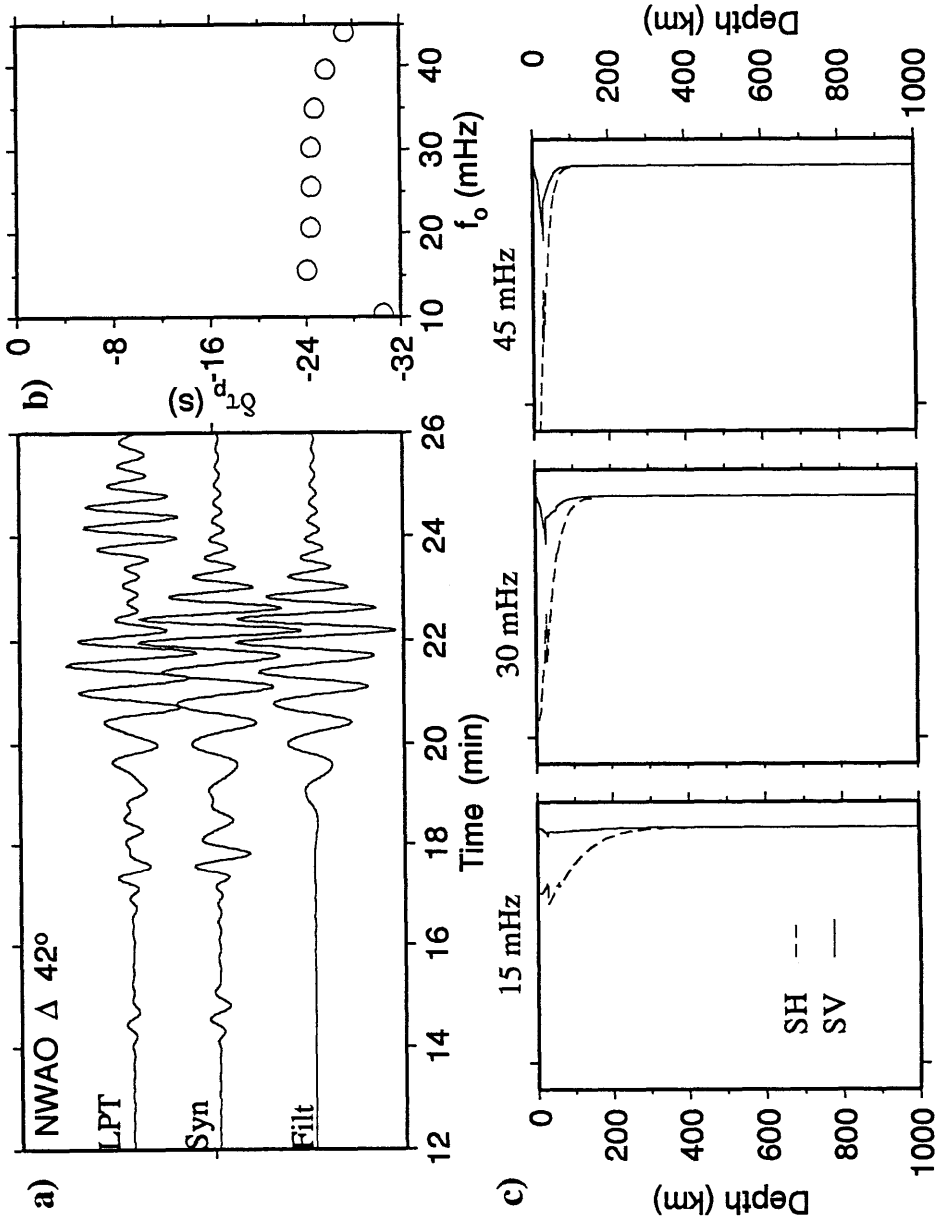
a)
NWAO Δ 42°
LPT
Syn
Filt
Time (min)
b)
$\delta\tau_p$ (s)
f_o (mHz)
c)
15 mHz
30 mHz
45 mHz
SH
SV
Depth (km)

Figure 4.4

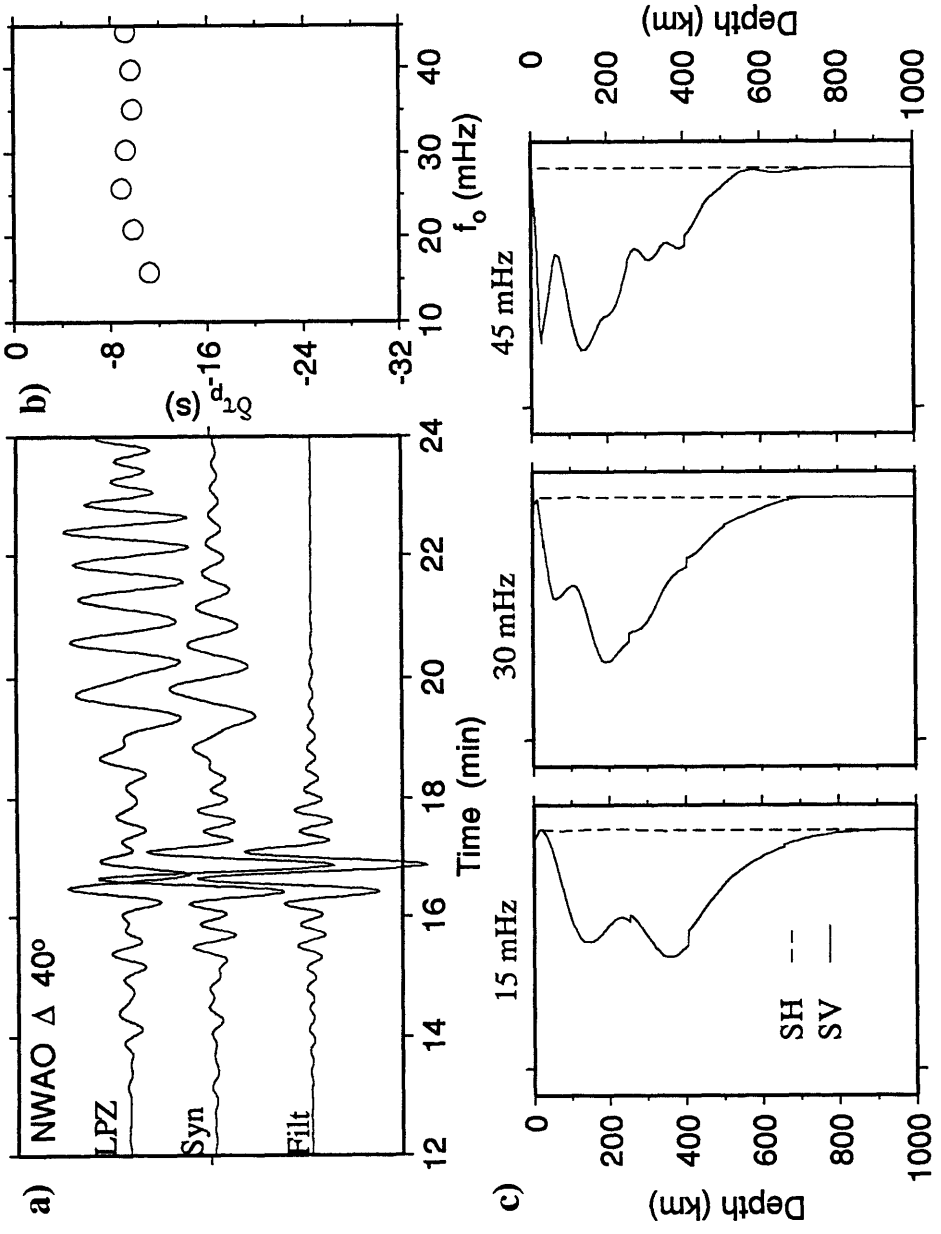
a)
NWAO Δ 40°
LPZ
Syn
Filt
Time (min)
b)
δτ_R (s)
f_o (mHz)
c)
15 mHz
30 mHz
45 mHz
SH
SV
Depth (km)

Figure 4.5

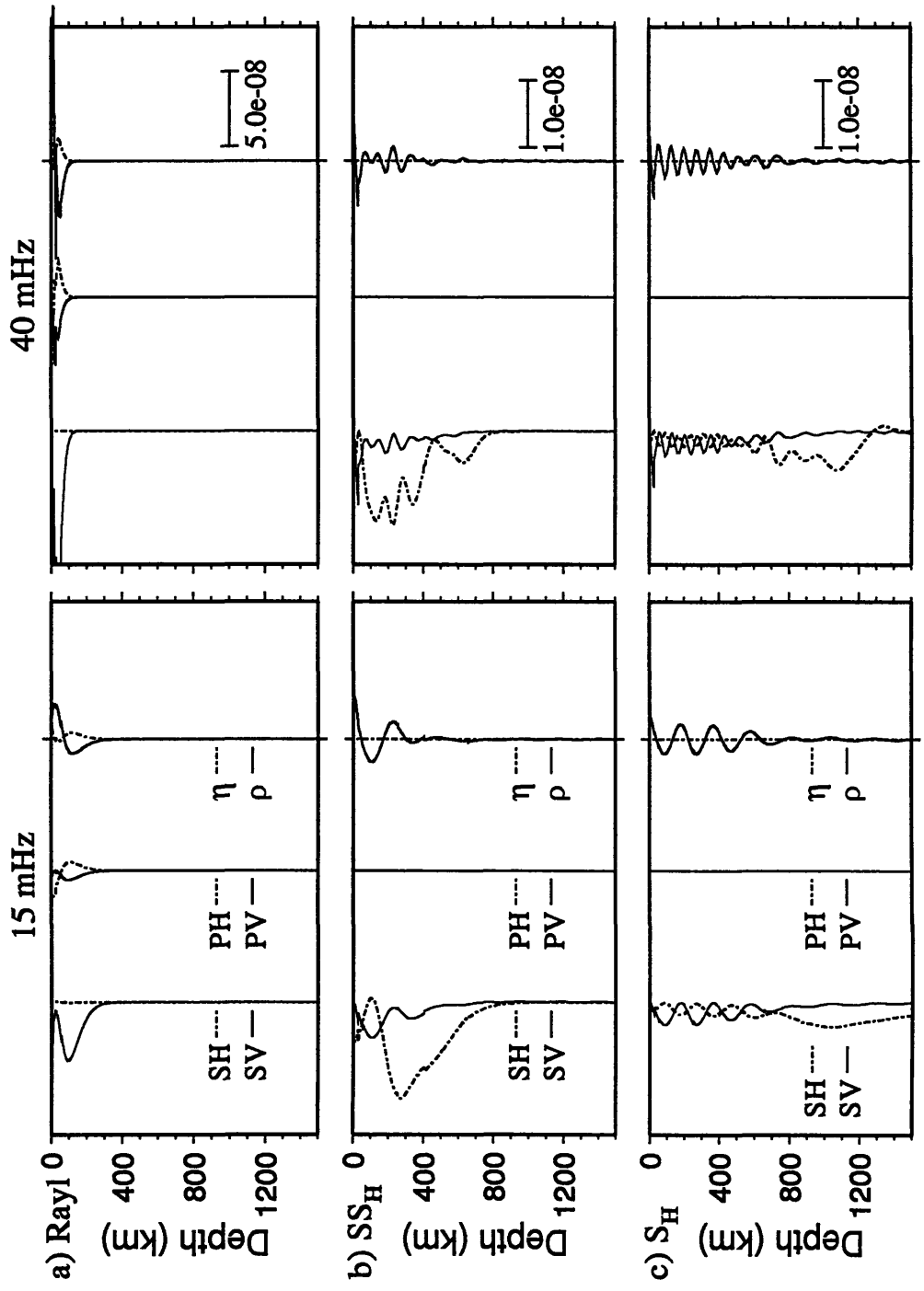
40 mHz
15 mHz
5.0e-08
1.0e-08
1.0e-08
SH
SV
PH
PV
η
ρ
a) Rayl
b) SS$_H$
c) S$_H$
Depth (km)
0
400
800
1200

Figure 4.6

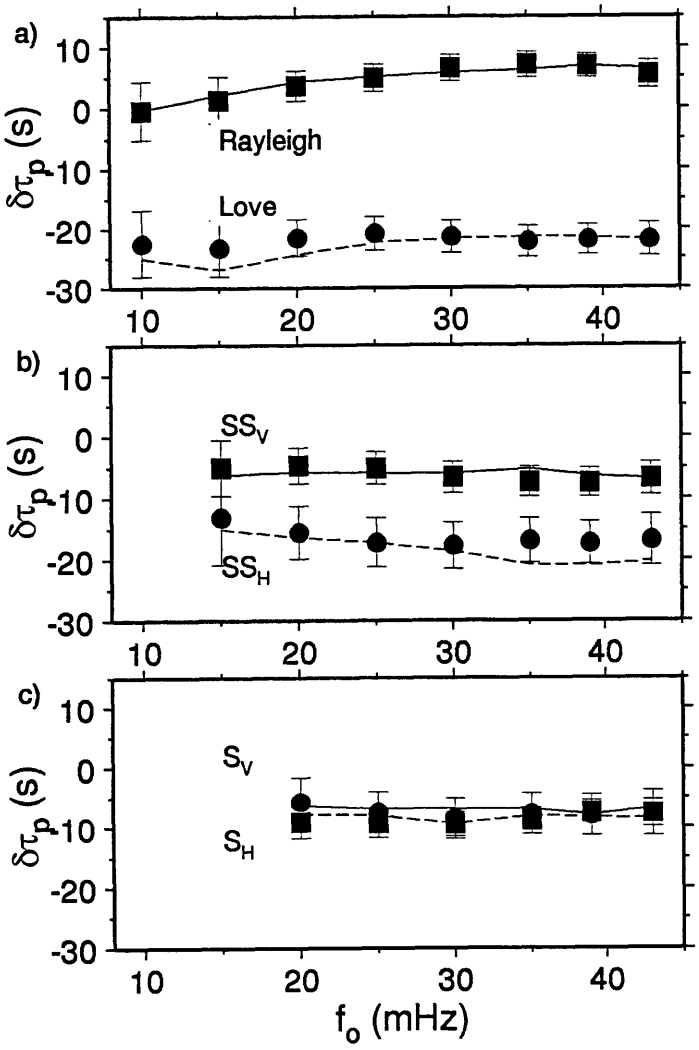
a)
b)
c)
Rayleigh
Love
SS$_V$
SS$_H$
S$_V$
S$_H$
$\delta\tau_p$ (s)
10
0
-10
-20
-30
10
20
30
40
f$_o$ (mHz)

Figure 4.7

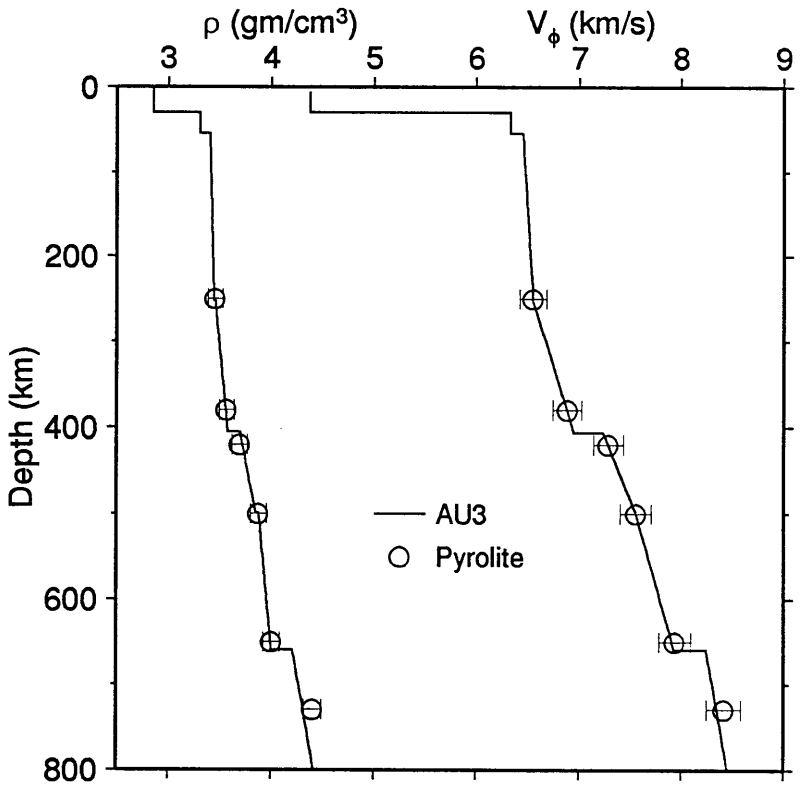
ρ (gm/cm³)
V$_\phi$ (km/s)
3
4
5
6
7
8
9
0
200
400
600
800
Depth (km)
AU3
Pyrolite

Figure 4.8

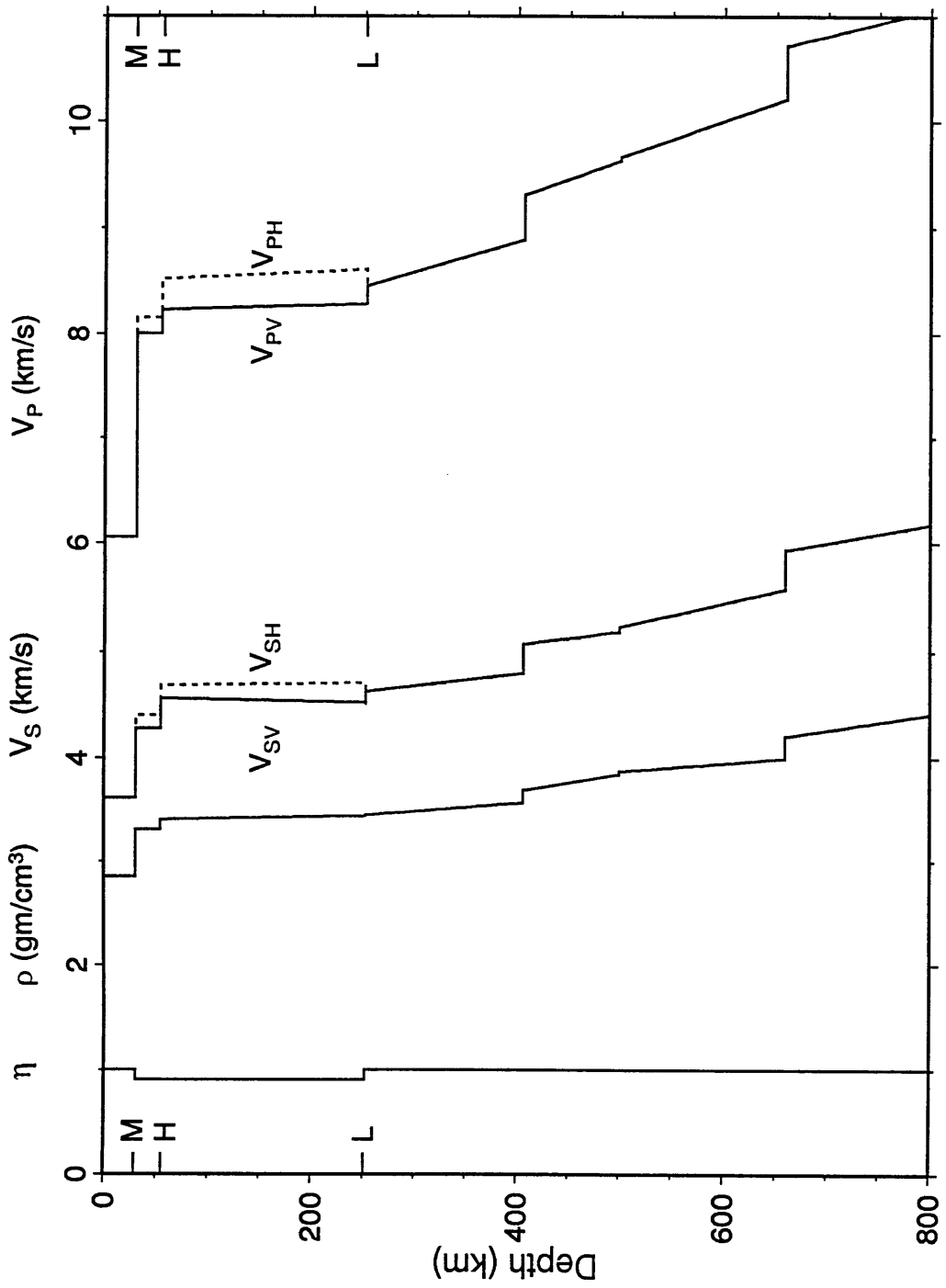
M
H
L
V_{PH}
V_{PV}
V_{SH}
V_{SV}
η
ρ (gm/cm³)
V_S (km/s)
V_P (km/s)
Depth (km)
0
2
4
6
8
10
0
200
400
600
800

Figure 4.9

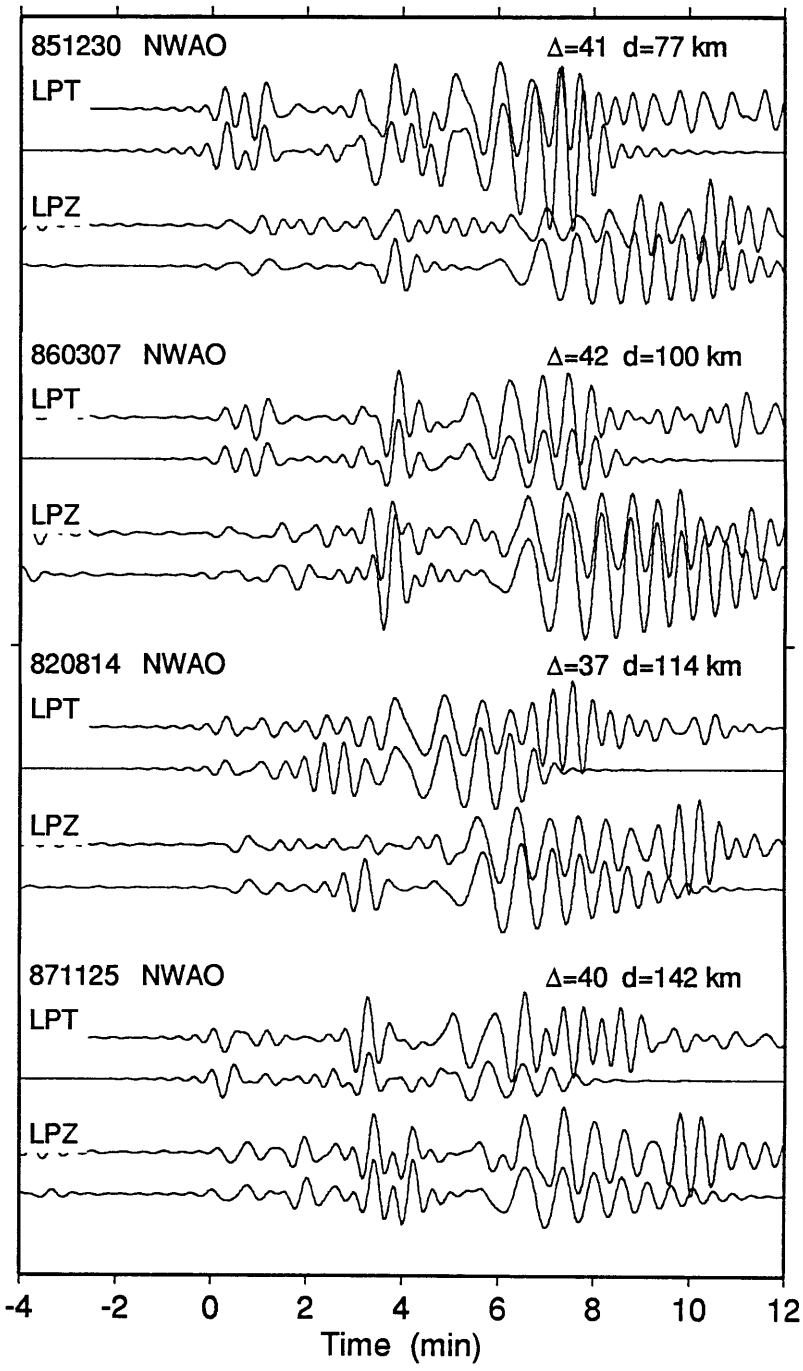
851230 NWAO
Δ=41 d=77 km
LPT
LPZ
860307 NWAO
Δ=42 d=100 km
LPT
LPZ
820814 NWAO
Δ=37 d=114 km
LPT
LPZ
871125 NWAO
Δ=40 d=142 km
LPT
LPZ
-4
-2
0
2
4
6
8
10
12
Time (min)

Figure 4.10

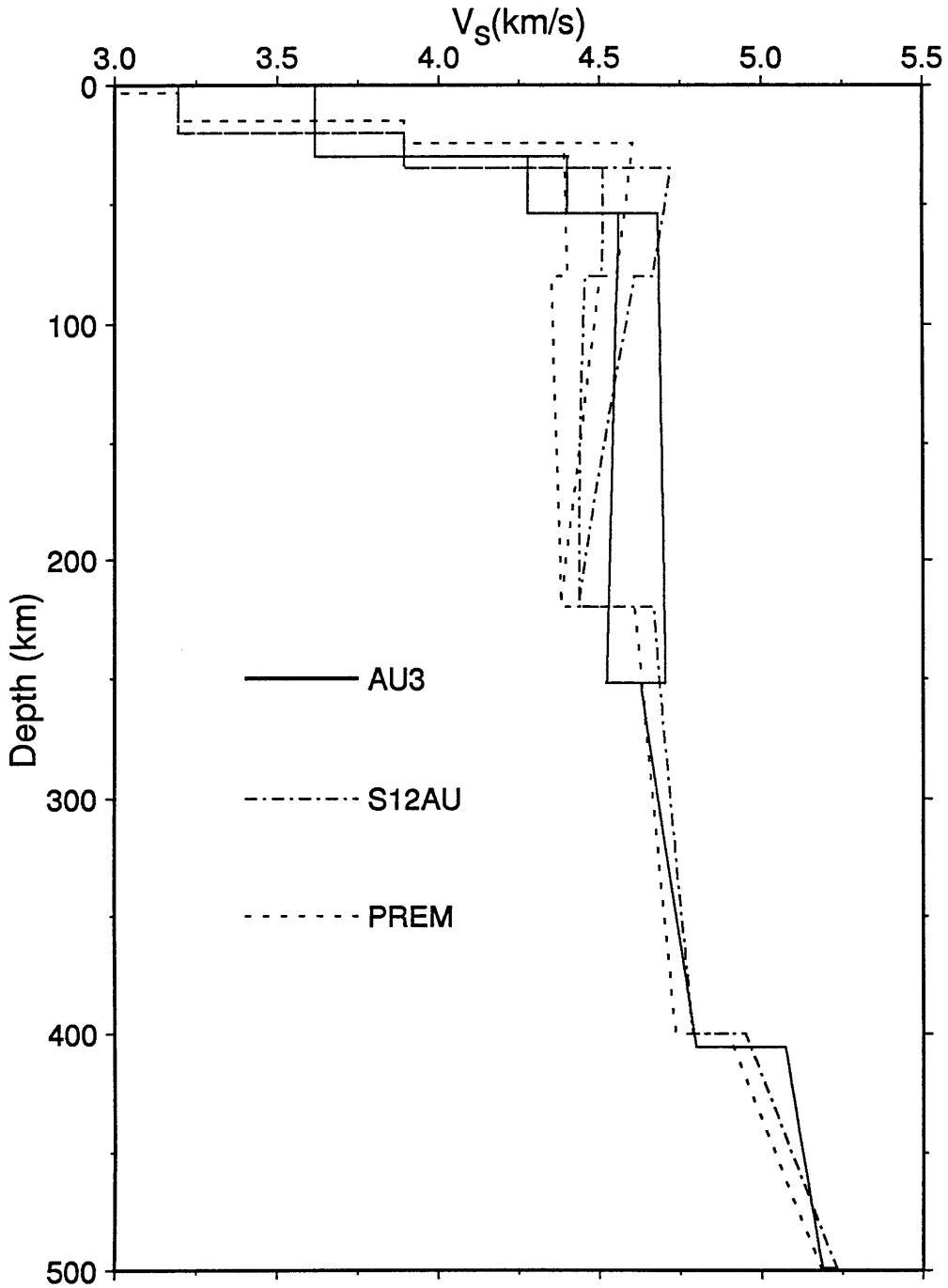
V_S(km/s)
3.0
3.5
4.0
4.5
5.0
5.5
0
100
200
300
400
500
Depth (km)
AU3
S12AU
PREM

Figure 4.11

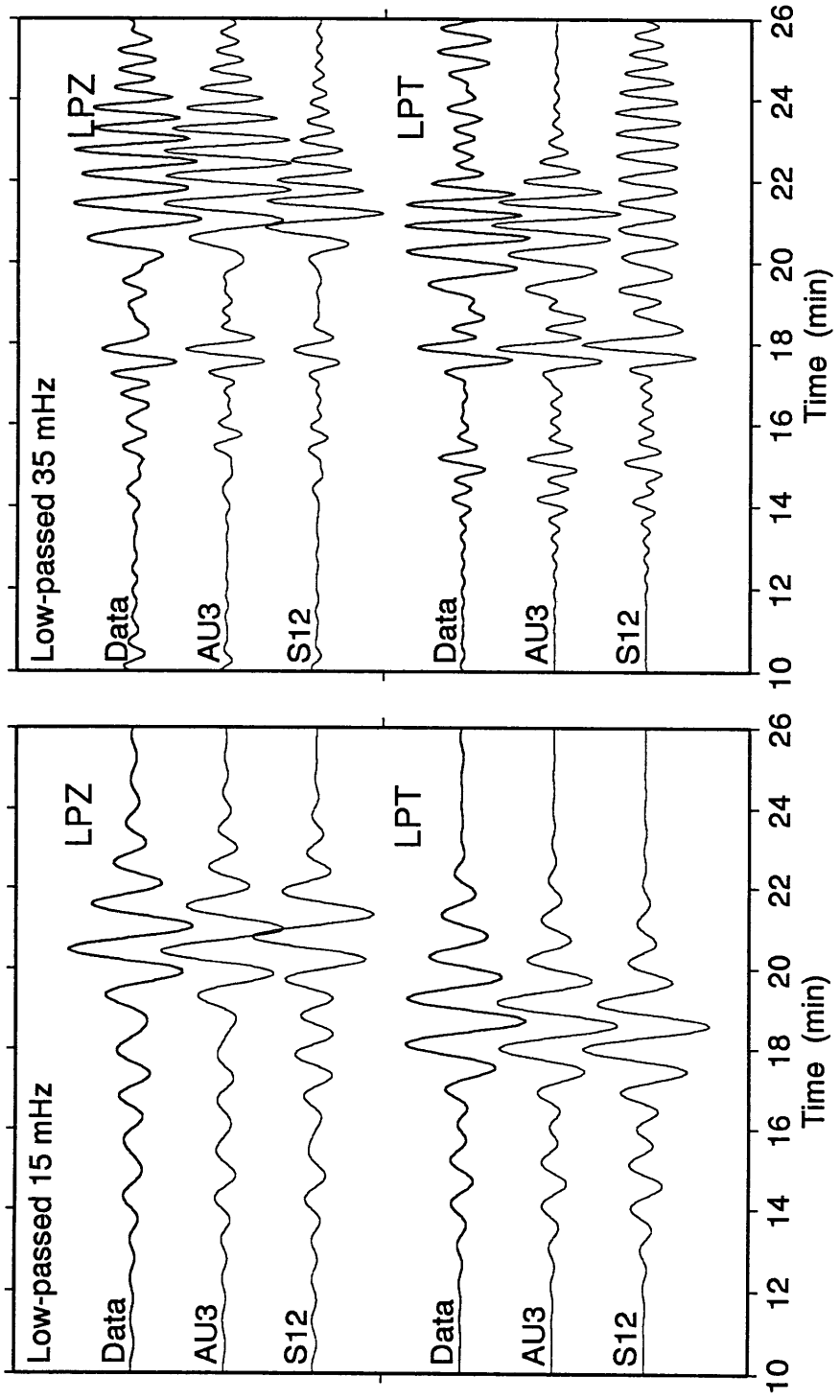
Low-passed 15 mHz
LPZ
Data
AU3
S12
LPT
Data
AU3
S12
10 12 14 16 18 20 22 24 26
Time (min)
Low-passed 35 mHz
LPZ
Data
AU3
S12
LPT
Data
AU3
S12
10 12 14 16 18 20 22 24 26
Time (min)

Figure 4.12

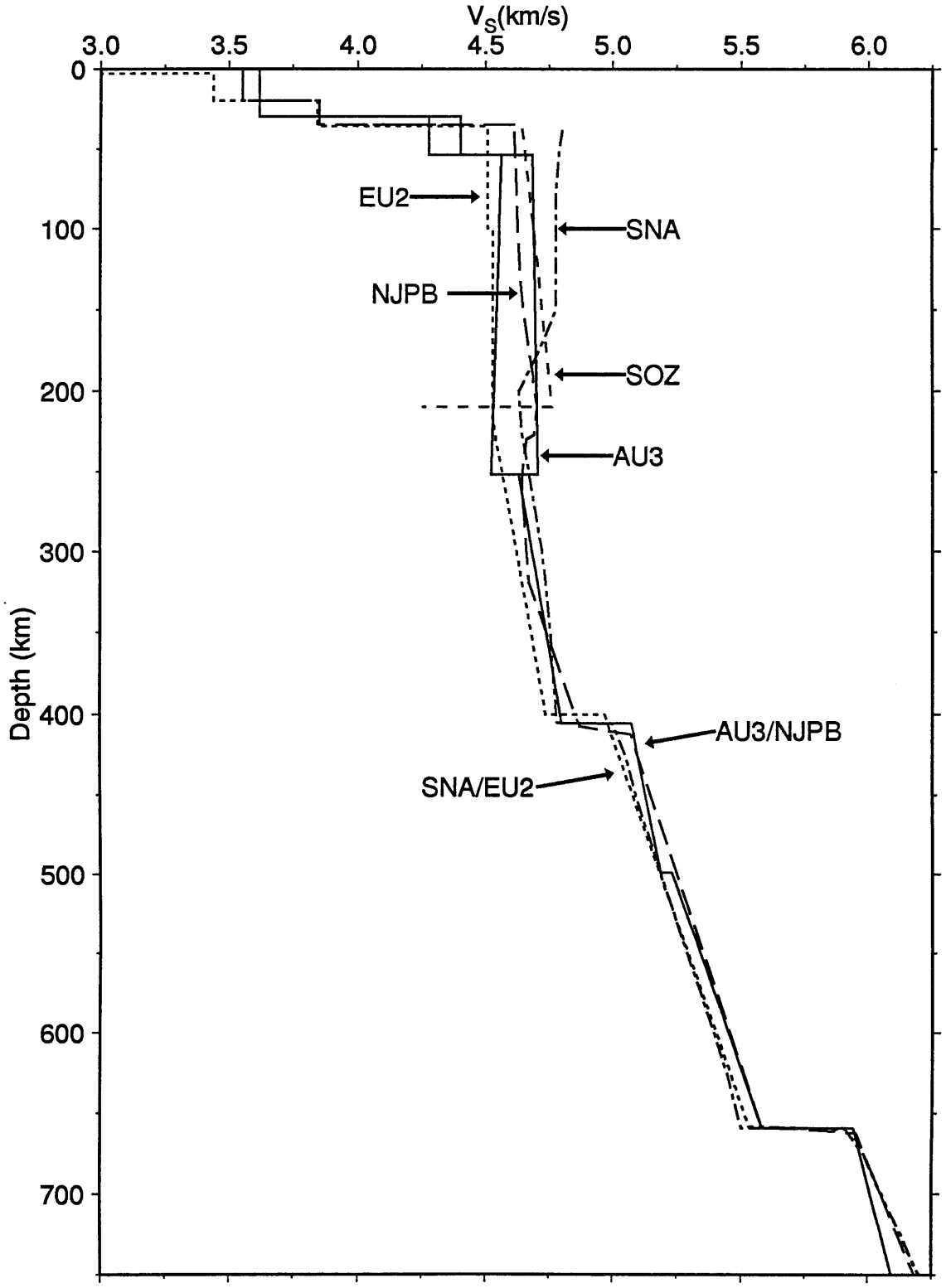
V_S(km/s)
3.0
3.5
4.0
4.5
5.0
5.5
6.0
0
100
200
300
400
500
600
700
Depth (km)
EU2
SNA
NJPB
SOZ
AU3
AU3/NJPB
SNA/EU2

Figure 4.13

CHAPTER 5

Lehmann Discontinuity as the Base of an Anisotropic Layer Beneath Continents

Seismic data from continents indicate a structural discontinuity at an average depth near 220 km. *Lehmann* [1959, 1961] was the first to suggest that an increase in *P*-wave and *S*-wave speeds at this level could explain the behavior of refracted arrivals from North America and Europe at epicentral distances between 10° and 20°, and she identified the jump with a sharp lower boundary of the asthenospheric low-velocity zone (LVZ). Subsequent authors have argued that this Lehmann (L) discontinuity occurs globally [*Anderson*, 1979; *Hales*, 1991], and *Dziewonski and Anderson* [1981] built it into the spherically averaged Preliminary Reference Earth Model (PREM). Solid-solid phase changes and chemical changes in ultramafic mantle rocks were ruled out as explanations of the L discontinuity [*Levin et al.*, 1981], which led *Hales* [1991] to conclude that it represents the termination of a zone of partial melting, in agreement with Lehmann's basic hypothesis. *Shearer* [1990] did not detect L in his global stacks of long-period waveforms, however, and *Revenaugh and Jordan* [1991c] show from a detailed analysis of *ScS* reverberations that its magnitude correlates inversely with the strength of the LVZ over a large area of the western Pacific and Australasia: L is small or absent on paths traversing oceans and marginal basins where the lid-LVZ boundary exhibits a large, negative contrast in shear impedance (G discontinuity), but is pronounced on continental and island-arc paths lacking a G discontinuity, where the LVZ is weak or absent altogether. Seeking alternative mechanisms, we test several hypotheses that are based on the effects of seismic anisotropy.

L AS AN ANISOTROPIC BOUNDARY

Leven et al. [1981] first proposed that L might be related to shear-induced anisotropy in the subcontinental mantle. From a reanalysis of *P*-wave refraction data in northern Australia, they derive a structure that features a high-velocity zone in the depth interval 190-225 km. They interpret the high velocities to be an expression of the horizontal alignment of olivine crystals by the northward motion of the Australian continent and propose that L is the upper boundary of a thin plate-decoupling zone underlying a nearly isotropic continental mechanical boundary layer (Figure 5.1*a*). This model does not account for the large polarization anisotropy observed for other continental regions, however [*McEvilly*, 1964; *Leveque and Cara*, 1983; *Gee and Jordan*, 1988]. It also is inconsistent with upper-mantle reflectivity profiles for Australia obtained from *ScS* reverberations, which indicate a ~2% increase in *SV* impedance at an L discontinuity with depths ranging from about 200 km along the northern Australian margin to over 250 km beneath the western Australian craton [*Revenaugh and Jordan* , 1991c].

Noting that the *SV* increase occurs near the level where some studies of *SH* waves in continents have found a shear-velocity decrease [*Grand and Helmberger*, 1984a, 1985], *Revenaugh and Jordan* [1991c] proposed that L marks the transition from an anisotropic mechanical boundary layer (MBL) to a more isotropic region below the MBL; the drop in the magnitude of the polarization anisotropy across this narrow (< 30 km) transition causes an increase in v_{SV} and decrease in v_{SH} with depth, although the isotropically averaged wave speeds and the density do not change appreciably (Figure 5.1*b*). Based on the apparent deepening of L towards the center of the western Australian craton, they speculated that this transition occurs at a critical temperature (near 1200°C) for the annealing of aligned textures in peridotites. They also pointed out that this horizon must be an internal feature of the continental thermal boundary layer, or tectosphere, whose thickness beneath cratons has been estimated to exceed 300 km [*Jordan*, 1975].

Karato [1992] accepted Revenaugh and Jordan's explanation of L as the rapid downward extinction of anisotropy, but he rejected their inference that such a feature could be maintained in a region of low deformation rate internal to the tectosphere. Instead, he proposed that L represents the transition from dislocation-controlled creep to diffusion-controlled creep in an actively deforming asthenosphere beneath the continental plate (Figure 5.1*c*), and he reiterated *Anderson's* [1979] suggestion that the tectospheric thicknesses obtained by *Jordan* [1975] could be biased to high values owing to anisotropic effects.

We evaluate the hypotheses illustrated in Figure 5.1 using the high-resolution, regionalized models of upper-mantle structure developed in Chapters 2 and 4.

DISTRIBUTION OF ANISOTROPY BENEATH AUSTRALIA

Our preferred Australia model (Chapter 4, Figure 4.9) is characterized by an anisotropic mantle above an L discontinuity located at a depth of 252 ± 5 km, and an isotropic mantle below this boundary. The relative *S*-wave and *P*-wave anisotropies are comparable, averaging 3.3 ± 0.5% and 3.7 ± 1.5%, respectively (although our data determined the former much better than the latter). The transition from an anisotropic to isotropic elastic structure at L is marked by an increase in *SV* impedance, consistent with the contrast observed for vertically propagating *ScS* reverberations, but a decrease in *SH* impedance. The latter feature of the Australia model yields an *SH* low-velocity zone similar to those inferred for other continental regions [*Grand and Helmberger*, 1984a, 1985]. It should be noted, however, that the density and mean values of the elastic parameters are almost continuous across L (Figure 5.2), as expected for a discontinuity that represents only a mechanical change in structure with no accompanying change in composition or phase.

As detailed in Chapter 4, we performed a number of inversions invoking a variety of prior constraints on the velocity distribution to test explicitly the hypotheses presented in

Figure 5.1. The surface- and turning-wave data for the Australia corridor required significant radial anisotropy averaged over the upper 200 km of the mantle. Restricting the anisotropy to a layer below 200 km depth, as in Figure 5.1*a*, resulted in models that did not satisfy the Love-Rayleigh discrepancy and *SS* splitting observations. On the other hand, the *S* and *SS* splitting data constrained the magnitude of the anisotropy below L to be small (<1%), and inversions that allowed anisotropy in the layer between the L and the 410-km discontinuities yielded no significant improvement in the fit to the data relative to the preferred model of Figure 4.9. The Australian data are therefore consistent with L being the lower boundary of the anisotropic layer.

UPPER-MANTLE SHEAR VELOCITIES BENEATH CONTINENTS AND OCEANS

To discriminate between the hypotheses illustrated in Figures 5.1*b* and 5.1*c*, we compared the shear-wave velocity structures derived for the Australian and Pacific corridors (Figure 5.2). The shear-wave anisotropy of the uppermost mantle along the Tonga-to-Hawaii path was found to be similar in magnitude to the Australia path and to extend below the G discontinuity into the oceanic LVZ, terminating at a weak discontinuity (unresolved by the *ScS* reverberation data) at a depth of 170 km (Chapter 2). Below G, however, the mean shear velocities were lower in the oceanic case, and this difference persisted to depths greater than 350 km. Attempts to satisfy both the Pacific and Australia data sets with models having similar shear velocities below 250 km were unsuccessful. Global tomographic models [*Woodhouse and Dziewonski*, 1984; *Su et al.*, 1984] and other regional studies [*Grand and Helmberger*, 1984; *Lerner-Lam and Jordan*, 1987] have demonstrated that differences between old continents and old oceans of this magnitude and depth are a global feature, indicative of a thick tectosphere beneath most Precambrian continental shields and platforms [*Jordan*, 1975; *Jordan et al.*, 1989]. We infer that the average thickness of the continental tectosphere beneath the Australia corridor is greater than 300 km, and we conclude that L is a transition internal to the tectosphere (Figure 1*b*),

rather than a boundary within an actively deforming asthenosphere beneath the continental plate (Figure 1*c*).

DISCUSSION

This result implies that the anisotropy above L is frozen in an MBL, or lithosphere, that forms the cold upper part of the tectosphere. The anisotropy is most plausibly related to the lattice preferred orientation of olivine and pyroxene, two highly anisotropic minerals known to dominate upper-mantle mineralogies [*Estey and Douglas*, 1986; *Nicolas and Christensen*, 1987]. In the oceanic lithosphere, the fast axes of olivine tend to be horizontally aligned in the directions of the plate-scale flow associated with sea-floor spreading, giving rise to azimuthal anisotropy that is coherent over large geographic distances [e.g. *Nishimura and Forsyth*, 1989]. Large-scale, coherent anisotropy related to plate motion also has been advocated for sublithospheric mantle in continental regions from observations of *SKS* splitting [*Vinnik et al.*, 1992, 1995]. Although such data cannot directly constrain the depth distribution of the anisotropy, *Vinnik et al.* [1995] hypothesize that beneath the South African craton the splitting arises from 2% anisotropy located between 175-400 km depth. Our result for Australia is in conflict with this inference from a similar stable continental region; it is in better agreement with upper-mantle anisotropy that appears to be inherited from episodes of orogenic deformation [*Silver and Chan*, 1991; *Silver and Kaneshima*, 1993]. The superposition of many such episodes over the long, complex history of the continents yields a deformation fabric with a local orientation that varies on a much smaller geographical scale than the plate-tectonic flow field. In Australia, for example, the lineaments in the gravity field associated with basement deformations have lateral scale lengths on the order of a few hundred kilometers [*Rutland*, 1979]. If this is the appropriate scale length for the decorrelation of the lattice preferred orientation within the uppermost mantle beneath Australia, then waves propagating over epicentral distances of

30°-40° will average out the azimuthal variations, and the path-averaged structure can be approximated by a transversely isotropic effective medium.

To test this inference we collected another data set from earthquakes in the Banda Sea to station CAN in southeast Australia (Figure 5.2 inset). Although this path largely samples the upper mantle beneath the margin and younger tectonic regions of eastern Australia, it is nearly orthogonal to that used in the inversion, and thus provides a good test of azimuthal variations in anisotropy. Although the effect of the different propagation paths is readily apparent in the relative dispersion, we find that the Love-Rayleigh discrepancy and *SS* splitting are quite similar, implying that the anisotropy is comparable for the two paths (Figure 5.3).

We consider stochastic models of upper-mantle heterogeneity in which orthorhombic peridotites have fast axes that are preferentially horizontal, but randomly oriented in azimuth (Figure 5.4). In these stochastic models, the spatial distribution of orientations is scale-invariant (fractal) up to some horizontal correlation length (outer scale) l_h and some vertical correlation length l_z. We distinguish two cases: equidimensional stochastic heterogeneity, with an aspect ratio near unity ($a \equiv l_h/l_z \sim 1$), and a stochastic laminate, with a large aspect ratio ($a >> 1$). Voigt averages of these models about a vertical axis of symmetry [e.g. *Estey and Douglas*, 1986] results in transversely isotropic effective media with elastic properties that are independent of l_h and l_z. The radial anisotropy implied in such models can be made to match the Australia data using a local anisotropies derived from mantle xenoliths brought to the surface by kimberlite pipes, which ranges from 3 to 8% (Figure 5.5) [*Mainprice and Silver*, 1993; *N.I. Christensen, personal communication*, 1994]. The relative shear-wave anisotropy of 3% obtained for Australia can be made consistent with these somewhat larger values by invoking dispersion of the olivine fast axis out of the horizontal plane.

At high frequencies, the anisotropic heterogeneity in Figure 5.4 generates strong multiple scattering that couples the *SV* and *SH* wave fields, thereby mixing the shear-wave

polarizations; this scattering may explain why the apparent S_n speeds observed in western Australia on short-period, vertical-component seismograms by *Bowman and Kennett* [1993] are consistent with our *SH* velocities, not our *SV* velocities, and why *Tong et al.* [1994] did not observe much *S*-wave splitting on (horizontal) paths sampling the lithosphere in the northern margin of Australia. A distribution of vertical shear-wave splitting results across the Australian continent would provide a means to test these models, but to date these observations only exist for two points on the periphery of the continent [*Vinnik et al.*, 1992]. Although L is represented in AU3 as a discrete discontinuity, we note that the *ScS* reverberations, as well as the other data used in this study, cannot distinguish a sharp transition from one spread out over a depth interval of about 30 km. A transition zone of such width would explain why L is not consistently observed in studies of higher frequency converted waves [*Bock*, 1988].

The extinction of low-frequency polarization anisotropy at the L discontinuity can arise from either the disappearance of anisotropy at local (hand-specimen) scales or the randomization of the fast-axis orientation out of the horizontal plane at larger geological scales. The first could be explained in terms of a kinetic boundary associated with long-term, thermally activated annealing of ancient deformation fabrics [*Boullier and Nicolas*, 1975; *Mainprice and Silver*, 1992] or, alternately, by *Karato's* [1992] rheological transition from dislocation to diffusion creep, although his proposal must be modified to generate an L discontinuity that is a relic feature frozen into the continental tectosphere. The second could be caused by a depth variation in the types of strains fields active during tectospheric stabilization and any subsequent remobilization; for example, with deformations in the region above L involving more horizontal flows and those below L involving displacements with larger vertical components.

The L discontinuity is located near the maximum depth of equilibration observed for suites of kimberlite xenoliths from several continental cratons, which averages about 220 km [*Finnerty and Boyd*, 1987]. This equilibration level evidently marks the transition from

slow diapiric upwelling of kimberlite magmas (or their precursors) [*Green and Gueguen*, 1974] through a ductile lower tectosphere to the much more rapid upward transport of melt via magma fracturing through a stronger lithosphere [*Spence and Turcotte*, 1990]. In this sense, the L discontinuity in continents may correspond to the base of a mechanical boundary layer that overlies a more mobile, dynamically active part of the continental tectosphere. The apparent deepening of L beneath the western Australian craton suggests that this rheological transition may be controlled by an isotherm at 1200-1300°C. The transition also appears to correspond to a rapid increase in shear-wave attenuation observed at about this depth by *Gudmundsson et al.* [1994].

Although L is not a global feature and appears to have a continental affinity, credible observations of discontinuities at depths of 180-220 km have been made in island-arc [*Vidale and Benz*, 1992] and marginal basin environments [*Revenaugh and Jordan*, 1991c]. Additional data will be needed to determine whether these discontinuities can be explained by the anisotropy-isotropy transition discussed here or require some other mechanism, such as the termination of a low-velocity zone, as favored by Hales and others. In this regard, we note that *Revenaugh and Sipkin* [1994] have recently invoked both mechanisms to explain the multiplicity of discontinuities they observe in *ScS* reflectivity profiles crossing China and the Tibetan Plateau.

FIGURE CAPTIONS

Fig. 5.1. Schematic cross-sections of the continental upper mantle illustrating three competing hypotheses regarding the relationship of the L discontinuity to upper-mantle anisotropy. Models are those of (A) *Levin et al.* [1981], where the anisotropy is confined to a narrow shear decoupling zone below L at the base of the continental plate (tectosphere); (B) *Revenaugh and Jordan* [1991c], where L is the base of an anisotropic mechanical boundary layer overlying a nearly isotropic layer that forms the lower part of a thick (> 300 km) tectosphere; and (C) *Karato* [1992], where L is the transition from dislocation to diffusion creep in an actively deforming asthenosphere beneath a thin (< 200 km) tectosphere. Thickness of the shear decoupling zone is not constrained in either model (B) or (C). Diagrams labeled $\Delta v_S/v_S$ show the perturbations to the *SV* (*solid line*) and *SH* (*dashed line*) wavespeeds relative to the isotropic average; *left* is for model (A), *right* is for both models (B) and (C).

Fig. 5.2. Comparison of shear-wave structures for the Australian and Pacific corridors. Mean shear-wave speeds are plotted for Pacific (*dashed-dot line*) and Australia (*solid line*) in the center diagram, and the anisotropic velocity perturbations relative to these mean velocities are displayed on the left and right, respectively. The contrasts in velocities and discontinuity structure inferred above a depth of about 350 km are evidence for a thick tectosphere beneath Australia. *Inset map* shows earthquakes and seismic stations that define the Pacific (*dashed-dot line*) and Australian (*solid line*) corridors. New Britain (*stars*) events recorded at NWAO were used to generate the Australia model, while Tonga events (*dots*) recorded at HON and KIP were used for the Pacific model. Banda Sea earthquakes (*crosses*) recorded at CAN form an alternative continental corridor (*dashed line*) used to test for azimuthal variations in anisotropy beneath Australia.

Fig. 5.3. Comparison between average measured phase delays (relative to isotropic model AU1, as a function of frequency) between the New Britain-NWAO and Banda Sea-CAN corridors. Data for the New Britain-NWAO corridor are shown as solid lines; data for the Banda Sea-CAN corridor are shown as dashed lines. a) Love- and Rayleigh-wave residuals. b) SS_H and SS_V residuals. Although there are small differences in the dispersion, the amount of shear-wave splitting is essentially identical, indicating that the azimuthal components of anisotropy are small at these epicentral distances.

Fig. 5.4. Schematic diagrams of two types of anisotropic heterogeneity considered in our research. *Left panel:* equidimensional stochastic heterogeneity, where the ratio of horizontal to vertical correlation length is near unity ($a \sim 1$). *Right panel:* a stochastic laminate, where this aspect ratio is large ($a \gg 1$). Both types of structures can explain the low-frequency polarization anisotropy observed in Australia, but their implications for high-frequency wave propagation are very different.

Fig. 5.5. Plot of the P anisotropy ratio against the S anisotropy ratio, comparing AU3 (triangle) and its 90% confidence ellipse (shaded region) against theoretical values for anisotropic stochastic heterogeneity with various assumptions of local anisotropy. The models include both the Voigt-average predictions for ideally aligned, hypothetical compositions (squares) and local anisotropies measured by *N.I. Christensen* [personal communication] in a suite of peridotitic xenoliths (circles). The magnitude of the shear-wave anisotropy observed in Australia falls at the lower end of the range predicted by the models, while the compressional-wave anisotropy is significantly smaller. The comparison can be improved by modifying the models to have fast axes dispersed out of the horizontal plane.

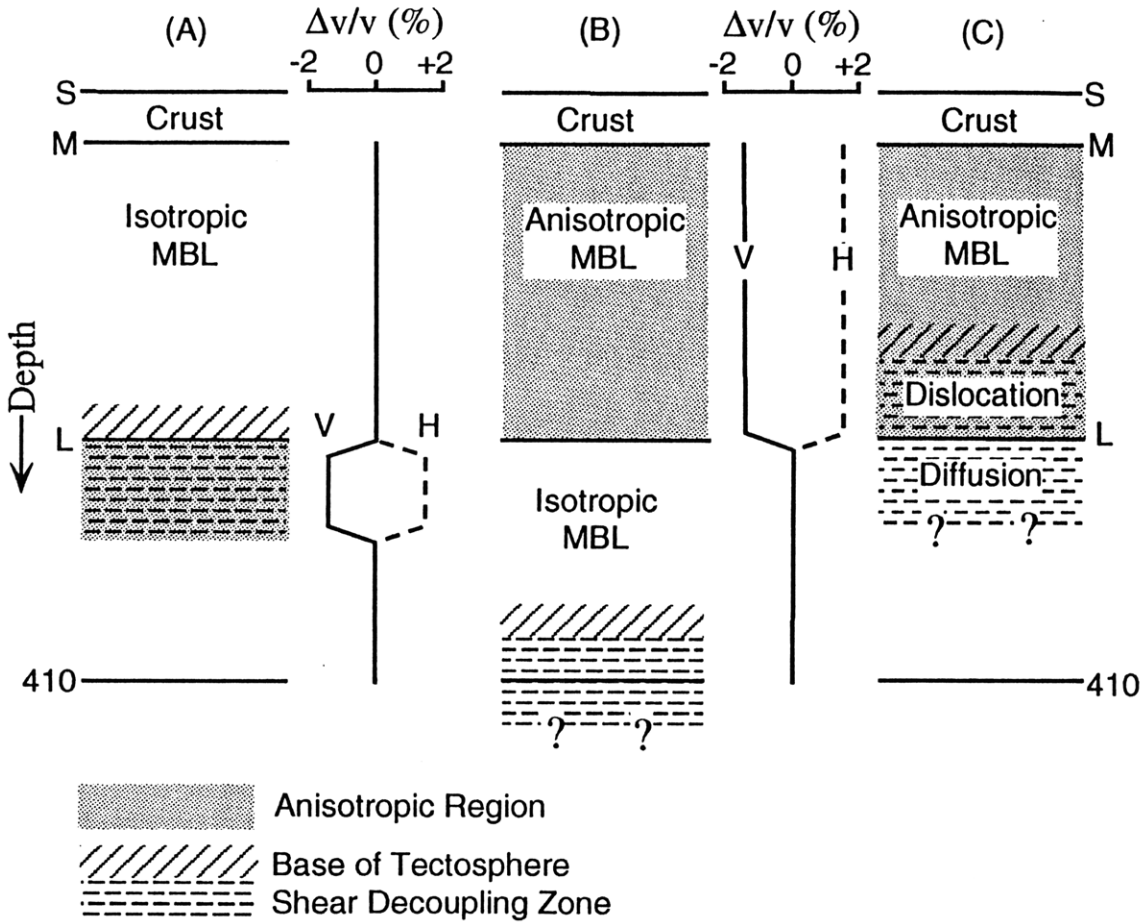
(A)
Δv/v (%)
-2 0 +2
S
Crust
M
Isotropic
MBL
Depth
L
V
H
410
(B)
Δv/v (%)
-2 0 +2
Crust
Anisotropic
MBL
V
H
Isotropic
MBL
?
?
(C)
S
Crust
M
Anisotropic
MBL
Dislocation
L
Diffusion
?
?
410
Anisotropic Region
Base of Tectosphere
Shear Decoupling Zone

Figure 5.1

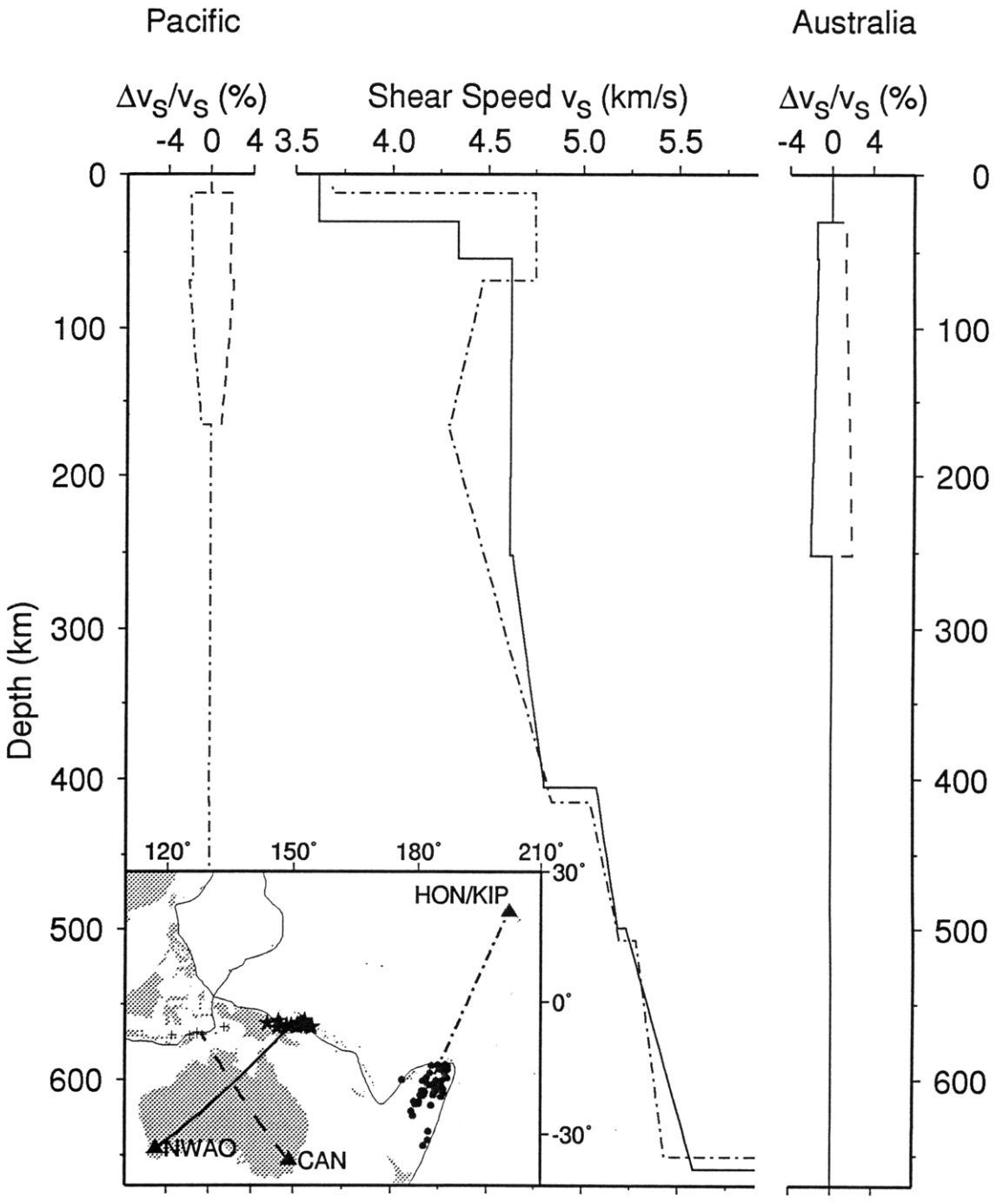
Pacific
Australia
$\Delta v_S/v_S$ (%)
Shear Speed v_S (km/s)
$\Delta v_S/v_S$ (%)
-4 0 4
3.5 4.0 4.5 5.0 5.5
-4 0 4
Depth (km)
0
100
200
300
400
500
600
120°
150°
180°
210°
30°
0°
-30°
HON/KIP
NWAO
CAN

Figure 5.2

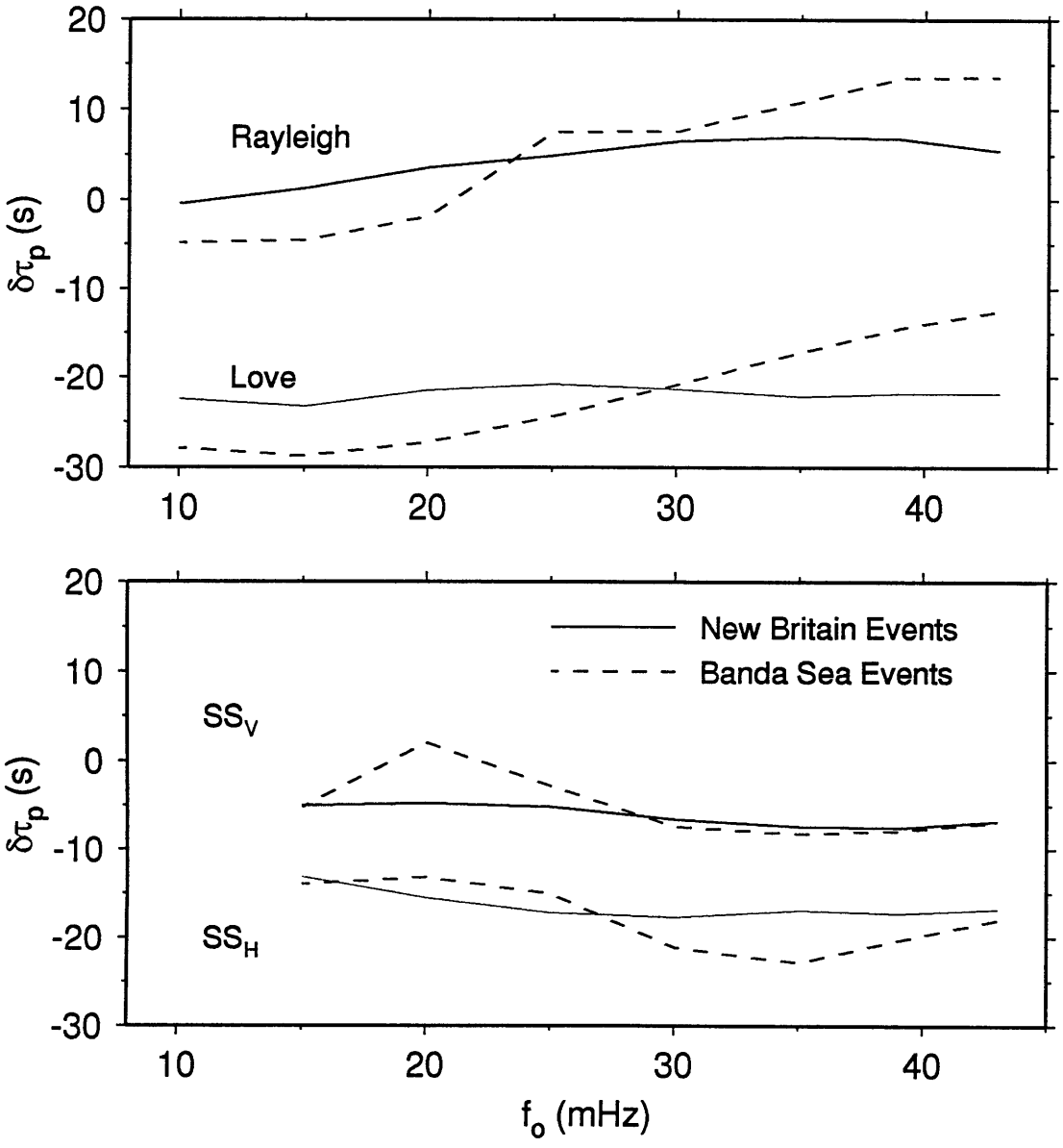
20
10
0
-10
-20
-30
$\delta\tau_p$ (s)
Rayleigh
Love
10
20
30
40
New Britain Events
Banda Sea Events
SS_V
SS_H
f_o (mHz)

Figure 5.3

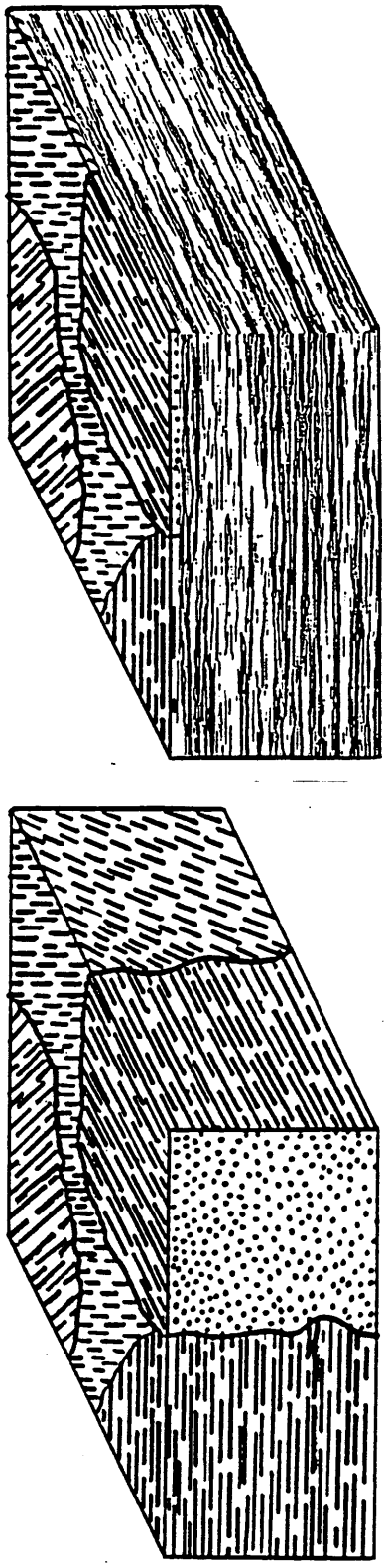

Figure 5.4

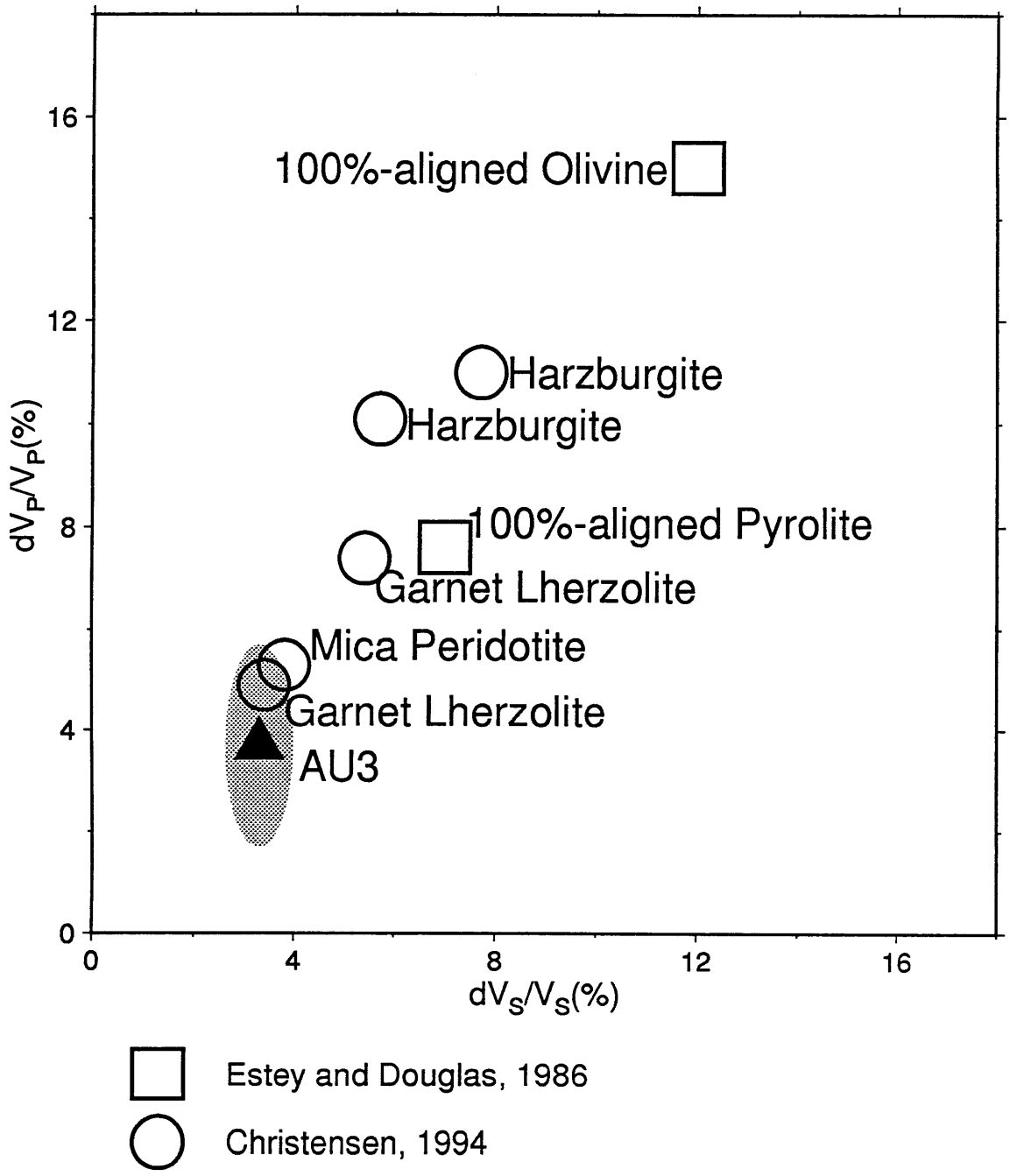
16
12
8
4
0
0
4
8
12
16
$dV_P/V_P(\%)$
$dV_S/V_S(\%)$
100%-aligned Olivine
Harzburgite
Harzburgite
100%-aligned Pyrolite
Garnet Lherzolite
Mica Peridotite
Garnet Lherzolite
AU3
Estey and Douglas, 1986
Christensen, 1994

Figure 5.5

CHAPTER 6

Ocean-Continent Comparisons and Future Directions

We have presented new regional seismic models of the upper mantle from two narrow, well-isolated corridors -- one traversing the western Pacific, one crossing western Australia -- using a one-dimensional, path-average, transversely isotropic (radially anisotropic) parameterization. Our analysis is unique in several aspects compared to most analyses of upper mantle structure: we have analyzed seismograms more completely in both time (multiple phases -- *S*, *SS*, *SSS*, surface waves, all on three components) and frequency (travel time behavior across the 10-45 mHz band) than most structural studies; we directly incorporate data from the reflected wavefield (*ScS* reverberations) in order to constrain the discontinuity structure; we utilize a self-consistent three-component analysis and inversion procedure that allows us to jointly determine all the velocity components of a radially anisotropic model. The restriction of our analysis to short corridors that cross simple, tectonically stable regions of oceanic and continental upper mantle minimizes the expense of our path-average approximation. As shown in Chapters 2 and 4, this assumption is further justified *a posteriori* by our ability to fit observed seismograms with a radial model. The utility in this methodology for characterizing structure beneath the western Pacific and western Australia, and the geophysical inferences that result, has been documented in the earlier chapters of this thesis. Here we expand on the ocean-continent comparison that was initiated in Chapter 5. The self-consistency in the data and analysis procedures used in constructing models PA5 and AU3 allows them to be directly compared to infer lateral variations of structure in the upper mantle.

OCEAN-CONTINENT COMPARISONS

Anisotropic Structure

To first order, the shear-wave radial anisotropy observed beneath the western Pacific and western Australia are remarkably similar (Figure 6.1). In detail, the magnitude of PA5's anisotropy peaks at 4.1±0.5%, while AU3 has a maximum anisotropy of 3.3±0.5%. The errors imply that the difference may not be strictly resolvable, but if it holds, it seems to imply that the tectonic forces responsible for olivine alignment in the upper mantle more efficiently align olivine in a horizontal orientation in oceanic mantle relative to continental mantle.

The depth distributions of anisotropy also differ slightly, with PA5's anisotropy terminating near 170 km, while AU3's extends to approximately 250 km depth. As discussed in Chapter 5, the mechanisms controlling the expected transition from anisotropy to apparent isotropy are not clear; they may be controlled by changes in creep mechanism [*Karato*, 1992] or the form and/or geometry of shear deformation [*Ribe*, 1989]. As these mechanisms are strongly temperature-dependent, it is useful to consider the anisotropic difference jointly with the mean velocity profiles for the two models. At a depth of 150 km, the mean shear velocity in AU3 is nearly 0.3 km/s fast relative to PA5, which roughly translates to a 500°K difference in temperature (using a value for $\partial v_S/\partial T$ of -0.6 m/s/°K [*Sheehan and Solomon*, 1991]). Due to the strong temperature-dependence of viscosity [e.g. *Karato and Wu*, 1993], this temperature difference in turn represents a stiffness at least two orders of magnitude greater beneath Australia relative to the Pacific, and it is highly likely that the dynamic state of the mantle at this depth is quite different between the two regions. We infer that the anisotropy at 150-km depth beneath Australia is fossilized in the continental lithosphere, while the anisotropy at this depth beneath the Pacific is maintained by dynamic flow in the weak suboceanic asthenosphere. This difference probably explains why anisotropy beneath Australia terminates relatively discontinuously at

an observable L, but that beneath oceans terminates more smoothly (the discontinuity at 170-km depth in PA5 is too small to be detected using ScS reverberations).

Thermal and Mechanical Structure

The differences in the mean velocity structure through the upper 400 km are dramatic (Figure 6.1). The seismic lithosphere in PA5 has a thickness of approximately 70 km, and it is underlain by a substantial LVZ. In contrast, there is no similar "lid" observable in AU3. The seismic lithosphere in oceanic regions is defined by the G discontinuity, which is probably controlled by the approach of the solidus to the geotherm, leading to a sharp drop in seismic velocity and Q [*Sato et al.*, 1989; *Revenaugh and Jordan*, 1991c] and an increase in strain rate due to lower viscosity [*Karato and Wu*, 1992]. It is clear that no equivalent process occurs beneath stable continents, presumably because of the much colder geotherm.

The low velocities and steep gradient between 170-400 km depth in PA5, when compared to the high velocity and flat gradient in AU3, indicate that higher temperatures persist beneath the Pacific all the way to 400 km depth. In fact, if we assume that the 410-km and 660-km discontinuities arise due to endothermic and exothermic (respectively) phase changes in a peridotite mantle [e.g. *Bina*, 1991], then the behavior of the velocity profiles indicate that this temperature difference may persist throughout the transition zone. The relative depths of the 410-km discontinuity (415 km in PA5, 406 km in AU3), the average velocity profile between the 410-km and 660-km discontinuities, and the relative depths of the 660-km discontinuity (651 km in PA5, 659 in AU3) all indicate warmer temperatures beneath the Pacific than Australia throughout this depth range.

This behavior can be summarized by calculating the vertical S-wave one-way travel time to a variety of depths in the two models [e.g. *Jordan et al.*, 1989]. Figure 6.2 displays the difference in these travel time between PA5 and AU3, as well as two other representative ocean-continent models extracted from global model S12_WM13 [*Su et al.*, 1994]. Positive residuals on this graph indicate the amount of extra travel time required for

a shear wave to travel to a given depth in the oceanic model, relative to the continental model. Figure 6.2 indicates that the differences in velocity above 250 km depth in PA5 and AU3 result in a 1.5 s difference in vertical travel time. As the velocities begin to come together between 250-400 km depth, the vertical travel time residual continues to increase, but more slowly. The residual continues to increase between 400-650 km, indicating that PA5 is still slower than AU3 in this depth range. This can be compared to the radial 1D models for the western Pacific and western Australia extracted from S12_WM13 (S12TH and S12AU, from Chapters 2 and 4, respectively). These residuals indicate that while S12_WM13 characterizes the Pacific upper mantle as slow relative to western Australia, the nearly constant rate of increase of dT_V with depth indicates that as much of the heterogeneity is placed in the transition zone as in the upper mantle. The total vertical travel time difference through the entire upper mantle and transition zone agrees quite well with that inferred from PA and AU3, but most of the difference in PA5-AU3 is accumulated above 250 km depth. The comparison between AU3 and S12AU in Chapter 4 indicated that the uppermost mantle in S12AU is too slow to fit long-period surface waves, which agrees with the result here.

These vertical travel times allow us to evaluate the portability of our PA5-AU3 comparison to old oceans and stable continents in general [*Shapiro et al.*, 1995]. Figure 6.2 also includes the vertical travel time difference calculated for all old oceanic regions of S12_WM13 (regions B and C of *Jordan* [1981]) with all stable continental platforms and shields (regions P and S of *Jordan* [1981]). These residuals indicate that the Pacific-Australia differences in vertical travel time above 400-km depth are characteristic of old oceans and continents in general, but that the slow velocities in the transition zone are less characteristic of such regions in general. The relatively low value at 250 km is probably due to the inability of S12_WM13 to accurately characterize the upper-most mantle due to reliance on long-period surface waves, as discussed in Chapters 2 and 4. This discrepancy is averaged out by 400 km depth.

In addition to the differences in average velocity structure in the transition zone, there are several differences in the discontinuities and gradients between PA5 and AU3. These differences are related to differences in the discontinuity structures inferred by *Revenaugh and Jordan* [1991b,c]; notably, a large 410-km, small 520-km and small 660-km discontinuity beneath Australia relative to the Pacific. As the long-period body wave data only constrains the average velocity through this region, the details of this structure are controlled by the reverberation data. Higher-frequency *S* and *P* body-wave analysis will be required to evaluate these differences in more detail.

FUTURE DIRECTIONS

This thesis represents a first step in generating regional radially anisotropic models of the upper mantle. The scientific inferences on structure of the upper mantle beneath both old oceans and stable continents have been detailed herein. A variety of questions posed in Chapter 1 remain unanswered, however, and new questions have arisen. We therefore conclude with a discussion of the directions to be explored in the near future.

Regional Models of Upper Mantle Anisotropy

Our models characterize anisotropy in stable oceanic and continental regions. A variety of studies have previously documented variability of anisotropic structure using a global parameterization [e.g. *Nataf et al.*, 1986; *Tanimoto and Anderson*, 1991]. We would like to confirm these inferences using our path-average inversion approach, which characterizes the anisotropy in well-isolated corridors, without resorting to the low-frequency data and large-scale regionalization or low-resolution 3D inversion required in global studies. Regions of interest are numerous: differences in anisotropic structure between old, stable cratons and more tectonically active regions [e.g. *Nataf et al.*, 1986; *Gee and Jordan*, 1988]; relationship between anisotropy and L in marginal basins tectonically-active continental regions [e.g. *Revenaugh and Sipkin*, 1994]; presence and depth extent of vertically-oriented anisotropy beneath spreading centers [*Nataf et al.*, 1986;

Blackman et al., 1993]. This later example is particular intriguing, in that the depth extent of ridge material has been difficult to infer from isotropic 3D models [e.g. *Zhang and Tanimoto*, 1992; *Su and Dziewonski*, 1993], and good constraints on the depth extent of *SH/SV* anisotropy would provide additional information. The seismic corridor between events near Easter Island and stations in southern California and Mexico provides an excellent experimental geometry for such a study [*Grand and Helmberger*, 1984a; *Walck, 1984*; *Jones et al.*, 1992]. In general, the inclusion of *ScS* reverberation data in such analyses will also provide opportunities to test and expand on the discontinuity model presented in Figure 1.2.

Scale Lengths of Anisotropic Structure

The azimuthal invariance of the radial anisotropy observed in both the Pacific and Australia allowed us to conclude that possible azimuthal anisotropy in both regions must have length scales smaller than 40°. In Chapter 5 (Figure 5.4) we presented two stochastic models of anisotropic heterogeneity that average to transverse isotropy, each with markedly different length scales (or aspect ratios a). We plan to further investigate such stochastic models by developing averaging procedures [e.g. *Backus*, 1962] appropriate for wave propagation through such structures, and by investigating observables that will allow us to extract information on the aspect ratio of the anisotropy. Values of a appropriate for the upper mantle are ambiguous, not only from the point of view of our data, but also from other observations. For example, an anisotropic stochastic laminate ($a >> 1$) can potentially explain the S_n discrepancy [*Gee and Jordan*, 1988] and the *P*-wave "shingling" commonly observed on long-range refraction profiles [*Fuchs and Shulz*, 1976; *Cipar et al.*, 1993; *Ryberg et al.*, 1995]. But the splitting observed for vertically propagating *SKS* waves, which can be large and rapidly varying with receiver position [*Silver and Chan*, 1991; *Silver and Kaneshima*, 1993], suggests that the aspect ratio is low. It may be that a varies strongly both laterally and vertically in the subcontinental mantle. We will incorporate P_n, S_n, and *SKS* data into our modeling to improve the constraints on this

parameter and its regional variations. In continental regions, this will help characterize the nature of fossilized anisotropy, and thus the tectonic processes that formed it. In oceanic regions, such models may assist in determining the nature of dynamic flow beneath the oceanic plates.

Joint S-P Behavior and Mineralogy of the Upper Mantle

The Bayesian inversion scheme described in Chapter 2 provides a powerful tool for combining data from a variety of sources (in particular, seismic and mineralogical) in order to explore hypotheses on the composition and state of the upper mantle. A deceptively simple benefit is the ability to simultaneously evaluate the *S* and *P* velocity structure. In general, compressional models are generated from high-frequency *P* waves, and shear models from lower-frequency *S* waves, and the results can often differ remarkably, even in the same region [e.g. *Nolet et al.*, 1994]. An good example is seen by comparing *S* and *P* models of the upper mantle beneath the East Pacific Rise and Gulf of California [*Grand and Helmberger*, 1984a; *Walck*, 1984]. The shear model has a 410-km discontinuity located at 405-406 km depth, while the *P* model locates it at 390 km depth. Are these true differences due to mineralogy, or are they representative of the uncertainty in the different data sets and modeling procedures? Joint determination of *S* and *P* structure allows such mineralogical hypotheses to be explicitly tested.

The models in this thesis do not directly incorporate *P* waves; the *P* velocities are constrained via *SV*-type waveforms, as well as the mineralogical data. Despite this fact, it appears that the *P* velocities in (at least) AU3 are reasonably well-determined. Australia happens to be one of the few regions were a joint *S* and *P* upper mantle model has been developed (via forward modeling of high-frequency refraction profiles), and Figure 6.3 compares the *S* and *P* velocities in AU3 with this model NJPB [*Kennett et al.*, 1994]. Despite differences in frequency content and sampling region (NJPB samples primarily the northern margin of Australia), and noting the isotropy assumed for NJPB, the models are reasonably consistent throughout the upper mantle. The reason for differences in the upper

250 km are important to quantify, however, as they hold key implications for anisotropy and structure in the continental lithosphere. Are the differences due to regional variation, or due to frequency-dependent propagation through a stochastic model like those discussed above? In addition, are the variable gradients between 250 km and 400 km generally required, and if so, what implications do they hold for mineralogy? Further development of isolation filters capable of isolating such phases as *P* and *PP* will greatly increase our sensitivity to the compressional velocities, and will allow us to more formally test a variety of mineralogical models. In addition, by increasing the frequency range (to higher frequency) of both the shear and compressional data, we can focus on the detailed structure of the transition zone, which could not be investigated here.

FIGURE CAPTIONS

Fig. 6.1. Comparison of shear-wave structures for the Australian and Pacific corridors. Mean shear-wave speeds are plotted for Pacific (*dashed-dot line*) and Australia (*solid line*) in the center diagram, and the anisotropic velocity perturbations relative to these mean velocities are displayed on the left and right, respectively. The contrasts in velocities and discontinuity structure inferred above a depth of about 350 km are evidence for a thick tectosphere beneath Australia, while the differences in transition zone structure are consistent with higher temperatures beneath the Pacific in a pyrolite mantle.

Fig. 6.2. Differences in vertical one-way *S*-wave travel time between oceanic and continental models. Each point represents the vertical travel time between 40 km depth and a specified depth (250, 400, or 650 km) in an "oceanic" model relative to a "continental" model. Squares represent the vertical travel time in PA5 relative to AU3. Circles represent the vertical travel time in model S12TH (see Figure 2.14) relative to model S12AU (see Figure 4.11). Triangles represent the vertical travel time in all old ocean regions (regions B or C as defined by *Jordan* [1981]) relative to all shield and platform regions (P or S as defined by *Jordan* [1981]). The PA-AU difference implies that PA5 remains slow relative to AU3 throughout the upper mantle and transition zone, with the strongest heterogeneity in the upper 250 km. S12_WM13 smears this heterogeneity throughout the upper mantle and transition zone, but the total integrated anomaly above 650 km is maintained. The regionalization results indicate that oceans are slow relative to continents above 400 km; the extension of slow velocities into the transition zone is less clear. Regionalized data provided by *Shapiro* [1995].

Fig. 6.3 Comparison of shear and compressional velocities in AU3 (solid lines) with those determined by joint isotropic modeling of high-frequency *S* and *P* refraction profiles from

northern Australia (NJPB, dashed lines; from *Kennett et al.* [1994]). The shear wave comparison was made previously in Chapter 4. Although *P* waves are not included in our data, the *P* velocity in AU3 parallel those in NJPB reasonably well.

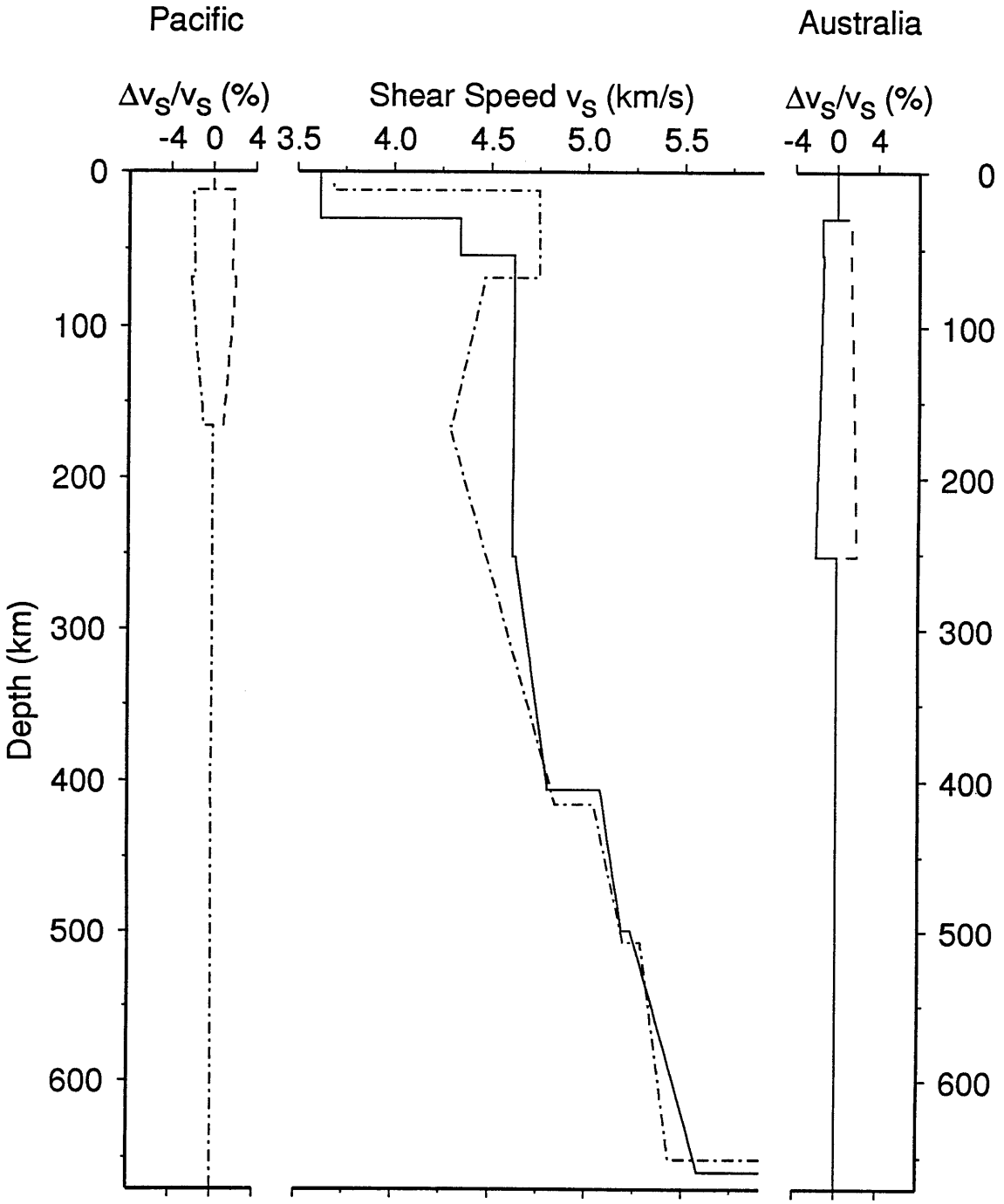
Pacific
Australia
$\Delta v_S/v_S$ (%)
-4 0 4
Shear Speed v_S (km/s)
3.5 4.0 4.5 5.0 5.5
$\Delta v_S/v_S$ (%)
-4 0 4
Depth (km)
0
100
200
300
400
500
600

Figure 6.1

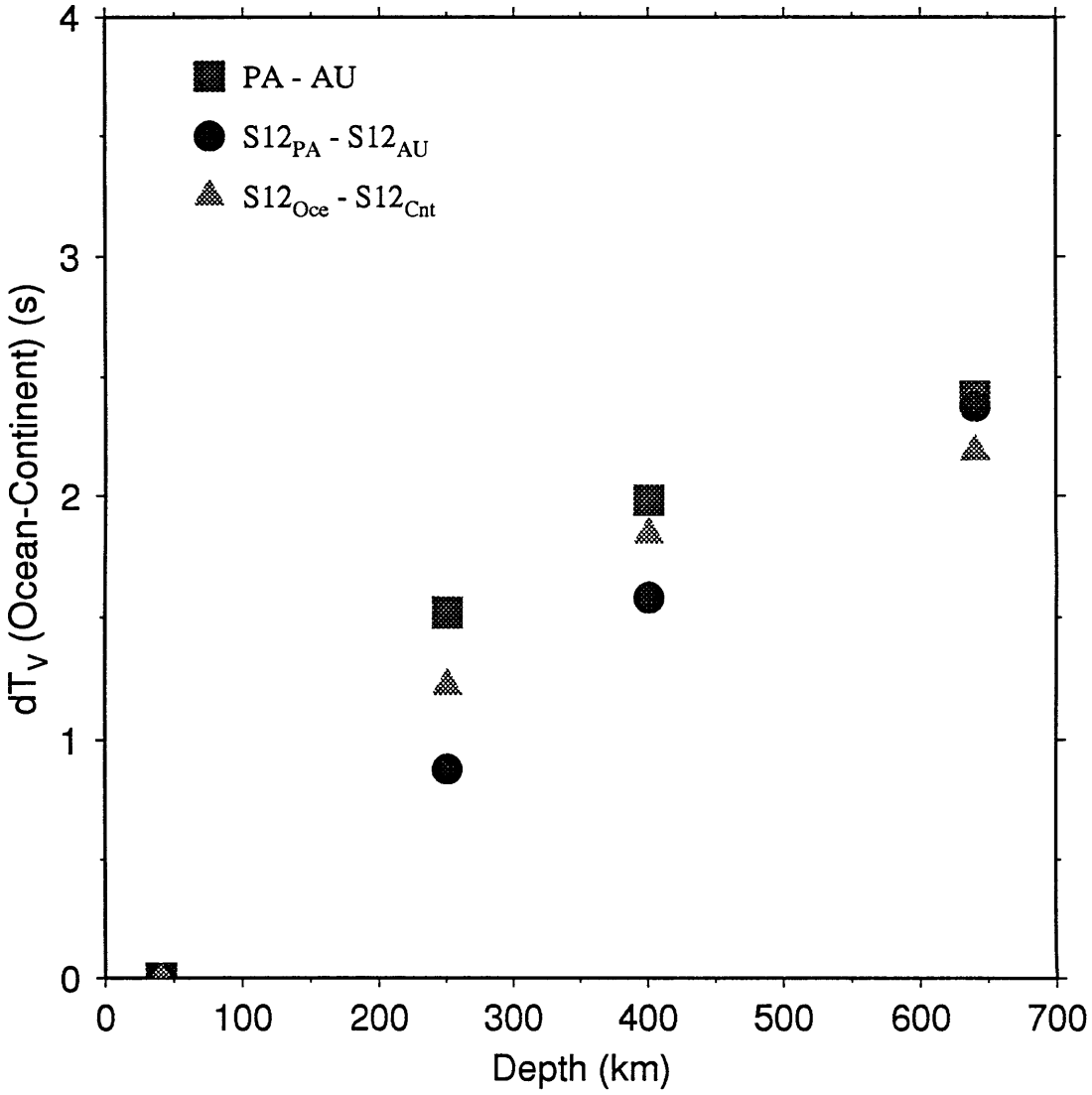
PA - AU
S12PA - S12AU
S12Oce - S12Cnt
dTv (Ocean-Continent) (s)
Depth (km)
0
1
2
3
4
0
100
200
300
400
500
600
700

Figure 6.2

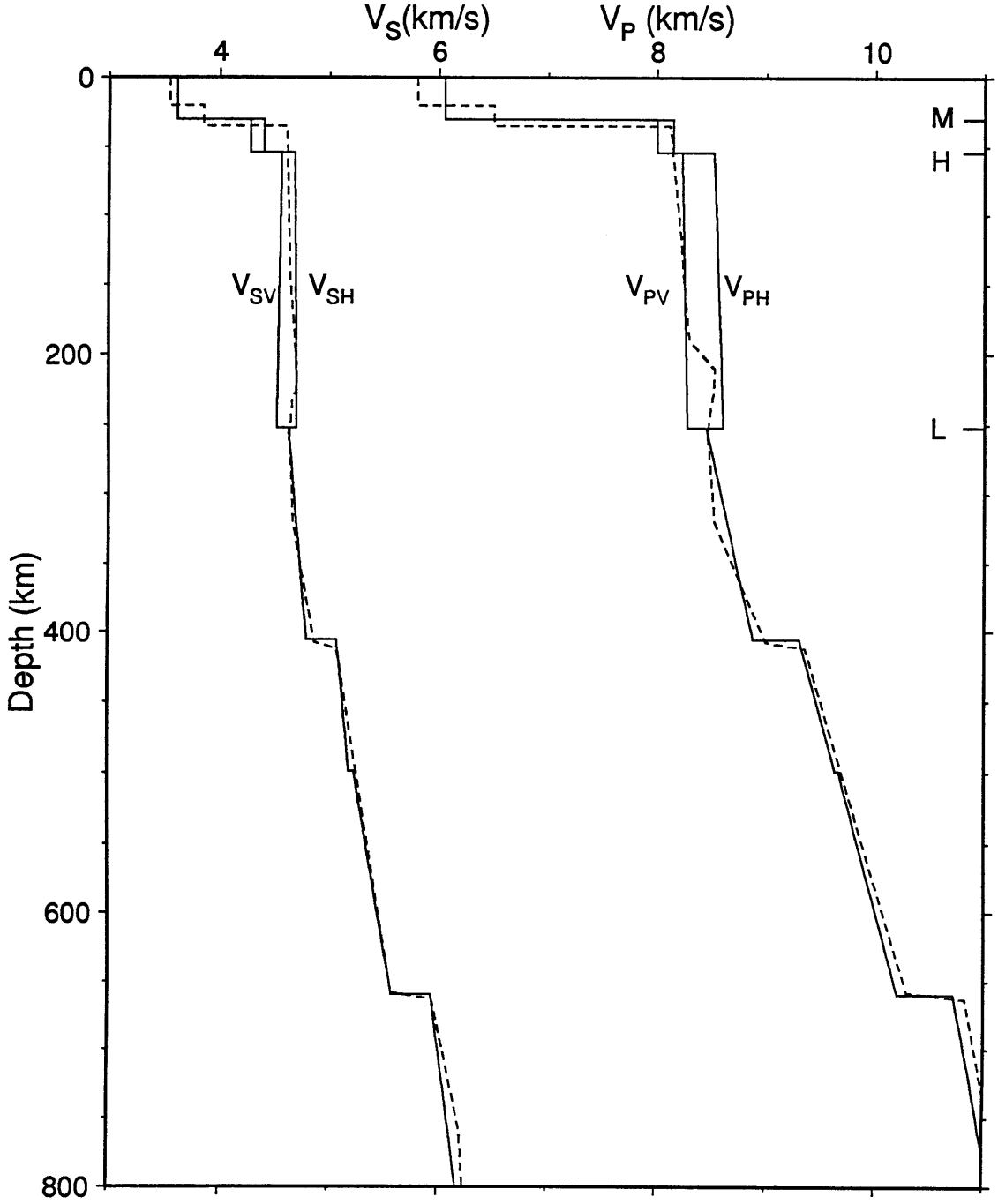
V_S(km/s)
V_P (km/s)
4
6
8
10
0
200
400
600
800
Depth (km)
M
H
L
V_{SV}
V_{SH}
V_{PV}
V_{PH}

Figure 6.3

APPENDIX

Partial Derivatives

PARTIAL DERIVATIVES FOR *ScS*-REVERBERATION DATA

ScS reverberations have very simple propagation characteristics when recorded over relatively short path lengths such as those presented here. Their ray paths nearly follow the radial gradient in a spherically symmetric earth, and they can be very well described using geometrical optics, even at relatively low frequencies [*Revenaugh and Jordan*, 1987]. Using a plane wave approximation, we can define the vertical incidence reflection coefficients and vertical travel times for each discontinuity in a spherically-symmetric model. In this section we present here the partial derivatives that allow us to relate our model parameters to these observations, allowing for inversion for an improved model.

Impedance Contrast

Consider a discontinuity at that base of a layer *i*, with depth z_i. We label the vertical shear velocity (v_{SV}) at the top of the layer v_i^t, while the velocity at the base of the layer (just above the *i*th discontinuity) is v_i^b. The velocity at the top of the next layer is therefore defined as v_{i+1}^t. We likewise define ρ_i^t, ρ_i^b, and ρ_{i+1}^t, the densities at the top of layer i, at the base of layer i, and at the top of the next layer, respectively. We can thus define the impedance contrast across the discontinuity at z_i as

$$R_o(z_i) = \frac{\rho_{i+1}^t v_{i+1}^t - \rho_i^b v_i^b}{\rho_{i+1}^t v_i^t + \rho_i^b v_i^b} \qquad \text{(A1)}$$

While this is a convenient description of $R_O(z_i)$, it is not written in terms of our model parameters; in particular, we need to rewrite v_i^b and ρ_i^b in terms of the gradients within the layer (g_i and s_i, respectively), and the discontinuity depths bounding the layer (z_{i-1} and z_i):

$$v_i^b = v_i^t + g_i(z_i - z_{i-1}) \tag{A2}$$
$$\rho_i^b = \rho_i^t + s_i(z_i - z_{i-1})$$

Substituting A2 into A1 and differentiating with respect to the model parameters results in the following set of eight partial derivatives associated with each $R_o(z_i)$.

Velocity intercepts:

$$\frac{\partial R_o}{\partial v_i^t} = \frac{-2\rho_i^b \rho_{i+1}^t v_{i+1}^t}{(\rho_i^b v_i^b + \rho_{i+1}^t v_{i+1}^t)^2} \tag{A3}$$

$$\frac{\partial R_o}{\partial v_{i+1}^t} = \frac{2\rho_i^b \rho_{i+1}^t v_i^b}{(\rho_i^b v_i^b + \rho_{i+1}^t v_{i+1}^t)^2} \tag{A4}$$

Velocity slope:

$$\frac{\partial R_o}{\partial g_i} = \frac{\partial R_o}{\partial v_i^t}(z_i - z_{i-1}) \tag{A5}$$

Density intercepts:

$$\frac{\partial R_o}{\partial \rho_i^t} = \frac{-2\rho_{i+1}^t v_i^b v_{i+1}^t}{(\rho_i^b v_i^b + \rho_{i+1}^t v_{i+1}^t)^2} \tag{A6}$$

$$\frac{\partial R_o}{\partial \rho_{i+1}^t} = \frac{2\rho_i^b v_{i+1}^t v_i^b}{(\rho_i^b v_i^b + \rho_{i+1}^t v_{i+1}^t)^2} \tag{A7}$$

Density slope:

$$\frac{\partial R_o}{\partial s_i} = \frac{\partial R_o}{\partial \rho_i^t}(z_i - z_{i-1}) \tag{A8}$$

Discontinuity depths:

$$\frac{\partial R_o}{\partial z_i} = \frac{\partial R_o}{\partial \rho_i^t} s_i + \frac{\partial R_o}{\partial v_i^t} g_i \tag{A9}$$

$$\frac{\partial R_o}{\partial z_{i-1}} = -\frac{\partial R_o}{\partial z_i} \tag{A10}$$

Note that we have retained the shorthand for v_i^b and ρ_i^b on the right-hand side of A3-A4 and A6-A7 for convenience; A2 is simply substituted in when calculating the kernels.

Vertical Travel Time

Using the same notation as in the previous section, we can write the vertical travel time to a discontinuity at a depth z_i at the base of layer i as an integral of the vertical slowness ($1/v_{sv}$) over the depth within a layer:

$$t_v(z_i) = \int_{z_{i-1}}^{z_i} \frac{dz}{v_i^t + g_i(z - z_{i-1})} + t(z_{i-1}) \qquad \text{(A11)}$$

Solving this integral analytically, we find

$$t_v(z_i) = \frac{1}{g_i} \ln\left[\frac{g_i}{v_i^t}(z_i - z_{i-1}) + 1\right] + t(z_{i-1}) \qquad (g_i \neq 0) \qquad \text{(A12)}$$

$$t_v(z_i) = \frac{(z_i - z_{i-1})}{v_i^t} + t(z_{i-1}) \qquad (g_i = 0)$$

We can differentiate these equations with respect to the model parameters to determine the four partial derivatives for each observed vertical travel time to a discontinuity.

Velocity intercepts:

$$\frac{\partial t_v}{\partial v_i^t} = \frac{-(z_i - z_{i-1})}{v_i^t g_i (z_i - z_{i-1}) + v_i^{t2}} \qquad \text{(A13)}$$

Velocity slope:

$$\frac{\partial t_v}{\partial g_i} = \frac{-1}{g_i^2} \ln\left[\frac{g_i}{v_i^t}(z_i - z_{i-1}) + 1\right] + \frac{1}{g_i}\left(\frac{(z_i - z_{i-1})}{g_i(z_i - z_{i-1}) + v_i^t}\right) \qquad (g_i \neq 0) \qquad \text{(A14)}$$

$$\frac{\partial t_v}{\partial g_i} = \frac{-(z_i - z_{i-1})^2}{2v_i^{t2}} \qquad (g_i = 0)$$

Discontinuity depths:

$$\frac{\partial t_v}{\partial z_i} = \frac{1}{g_i(z_i - z_{i-1}) + v_i^t} \qquad \text{(A15)}$$

$$\frac{\partial t_v}{\partial z_{i-1}} = -\frac{\partial t_v}{\partial z_i} \qquad \text{(A16)}$$

GSDF FRÉCHET KERNELS IN RADIALLY ANISOTROPIC MEDIA

Gee and Jordan [1992] describe the formulation of the partial derivative kernels for frequency dependent phase delays. The process involves a weighted sum of the normal mode Fréchet kernels, the weighting depending on the modes incorporated in the isolation filter, other interfering modes, the mode excitation of the source, and the frequency response of the receiver and any subsequent filtering. For an isotropic media, the phase delay at a center frequency $\tilde{\omega}_s$ can be approximated as [*Gee and Jordan*, 1992]

$$\delta\tau_p(\tilde{\omega}_s) \approx \sum_{n=1}^{N} c_n \int_0^1 g_p^n(\tilde{\omega}_s, r)\delta m(r) r^2 dr \tag{A16}$$

where c_n represents a weighting coefficient for the nth normal mode branch, δm represents the perturbations of isotropic velocity parameters (i.e. v_S, v_P, and ρ, and depths of discontinuities), and g_p^n represents the Fréchet kernels for an eigenfrequency perturbation due to these parameter perturbations [*Woodhouse and Dahlen*, 1978]. This formalism can be extended to radially anisotropic media by incorporating a source excitation for an anisotropic media, and simply replacing the isotropic normal mode Fréchet kernels with the appropriate kernels for an anisotropic structure. These kernels are generally available in the literature for a variety of choices of parameterization for transversely isotropic media [e.g. *Dziewonski and Anderson*, 1981; *Anderson and Dziewonski*, 1982; *Woodhouse and Dziewonski*, 1984], but we summarize them here for our parameterization for completeness.

For a transversely isotropic model, perturbations to eigenfrequency ω due to perturbations in discontinuity depths and radial velocity and density can be written as

$$\begin{aligned}\frac{\delta\omega}{\omega} = &\int_0^1 [\delta\rho R' + \delta A\overline{A} + \delta C\overline{C} + \delta L\overline{L} + \delta N\overline{N} + \delta F\overline{F}] r^2 dr \\ &- \sum_d r^2 h[\rho R' + A\overline{A} + C\tilde{C} + L\tilde{L} + N\overline{N} + F\tilde{F}]_-^+\end{aligned} \tag{A17}$$

where the integral term accounts for perturbations to the velocity and density as a function of depth ($\delta\rho$, δA, etc.), and the summation accounts for perturbations h to each discontinuity d [*Woodhouse and Dziewonski*, 1984]. This form employs *Love's* [1927] notation (A, C, F, L, N) for transverse isotropy, which is not particularly convenient for our purposes. We relate Love's parameterization to the one employed in our models [e.g. *Dziewonski and Anderson*, 1981]:

$$\begin{aligned} A &= \rho v_{PH}^2 & C &= \rho v_{PV}^2 \\ L &= \rho v_{SV}^2 & N &= \rho v_{SH}^2 \\ F &= \eta\rho(v_{PH}^2 - 2v_{SV}^2) \end{aligned} \tag{A18}$$

Differentiating the expressions in A18, we can rewrite A17 as

$$\begin{aligned} \frac{\delta\omega}{\omega} = &\int_0^1 [\delta\rho\overline{R} + \delta v_{PH}\overline{P}_H + \delta v_{PV}\overline{P}_V + \delta v_{SH}\overline{S}_H + \delta v_{SV}\overline{S}_V + \delta\eta\overline{E}]r^2 dr \\ &- \sum_d r^2 h\rho[R' + v_{PH}^2\overline{A} + v_{PV}^2\tilde{C} + v_{SV}^2\tilde{L} + v_{SH}^2\overline{N} + \rho\eta(v_{PH}^2 - 2v_{SV}^2)]_-^+ \end{aligned} \tag{A19}$$

This specifies the perturbation to a mode eigenfrequency in terms of perturbations to model parameters $\delta\rho$, δv_{PV}, etc. The volumetric kernel functions ($\overline{P}_V$, $\overline{S}_H$, etc) are expressed in terms of the kernels in the Love notation:

$$\begin{aligned} \overline{P}_H &= 2\rho v_{PH}(\overline{A} + \eta\overline{F}) \\ \overline{P}_V &= 2\rho v_{PV}\overline{C} \\ \overline{S}_H &= 2\rho v_{SH}\overline{N} \\ \overline{S}_V &= 2\rho v_{SV}(\overline{L} - 2\eta\overline{F}) \\ \overline{E} &= \rho(v_{PH}^2 - 2v_{SV}^2)\overline{F} \\ \overline{R} &= \tfrac{1}{2}[R' + v_{PH}^2(\overline{A} + \eta\overline{F}) + v_{PV}^2\overline{C} + v_{SV}^2(\overline{L} - 2\eta\overline{F}) + v_{SH}^2\overline{N}] \end{aligned} \tag{A20}$$

The Love-notation kernels for volumetric heterogeneity ($\overline{C}$, $\overline{L}$, etc.) are written in terms of the mode eigenfunctions U, V, W, and their radial partial derivatives ($\partial/\partial r$, specified by a

dot) for radially anisotropic media [*Takeuchi and Saito*, 1972; *Dziewonski and Anderson*, 1981; *Anderson and Dziewonski*, 1982]. Using the eigenfunction normalization

$$\omega^2 \int_0^a \rho[U^2 + l(l+1)V^2 + l(l+1)W^2]r^2 dr = 1$$

the spheroidal-mode kernels can be expressed as:

$$\begin{aligned}
\overline{C} &= \dot{U}^2 \\
\overline{A} &= r^{-2}[2U - l(l+1)V]^2 \\
\overline{F} &= 2r^{-1}\dot{U}[2U - l(l+1)V] \\
\overline{L} &= l(l+1)[\dot{V} + (U-V)/r]^2 \\
\overline{N} &= r^{-2}\{(l+2)(l+1)l(l-1)V^2 - [2U - l(l+1)V]^2\}
\end{aligned} \tag{A21}$$

For toroidal modes,

$$\begin{aligned}
\overline{L} &= l(l+1)[\dot{W} - W/r]^2 \\
\overline{N} &= (l+2)(l+1)l(l-1)[W/r]^2 \\
\overline{A} &= \overline{C} = \overline{F} = 0
\end{aligned} \tag{A22}$$

The remaining kernels for the discontinuity perturbations are specified by *Woodhouse and Dziewonski* [1984]. For spheroidal modes,

$$\begin{aligned}
\tilde{C} &= \overline{C} - 2\dot{U}^2 \\
\tilde{F} &= \overline{F} - 2r^{-1}\dot{U}[2U - l(l+1)V] \\
\tilde{L} &= \overline{L} - 2l(l+1)\dot{V}[\dot{V} + (U-V)/r]
\end{aligned} \tag{A23}$$

For toroidal modes,

$$\begin{aligned}
\tilde{L} &= \overline{L} - 2l(l+1)\dot{W}[\dot{W} - W/r] \\
\tilde{C} &= \tilde{F} = 0
\end{aligned} \tag{A24}$$

The density kernel R' is unchanged from the isotropic case [*Backus and Gilbert*, 1967].

In practice, the Fréchet kernels in equation A20 are calculated as a function of depth for all normal modes with eigenfrequencies < 50 mHz, using equations A21-A24. These

kernels then form the basis for the weighted sums over mode branches for the modes selected in a given isolation filter. The result is a partial derivative (such as those presented in Chapters 2 and 4) that is tuned to explicitly represent the structural sensitivity (including sensitivity to discontinuities) of a chosen phase on the seismogram.

We have tested the accuracy of the linear perturbation theory by using the Fréchet kernels (equation A19) to predict an eigenfrequency perturbation for several input model perturbations, and comparing them to the forward-calculated eigenfrequencies. In general, velocity perturbations of ±3% in the upper mantle are quite linear: errors in $\delta\omega$ are of order 5%. Similar errors in $\delta\omega$ are found for discontinuity perturbations of less than 10 km. Larger discontinuity perturbations (for example the perturbation of lid thickness from 100 km to 70 km) are quite non-linear. Perturbations of this magnitude necessitate the iteration process used in our study.

REFERENCES

Adams, R.D., Early reflections of *P'P'* as an indication of upper mantle structure, *Bull. Seism. Soc. Am., 58,* 1933-1947, 1968.

Anderson, D.L., Elastic wave propagation in layered anisotropic media, *J. Geophys. Res., 66,* 2953-2963, 1961.

Anderson, D.L., The deep structure of continents, *J. Geophys. Res., 84,* 7555-7560, 1979.

Anderson, D.L., *Theory of the Earth,* 366 pp., Blackwell Scientific, Boston, MA, 1989.

Anderson, D.L. and A.M. Dziewonski, Upper mantle anisotropy: evidence from free oscillations, *Geophys. J. R. astr. Soc., 69,* 383-404, 1982.

Ando, M., Y. Ishikawa, and F. Yamazaki, Shear wave polarization-anisotropy in the upper mantle beneath Honshu, Japan, *J. Geophys. Res., 88,* 5850-5864, 1983.

Backus, G.E., Long-wave elastic anisotropy produced by horizontal layering, *J. Geophys. Res., 67,* 4427-4440, 1962.

Backus, G.E., Possible forms of seismic anisotropy of the uppermost mantle under oceans, *J. Geophys. Res., 70,* 3429-3439, 1965.

Bass, J.D. and D.L. Anderson, Composition of the upper mantle: Geophysical tests of two petrological models, *Geophys. Res. Lett., 11,* 237-240, 1984.

Bina, C.R., Mantle discontinuities, *Rev. Geophys., Supp,* 783-793, 1991.

Bock, G., Sp phases from the Australian upper mantle, *Geophys. J. 94,* 73-81, 1988.

Bock, G., Long-period *S* to *P* converted waves and the onset of partial melting beneath Oahu, Hawaii, *Geophys. Res. Lett., 18,* 869-872, 1991.

Bock, G., Synthetic seismogram images of upper mantle structure: No evidence for a 520-km discontinuity, *Geophys. Res., 99,* 15,843-15,851, 1994.

Boore, D. Effect of higher mode contamination on measured Love wave phase velocities, *J. Geophys. Res., 74,* 6612, 1969.

Boullier, A.M. and A. Nicolas, Classification of textures and fabrics of peridotite xenoliths from South African Kimberlites, *Phys. Chem. Earth* **9**, 467, 1975.

Bowman, J.R. and B.L.N. Kennett, An investigation of the upper mantle beneath northwestern Australia using a hybrid seismograph array, *Geophys. J. Int, 101,* 411-424, 1990.

Bowman, J.R. and B.L.N. Kennett, The velocity structure of the Australian shield from seismic travel times, *Bull. Seism. Soc. Am., 83,* 25-37, 1993.

Cara, M. and J.J. Lévêque, Oriented olivine crystals in the upper mantle: a test from the inversion of multimode surface-wave data, *Phys. Earth Planet. Int, 47,* 246-252, 1987.

Cara, M. and J.J. Lévêque, Anisotropy of the asthenosphere: the higher mode data of the Pacific revisited, *Geophys. Res. Lett., 15,* 205-208, 1988.

Carlson, R.L. and H.P. Johnson, On modeling the thermal evolution of the oceanic upper mantle: An assessment of the cooling plate model, *J. Geophys. Res, 99,* 3201-3214, 1994.

Cipar, J. J., K. Priestley, A. V. Egorkin, and N. I. Pavlenkova, The Yamal Peninsula-Lake Baikal deep seismic sounding profile, *Geophys. Res. Lett., 20,* 1631-1634, 1993.

Christensen, N.I. and M.H. Salisbury, Seismic anisotropy in the oceanic upper mantle: evidence from the Bay of Islands ophiolite complex, *J. Geophys. Res, 84,* 4601-4610, 1979.

Christensen, N.I. and J.D. Smewing, Geology and seismic structure of the norhtern section of the Oman ophiolite, *J. Geophys. Res, 86,* 2545-2555, 1981.

Cummins, P.R., B.L.N. Kennett, J.R. Bowman, and M.G. Bostock, The 520 km discontinuity?, *Bull. Seismol. Soc. Am., 82,* 323-336, 1992.

DeMets, C., R.G. Gordon, D.F. Argus, and S. Stein, Current plate motions, *Geophys. J. Int., 101,* 425-478, 1990.

Drummond, A.J., K.J. Muirhead, and A.L. Hales, Evidence for a seismic discontinuity near 200 km depth under a continental margin, *Geophys. J. R. Astron. Soc., 70,* 67-77, 1982.

Duffy, T.S. and D.L. Anderson, Seismic velocities in mantle minerals and the mineralogy of the upper mantle, *J. Geophys. Res., 94,* 1895-1912, 1989.

Dziewonski, A.M., Mapping the lower mantle: Determination of lateral heterogeneity in *P* wave velocity up to degree and order 6, *J. Geophys. Res., 89,* 5929-5952, 1984

Dziewonski, A.M. and D.L. Anderson, Preliminary reference Earth model, *Phys. Earth Planet. Inter., 25,* 297-356, 1981.

Ellis R.M., and D. Denham, Structure of the crust and upper mantle beneath Australia from Rayleigh- and Love-wave observations, *Phys. Earth Planet. Inter., 38,* 224-234, 1985.

Estey, L.H. and B.J. Douglas, Upper mantle anisotropy: a preliminary model, *J. Geophys. Res., 91,* 11,393-11,406, 1986.

Farra, V. and L. Vinnik, Shear-wave splitting in the mantle of the Pacific, *Geophys. J. Int., 119,* 195-218, 1994.

Finnerty, A.A. and F.R. Boyd, Thermobarometry for garnet peridotites: basis for the determination of thermal and compositional structure of the upper mantle, in *Mantle Xenoliths*, P. H. Nixon, Ed. (Wiley-Interscience, Chichester, 1987), pp. 381-402.

Forsyth, D.W., The early structural evolution and anisotropy of the oceanic upper mantle, *Geophys. J. R. astr. Soc., 43,* 103-162, 1975a.

Forsyth, D.W., A new method for the analysis of multi-mode surface-wave dispersion: Application to Love-wave propagation in the east Pacific, *Bull. Seism. Soc. Am., 65,* 323-342, 1975b.

Forsyth, D.W., The evolution of the upper mantle beneath mid-ocean ridges, *Tectonophysics, 38,* 89-118, 1977.

Francis, T.J.G., Generation of seismic anisotropy along the mid-oceanic ridges, *Nature, 221,* 162-165, 1969.

Fuchs, K., and K. Schulz, Tunneling of low-frequency waves through the subcrustal lithosphere, *J. Geophys., 42,* 175-190, 1976.

Gaherty, J.B., T.H. Jordan, and L.S. Gee, Relating upper-mantle discontinuities and anisotropy: inversion of phase-delay and *ScS*-reverberation data (abstract), *Eos Trans. Amer. Geophys. Union, 73,* No. 43 supplement, 523, 1992.

Gaherty, J.B. and T.H. Jordan, Lehmann discontinuity as the base of an anisotropic layer beneath continents, *Science*, in press, 1995.

Gao, S., P.M. Davis, H. Liu, P.D. Slack, Y.A. Zorin, V.V. Mordvinova, V.M. Kozhevnikov, and R.P. Meyer, Seismic anisotropy and mantle flow beneath the Baikal rift zone, *Nature, 371*, 149-151, 1994.

Gee, R.D., Structure and tectonic style of the western Australian shield, *Tectonophysicis, 58*, 327-369, 1979.

Gee, L.S., A travel-time anomaly in the western Pacific, *Geophys. Res. Lett.*, submitted, 1994.

Gee, L.S. and T.H. Jordan, Polarization anisotropy and fine-scale structure of the Eurasian upper mantle, *Geophys. Res. Lett.*, *15*, 824-827, 1988.

Gee, L. S., and T. H. Jordan, Generalized seismological data functionals, *Geophys. J. Int.*, *111*, 363-390, 1992.

Grand, S.P., Tomographic inversion for shear velocity structure beneath the North America Plate, *J. Geophys. Res.*, *92*, 14,065-14,090, 1987.

Grand, S.P., Mantle shear structure beneath the Americas and surrounding oceans, *J. Geophys. Res.*, *99*, 11,591-11,621, 1994.

Grand, S.P. and D.V. Helmberger, Upper mantle shear structure of North America, *Geophys. J. R. astr. Soc.*, *76*, 399-438, 1984.

Grand, S.P. and D.V. Helmberger, Upper mantle shear structure beneath the northwest Atlantic Ocean, *J.Geophys. Res.*, *89*, 11,465-11,475, 1984.

Grand, S.P. and D.V. Helmberger, Upper mantle shear structure beneath Asia from multi-bounce *S* waves, *Phys. Earth Planet. Int.*, *41*, 154-169, 1985.

Green, H.W. and Y. Gueguen, Origin of kimberlite pipes by diapiric upwelling in the upper mantle, *Nature, 249*, 617-620, 1974.

Gripp, A.E. and R.G. Gordan, Current plate velocities relative to the hotspots incorporating the NUVEL-1 global plate motion model, *Geophys. Res. Lett, 17*, 1109-1112, 1990.

Gudmundsson, O., B.L.N. Kennett, A. Goody, Broadband observations of upper-mantle seismic phases in northern Australia and the attenuation structure in the upper mantle, *Phys. Earth Planet Inter. 84*, 207, 1994.

Gutenberg, B., *Physics of the Earth's Interior*, 240 pp., Academic Press, New York, 1959.

Hager, B.H., R.W. Clayton, M.A. Richards, R.P. Comer, and A.M. Dziewonski, Lower mantle heterogeneity, dynamic topography and the geoid, *Nature, 313*, 541-545, 1985.

Hales, A.L., Upper mantle models and the thickness of continental lithosphere, *Geophys. J. Int. 105*, 355-363, 1991.

Hales, A.L., K.J. Muirhead, and J.M.W. Rynn, A compressional velocity distribution for the upper mantle, *Tectonophysics, 63*, 309-348, 1980.

Hess, H., Seismic anisotropy of the uppermost mantle under oceans, *Nature, 203*, 629, 1964.

Hirth, G. and D.L. Kohlstedt, Experimental constraints on the dynamics of the partially molten upper mantle: Deformation in the diffusion creep regime, *J. Geophys. Res.*, *100*, 1981-2001, 1995.

Inoue, H., Y. Fukao, K. Tanabe, and Y. Ogata, Whole mantle P-wave travel-time tomography, *Phys. Earth Planet. Inter., 59*, 294-328, 1990.

Ita, J. and L. Stixrude, Petrology, elasticity, and composition of the mantle transition zone, *J. Geophys. Res.*, **97**, 6849-6866, 1992.

James, D.E., Anomalous Love wave phase velocities, *J. Geophys. Res., 76,* 2077-2083, 1971.

Jones, L.E., J. Mori, and D.V. Helmberger, Short-period constraints on the proposed transition zone discontinuity, *J. Geophys. Res., 97,* 8765-8774, 1992.

Jordan, T.H., The continental tectosphere, *Rev. Geophys., 13*, 1-12, 1975.

Jordan, T.H., Global tectonic regionalization for seismological data analysis, *Bull. Seism. Soc. Am., 71,* 1131-1141, 1981

Jordan, T. H., Structure and formation of the continental tectosphere, *J. Petrology Special Lithosphere Issue* , 11-37, 1988.

Jordan, T.H. and L. N. Frazer, Crustal and upper mantle structure from Sp phases, *J. Geophys. Res., 80,* 1504-1518, 1975.

Jordan, T.H. and J.B. Gaherty, Polarization anisotropy and small-scale structure of continental upper mantle, in *Proceedings of the 16th Annual Seismic Research Symposium*, J.J. Cipar, J.F. Lewkowicz, J.M. McPhetres, Eds., (Phillips Laboratory Technical Report PL-TR-94-2217, Hanscom A.F.B., MA), pp. 189-195, 1994.

Jordan, T.H., A.L. Lerner-Lam, and K.C. Creager, Seismic imaging of boundary layers and deep mantle convection, in *Mantle Convection*, W. R. Peltier, Ed. (Gordon and Breach, New York, 1989), pp. 98-201, 1989.

Karato, S.-I., Seismic anisotropy due to lattice preferred orientation of minerals: kinematic or dynamic?, In *High Pressure Research in Mineral Physics*, M.H. Manghnani and Y. Syono, Eds., (Am. Geophys. Union, Washington, DC, 1987), pp. 455-471, 1987.

Karato, S.-I., On the Lehmann discontinuity, *Geophys. Res. Lett.* **19**, 2255-2258, 1992.

Karato, S.-I. and P. Wu, Rheology of the upper mantle: A synthesis, *Science, 260,* 771-778, 1993.

Karato, S.-I, S.S. Paterson, and J.D. Fitz Gerald, Rheology of synthetic olivine aggregates: Influence of grain size and water, *J. Geophys. Res, 91*, 8151-8176, 1986.

Katzman, R. and T.H. Jordan, Seismic tomography using *ScS* reverberations, IUGG meeting abstract, submitted, 1995.

Kawasaki, I., and F. Kon'no, Azimuthal anisotropy of surface waves and the possible type of the seismic anisotropy due to preferred orientation of olivine in the uppermost mantle beneath the Pacific Ocean, *J. Phys. Earth, 32,* 229-244, 1984.

Kennett, B.L.N., O. Gudmundsson, and C. Tong, The upper mantle S and P velocity structure beneath northern Australia from broad-band observations, *Phys. Earth Planet. Inter.*, in press, 1994.

Kern, H., P- and S-wave anisotropy and shear-wave splitting at pressure and temperature in possible mantle rocks and their relationship to the rock fabric, *Phys. Earth Planet. Inter., 87,* 245-256, 1993.

Kirby, S.H. and A.K. Kronenberg, Rheology of the lithosphere: Selected topics, *Reviews of Geophysics, 25*, 1219-1244, 1987.

Kirkwood, S. and S. Crampin, Surface-wave propagation in an ocean basin with an anisotropic upper mantle: Observations of polarization anomalies, *Geophys. J. R. Astron . Soc., 64,* 487-497, 1981a.

Kirkwood, S. and S. Crampin, Surface-wave propagation in an ocean basin with an anisotropic upper mantle: Numerical modeling, *Geophys. J. R. Astron . Soc., 64,* 463-485, 1981b.

Kuo, B.-Y. and D.W. Forsyth, A search for split SKS waveforms in the North Atlantic, *Geophys. J. Int, 108,* 557-574, 1992.

Kuo, B.-Y., D.W. Forsyth, and M. Wysession, Lateral heterogeneity and azimuthal anisotropy in the North Atlantic determined from SS-S differential travel times, *J. Geophys. Res.,* 92, 6421-6436, 1987.

Larson, R.L., Latest pulse of the Earth: Evidence for a mid-Cretaceous super plume, *Geology, 19,* 547-550, 1991.

Lerner-Lam, A.L. and T.H. Jordan, How thick are the continents?, *J. Geophys. Res., 92,* 14007-14026, 1987.

Lehmann, I., Velocities of longitudinal waes in the upper part of the Earth's mantle, *Ann. Géophys., 15,* 93-118, 1959.

Lehmann, I., *S* and the structure of the upper mantle, *Geophys. J. R. Astron. Soc., 4,* 124-138, 1961.

Lévêque, J.J. and M. Cara, Long-period Love wave overtone data in North America and the Pacific Ocean: new evidence for upper mantle anisotropy, *Phys. Earth Planet. Inter., 33,* 164-179, 1983.

Lévêque, J.J. and M. Cara, Inversion of multimode surface wave data: evidence for sub-lithospheric anisotropy, *Geophys. J. R. astr. Soc., 83,* 753-773, 1985.

Leven, J.H., The application of synthetic seismograms to the interpretation of the upper mantle P wave velocity structure in northern Australia, *Phys. Earth Planet. Inter., 38,* 9-27, 1985.

Leven, J.H., I. Jackson, A. E. Ringwood, Upper mantle seismic anisotropy and lithospheric decoupling, *Nature, 289,* 234-239, 1981.

Love, A.E.H., *A Treatise on the Mathematical Theory of Elasticity,* Cambridge University Press, Cambridge, 1927.

Ludwig, W.J. and R.E. Houtz, Isopach map of sediments in the Pacific ocean basin and marginal sea basins, Amer. Assoc. Petrol. Geol., Tulsa, Okla., 1979.

Mainprice, D. and P. G. Silver, Interpretation of SKS-waves using samples from the subcontinental lithosphere,*Phys. Earth Planet. Inter. 78,* 257-280, 1993.

Maupin, V., Partial derivatives of surface-wave phase velocities for flat anisotropic models, *Geophys. J. R. astr. Soc., 83,* 379-398, 1985.

McEvilly, T.V., Central US crust-upper mantle structure from Love and Rayleigh wave phase velocity inversion, *Bull. Seis. Soc. Am., 54,* 1997-2015, 1964.

McKenzie, D., Finite deformation during fluid flow, *Geophys. J. R. astr. Soc., 58,* 689-715, 1979.

McNamara, D.E., T.J. Owens, P.G. Silver, and F.T. Wu, Shear wave anisotropy beneath the Tibetan Plateau, *J. Geophys. Res., 99,* 13,655-13,665, 1994.

McNutt, M.K., Marine geodynamics: Depth-age revisited, *Rev. Geophys., Suppl.*, submitted, 1994.

McNutt, M.K. and K.M. Fischer, The south Pacific superswell, in *Seamounts, Islands, and Atolls*, B.H. Keating, P.Fryer, R. Batiza, G.W. Boehlert, Eds. (Geophysical Monograph 43, American Geophysical Union, Washington, DC), 969-975, 1987.

Menard, H.W., Darwin reprise, *J. Geophys. Res., 89,* 9960-9968, 1984.

Menke, W., *Geophysical Data Analysis: Discrete Inverse Theory,* 2nd Edition, 289 p., Academic Press, San Diego, 1989.

Minster, J.B. and T.H. Jordan, Present day plate motions, *J. Geophys. Res., 83,* 5331-5354, 1978.

Mitchell, B.J., On the inversion of Love and Rayleigh wave dispersion and implications for Earth structure and anisotropy, *Geophys. J. R. Astr. Soc., 76,* 233-241, 1984.

Montagner, J.-P., Regional three-dimensional structures using long-period surface waves, *Ann. Geophys. Ser. B, 4*, 283-294, 1986.

Montagner, J.-P. and D.L. Anderson, Petrological constraints on seismic anisotropy, *Phys. Earth Planet. Inter., 54,* 82-105, 1989.

Montagner, J.-P. and N. Jobert, Vectorial tomography, II, Application to the Indian Ocean, *Geophys. J. R. Astron. Soc., 94*, 309-344, 1988.

Montagner, J.-P. and H.C. Nataf, A simple method for inverting the azimuthal anisotropy of surface waves, *J. Geophys. Res., 91,* 511-520, 1986.

Montagner, J.-P. and H.C. Nataf, Vectorial Tomography, I, Theory, *Geophys. J. R. Astron. Soc., 94*, 295-307, 1988.

Montagner, J.-P. and T. Tanimoto, Global anisotropy in the upper mantle inferred from the regionalization of the phase velocities, *J. Geophys. Res., 95,* 4797-4819, 1990.

Montagner, J.-P. and T. Tanimoto, Global upper-mantle tomography of seismic velocities and anisotropy, *J. Geophys. Res., 96,* 20,337-20,351, 1991.

Mueller, R.D., Roest, W.R., Royer, J.-Y., Gahagan, L.M., and Sclater, J.G., A digital age map of the ocean floor, *SIO Reference Series 93-30*, 1993.

Nataf, H.-C., I. Nakanishi, and D.L. Anderson, Measurements of mantle-wave velocities and inversino for lateral heterogeneities and anisotropy, 3. Inversion, *J. Geophys. Res., 91,* 7261-7307, 1986.

Nicolas, A. and N.I. Christensen, Formation of anisotropy in upper mantle peridotites: A review, in *Composition, Structure, and Dynamics of Lithosphere-Asthenosphere Systerm, Geodyn. Ser.,* vol. 16, edited by K. Fuchs and C. Froidevaux, pp. 111-123, AGU, Washington, D.C., 1987.

Nicolas, A., F. Boudier, and A.M. Boullier, Mechanisms of flow in naturally and experimentally deformed peridotites, *Am. J. Sci., 280,* 853-876, 1973.

Nishimura, C.E. and D.W. Forsyth, Rayleigh wave phase velocities in the Pacific with implications for azimuthal anisotropy and lateral heterogeneities, *Geophys. J., 94,* 479-501, 1988.

Nishimura, C.E. and D.W. Forsyth, The anisotropic structure of the upper mantle in the Pacific, *Geophys. J., 96,* 203-229, 1989.

Nolet, G., S.P. Grand, and B.L.N. Kennett, Seismic heterogeneity in the upper mantle, *J.Geophys. Res., 99,* 23,753-23,766, 1994.

Parsons, B. and J. Sclater, An analysis of the variation of ocean bathymetry and heat flow with age, *J. Geophys. Res., 82,* 803-827, 1977.

Parsons, B. and D. McKenzie, Mantle convection and the thermal structure of the plates, *J. Geophys. Res., 83,* 4485-4496, 1978.

Peselnick, L. and A. Nicolas, Seismic anisotropy in an ophiolite peridotite: application to oceanic upper mantle, *J. Geophys. Res., 83,* 1227-1235, 1978.

Plumb, K.A., Structure and tectonic style of the Precambrian shields and platforms of northern Australia, *Tectonophysicis, 58,* 291-325, 1979.

Pulliam, R.J., D. Vasco, and L. Johnson, Tomographic inversions for mantle wave velocity structure based in the minimization of L^2 and L^1 norm of International Seismological Centre travel time residuals, *J. Geophys. Res., 98,* 699-734, 1993.

Raitt, R.W., G.G. Shor, T.J. Francis, and G.B. Morris, Anisotropy of the Pacific upper mantle, *J. Geophys. Res., 74,* 3095-3109, 1969.

Regan, J. and D.L. Anderson, Anisotropic models of the upper mantle, *Phys. Earth Planet. Int., 35,* 227-263, 1984.

Revenaugh, J. S., and T. H. Jordan, Observations of first-order mantle reverberations, *Bull. Seis Soc. Am., 77,* 1704-1717, 1987.

Revenaugh, J. S., and T. H. Jordan, A study of mantle layering beneath the western Pacific, *J. Geophys. Res., 94,* 5787-5813, 1989.

Revenaugh, J.S. and T.H. Jordan, Mantle layering from *ScS* reverberations, 1, waveform inversion of zeroth-order reverberations, *J. Geophys. Res., 96,* 19,749-19,762, 1991a.

Revenaugh, J.S. and T.H. Jordan, Mantle layering from *ScS* reverberations, 2, The transition zone, *J. Geophys. Res., 96,* 19,763-19,780, 1991b.

Revenaugh, J.S. and T.H. Jordan, Mantle layering from *ScS* reverberations, 3, The upper mantle, *J. Geophys. Res., 96,* 19,781-19,810, 1991c.

Revenaugh, J.S. and T.H. Jordan, Mantle layering from *ScS* reverberations, 4, The lower mantle and core-mantle boundary, *J. Geophys. Res., 96,* 19,811-19,824, 1991d.

Revenaugh, J. and S. A. Sipkin, Mantle discontinuity structure beneath China, *J. Geophys. Res. 99,* 21911-21,927, 1994.

Ribe, N.M., Seismic anisotropy and mantle flow, *J. Geophys. Res., 94,* 4213-4223, 1989.

Ribe, N.M., On the relation between seismic anisotropy and finite strain, *J. Geophys. Res., 97,* 8737-8747, 1992.

Rigden, S.M., G.D. Gwanmesia, J.D. Fitzgerald, I. Jackson, and R.C. Lieberman, Spinel elasticity and the seismic structure of the transition zone of the mantle, *Nature, 345,* 143-145, 1991.

Ringwood, A.E., *Composition and Petrology of the Earth's Mantle,* 604 pp., McGraw-Hill, New York, 1975.

Russo, R.M., and P.G. Silver, Trench-parallel flow beneath the Nazca plate from seismic anisotropy, *Science, 263,* 1,105-1,111, 1994.

Rutland, R.W.R., Structural framework of the Australian Precambrian, in *Precambrian of the Southern Hemisphere*, D. R. Hunter, Ed. (Elsevier, Amsterdam, 1981), pp. 1-32], 1981.

Ryberg, T., K. Fuchs, A.V. Egorkin, and L. Solodilov, Observation of high-frequency teleseismic P_n waves on the long-range Quartz profile across northern Eurasia, *J. Geophys. Res,* submitted, 1995.

Sato, H., I.S. Sacks, T. Murase, G. Muncill, and H. Fukuyama, *Qp*-melting temperature relation in peridotite at high pressure and temperature: attenuation mechanism and implications for the mechanical properties of the upper mantle, *J. Geophys. Res, 94,* 10,647-10,661, 1989.

Schlue, J. W. and L. Knopoff, Shear-wave polarization anisotropy in the Pacific basin, *Geophys. J. R. astr. Soc., 49,* 145-165, 1977.

Schubert, G., C. Froidevaux, and D.A. Yuen, Oceanic lithosphere and asthenosphere: Thermal and mechanical structure, *J. Geophys. Res., 81,* 3525-3540, 1976.

Shapiro, S.S., B.H. Hager, and T.H. Jordan, Surface tectonics and upper-mantle shear-wave heterogeneity, *Geophys. Res. Lett., submitted,* 1995.

Shearer, P.M., Seismic imaging of upper mantle structure with new evidence for a 520-km discontinuity, *Nature, 344,* 121-126, 1990.

Shearer, P.M. and J.A. Orcutt, Compressional and shear wave anisotropy in the oceanic lithosphere -- the Ngendei seismic refraction experiment, *Geophys. J. R. Astr. Soc, 87,* 967-1003, 1986.

Shearer, P.M., Global mapping of upper mantle reflectors from long-period *SS* precursors, *Geophys. J. Int, 115,* 878-904, 1993.

Sheehan, A.F. and S.C. Solomon, Joint inversion of shear wave travel time residuals and geoid and depth anomalies for long-wavelength variations in upper mantle temperature and composition along the mid-Atlantic ridge, *J. Geophys. Res., 96,* 19,981-20,009, 1991.

Shimamura, H., Anisotropy in the oceanic lithosphere of the northwestern Pacific basin, *Geophys. J. R. Astr. Soc, 76,* 253-260, 1984.

Shimamura, H., T. Asada, and M. Kumazawa, High shear velocity layer in the upper mantle of the Western Pacific, *Nature, 269,* 680-681, 1977.

Silver, P.G. and W.W. Chan, Shear wave splitting and subcontinental mantle deformation, *J. Geophys. Res., 96,* 16,429-16,454, 1991.

Silver, P.G. and S. Kaneshima, Constraints on mantle anisotropy beneath precambrian North America from a transportable teleseismic experiment, *Geophys. Res. Lett, 20,* 1127-1130, 1993.

Sipkin, S.A., and T.H. Jordan, Lateral heterogeneity of the upper mantle determined from the travel times of multiple *ScS, J. Geophys. Res., 81,* 6307-6320, 1976.

Sipkin, S.A., and T.H. Jordan, Multiple *ScS* travel times in the western Pacific: Implications for mantle heterogeneity, *J. Geophys. Res., 85,* 853-861, 1980a.

Sipkin, S.A., and T.H. Jordan, Regional variation of Q_{ScS}, *Bull. Seismol. Soc. Am., 70,* 1071-1102, 1980b.

Smith, M.L. and F.A. Dahlen, The azimuthal dependence of Love and Rayleigh wave propagation in a slightly anisotropic medium, *J. Geophys. Res., 78,* 3321-3333, 1973.

Spence, D.A. and D. L. Turcotte, Buoyancy-driven magma fracture: A mechanism for ascent through the lithosphere and the emplacement of diamonds, *J. Geophys. Res. 95,* 5133-5139, 1990.

Stein, C.A. and S. Stein, A model for the global variation in oceanic depth and heat flow with lithospheric age, *Nature, 359*, 123-129, 1992.

Su, L., and J. Park, Anisotropy and the splitting of PS waves, *Phys. Earth Planet. Inter., 87*, in press, 1994.

Su, W.-J., R.L. Woodward, and A.M. Dziewonski, Deep origin of mid-ocean-ridge seismic velocity anomalies, *Nature, 359*, 149-152, 1992.

Su, W.-J., R.L. Woodward, and A.M. Dziewonski, Degree 12 model of shear velocity heterogeneity in the mantle, *J. Geophys. Res., 99*, 6945-6980, 1994.

Suetsugu D., and I. Nakanishi, Tomographic inversion and resolution for Rayleigh wave phase velocities in the Pacifi Ocean, *J. Phys. Earth, 33*, 345-368, 1985.

Suetsugu D., and I. Nakanishi, Regional and azimuthal dependence of phase velocities of mantgle Rayleigh waves in the Pacific Ocean, *Phys. Earth Planet. Inter., 47*, 230-245, 1987.

Takeuchi H. and M. Saito, Seismic surface waves, *Methods Comput. Phys., 11, 217-295*, 1972.

Tanimoto, T., Free oscillation in a slightly anisotropic Earth, *Geophys. J. R. Astron. Soc., 100*, 327-336, 1990.

Tanimoto, T. and D.L. Anderson, Lateral heterogeneity and azimuthal anisotropy in the upper mantle: Love and Rayleigh waves 100-250 s, *J. Geophys. Res., 90*, 1842-1858, 1990.

Tarantola, A., *Inverse Problem Theory*, 613 p., Elsevier, New York, 1987.

Tarantola, A. and B. Valette, Generalized nonlinear inverse problems solved using the least squares criterion, *Revs. Geophys. Space Phys., 20*, 219-232, 1982.

Tong C., O. Gudmundsson, B.L.N. Kennett, Shear-waves splitting in refracted waves returned from the upper mantle transition zone beneath northern Australia, *J. Geophys. Res. 99*, 15,783-15,799, 1994.

Vidale, J.E. and H.M. Benz, Upper-mantle seismic discontinuities and the thermal structure of subduction zones, *Nature, 356*, 678-683, 1992.

Vinnik, L.P., L.I. Makeyeva, A. Milev, and A.Y. Usenko, Global patterns of azimuthal anisotropy and deformations in the continental mantle, *Geophys. J. Int., 111*, 433-447, 1992.

Vinnik, L.P., R.W.E. Green, and L.O. Nicolaysen, Recent deformations of the deep continental root beneath southern Africa, *Nature, 375*, 50-52, 1995.

Walck, M., The P-wave upper mantle structure beneath an active spreading centre: the Gulf of California, *Geophys. J. R. Astron. Soc., 76*, 697-723, 1984.

Walker, D.A., High-frequency *Pn* and *Sn* phases recorded in the western Pacific, *J. Geophys. Res., 82*, 3350-3360, 1977.

Weidner, D., A mineral physics test of a pyrolite mantle, *Geophys. Res. Lett, 12*, 417-420, 1985.

Wenk, H.-R., K. Bennett, G. Canova, and A. Molinari, Modelling plastic deformation of peridotite with the self-consistent theory, *J. Geophys. Res., 96*, 8337-8349, 1991.

Wessel, P. and W.H.F. Smith, Free software helps map and display data, *EOS Trans. Amer. Geophys. U., 72*, pp. 441, 445-446, 1991.

Whitcomb, J. and D.L. Anderson, Reflection of *P'P'* seismic waves from discontinuities in the mantle, *J. Geophys. Res., 75,* 5713-5728, 1970.

Woodhouse, J.H. and A.M. Dziewonski, Mapping the upper mantle: Three-dimensional modeling of earth structure by inversino of seismic waveforms, *J. Geophys. Res., 89,* 5953-5986, 1984.

Woodward, R.L. and G. Masters, Global upper mantle structure from long-period differential travel times, *J. Geophys. Res., 96,* 6351-6378, 1991.

Yang X., K.M. Fischer, and G.A. Abers, Seismic anisotropy beneath the Shumagin Islands segment of the Aleutian-Alaska subduction zone, *J. Geophys. Res.,* submitted, 1995.

Yu, G.K. and B.J. Mitchell, Regionalized shear velocity models of the Pacific upper mantle from observed Love and Rayleigh wave dispersion, *Geophys. J. R. astr. Soc., 57,* 311-341, 1979.

Yu, Y. and J. Park, Hunting for azimuthal anisotropy beneath the Pacific Ocean region, *J. Geophys. Res., 99,* 15,399-15,421, 1994.

Zaug, J.M., E.H. Abramson, J.M. Brown, and L.J. Slutsky, Sound velocities in olivine at Earth mantle pressures, *Science, 260,* 1487-1489, 1993.

Zhang, S. and S.-I. Karato, Lattice preferred orientation of olivine in simple shear deformation and the flow geometry of the upper mantle of the Earth, *Nature, submitted,* 1995.

Zhang, Y.-S. and T. Tanimoto, Ridges, hot spots,and their interaction as observed in seismic velocity maps, *Nature, 355,* 45-49, 1992.

Zhang, Y.-S. and T. Tanimoto, High-resolution global upper mantle structure and plate tectonics, *J. Geophys. Res., 98,* 9793-9823, 1993.

Zielhaus, A. and G. Nolet, Shear wave velocity variations in the upper mantle beneath central Europe, *Geophys. J. Int., 117,* 695-715, 1994.

ACKNOWLEDGMENTS

Over the years, I've read far more thesis acknowledgments than I've read theses. Having now completed my own thesis, it occurs to me that this is as it should be.

First, the technical details. The figures were generated using GMT [*Wessel and Smith*, 1991]. Justin Revenaugh provided the reflectivity profiles plotted in Chapters 2 and 4. Peter Puster pointed out the reference for the boundary-perturbation kernels in the Appendix, and Steve Shapiro provided the vertical travel times in Chapter 6. Professor N.I Christensen of Purdue University supplied unpublished xenolith data plotted in Figure 5.5. Seismic data was acquired from the Seismic Archive Facility at Harvard University, and from the IRIS Data Management system. IRIS also provided funding for travel to a variety of workshops and meetings. I thank Stan Dickinson and Jim Lewkowicz for their ongoing support. This research was sponsored by the Air Force Office of Scientific Research under grants F49620-92-J-0404 and F49620-95-1-0051, and by the National Science Foundation under grant EAR-9105419.

I've been extremely fortunate to have worked closely with three outstanding scientists and teachers. Tom Jordan has been a great advisor. I can only hope that I've inherited a small portion of his instinct for scientific significance. Brad Hager guided my exploration of geodynamics. Although the result of our collaboration is not incorporated in this document, my education would have been incomplete without it. Thorne Lay introduced me to the arcane world of seismic data, taught me the value of a simple waveform, and convinced me that the scientific treasures hidden within were worth the trouble.

I also thank Chris Marone, Tim Grove, and Paul Silver for reading my thesis and providing spirited discussion and useful comments and suggestions.

This work could not have been done without the assistance of Lind Gee. Lind introduced me to digital data, provided (and updated) the GSDF codes used throughout this analysis, and cheerfully (at least outwardly) waded through my text. Her contribution to this thesis (and all other work in Global Seismology at MIT) is immeasurable.

My scientific development has been enhanced by interaction with a number of people, either in class or over a beer: in particular, Chris Marone, Sam Bowring, Larry Ruff, Henry Pollack, John Vidale, Susan Schwartz, Sue Beck, Greg Hirth, Mike Gurnis, Art Lerner-Lam, and Steve Grand. Art is especially thanked for encouraging my participation in the Rocky Mt. Front experiment.

My fellow students have surely taught me more than my teachers, and detailing their contributions would only trivialize them. In short, I thank Chris Young, Anne Sheehan, Mike Bergman, Will Wilcock, Peter Puster, Pierre Ihmle, Paolo Harabaglia, Steve Shapiro, Mark Simons, Cecily Wolfe, Paula Waschbusch, Nic Fiszman, Mamoru Kato, Rafi Katzman, and Mousumi Roy.

Dave Krowitz, Linda Meinke, and Dave Bauman kept the computers purring, and Libby Kurten, Marie Sénat, Deb Sykes, and Beverly Kozel-Tattlebaum smoothed out the paperwork and Tom's schedule.

EAPS Softball, Hoops, and Hockey kept me younger, mentally if not physically. "Nine Planets" redefine fast-pitch softball, and opened my mind to the possibility that life after 40 won't be so bad.

My family has always been extremely supportive of my ongoing education, despite the abstract nature of my endeavors. I appreciate their encouragement, and I'm thankful to have spent these years so close to home.

Finally, I could not have done this without Jennifer. She's encouraged me to pursue my dreams, given me space to work when needed, and yet prevented me from working too hard. Because of Jen, the memories of my graduate years will not be of a computer screen full of tangled Love waves, but rather of Saturday mornings chasing squirrels in the Arb with Kiko. Thank you.